Enhancement of End-loss Ion Flux Using Ion Cyclotron Range of Frequency Waves on GAMMA 10/PDX

Seowon Jang

February 2020

Enhancement of End-loss Ion Flux Using Ion Cyclotron Range of Frequency Waves on GAMMA 10/PDX

Seowon Jang

Doctoral Program in Physics

Submitted to the Graduate School of

Pure and Applied Sciences

in Partial Fulfillment of the Requirements

for the Degree of Doctor of Philosophy in

Science

at the

University of Tsukuba

1. INTRODUCTION

1.1 Fusion Power

New power generation technology is required because of the depletion of fossil fuels and growing energy demand due to the increase of the global population. Consequently, research on power generation using nuclear fusion reactions is now under way. Fusion reactions are performed when two or more atomic nuclei come close enough that the nuclear force pulling them exceeds the electrostatic force pushing them. For nuclei lighter than iron, the reactions are exothermic. Plasmas are used to bring the atomic nuclei close enough for fusion to occur. The easiest fusion reaction at low energy is the reaction with deuterium and tritium, as follows

$$ {}_1^2\mathrm{D} + {}_1^3\mathrm{T} \rightarrow {}_2^4\mathrm{He}(3.5\ \mathrm{MeV}) + {}_0^1\mathrm{n}(14.1\ \mathrm{MeV}). \quad (1.1) $$

Deuterium exists in sea water and tritium can be produced by the nuclear reactions between lithium and neutrons:

$$ {}_0^1\mathrm{n} + {}_3^6\mathrm{Li} \rightarrow {}_1^3\mathrm{T} + {}_2^4\mathrm{He} \quad (1.2) $$

$$ {}_0^1\mathrm{n} + {}_3^7\mathrm{Li} \rightarrow {}_1^3\mathrm{T} + {}_2^4\mathrm{He} + {}_0^1\mathrm{n} \quad (1.3) $$

Because lithium can be found in sea water, the fuel resources for fusion power are almost inexhaustible. In addition, fusions reactions do not generate carbon dioxide, nitric oxide or any of the other gases which cause global environmental pollution. The radioactive waste arising from neutron activation of the fusion reactor materials is at a lower level than that in nuclear fission reactors and the fusion reactor materials could be recycled within about 100 years of shutdown.

The fusion energy gain factor, which is usually expressed with the symbol Q, is the ratio of the fusion power to the power required to maintain the plasma. To increase Q, it is necessary to sustain high ion temperature, density, and confinement time. For example, Q is 1 for a plasma with a temperature of 10 keV, the density of 10^{20} m^{-3} and a confinement time of one second. As Q further increases, the plasma can be sustained by self-

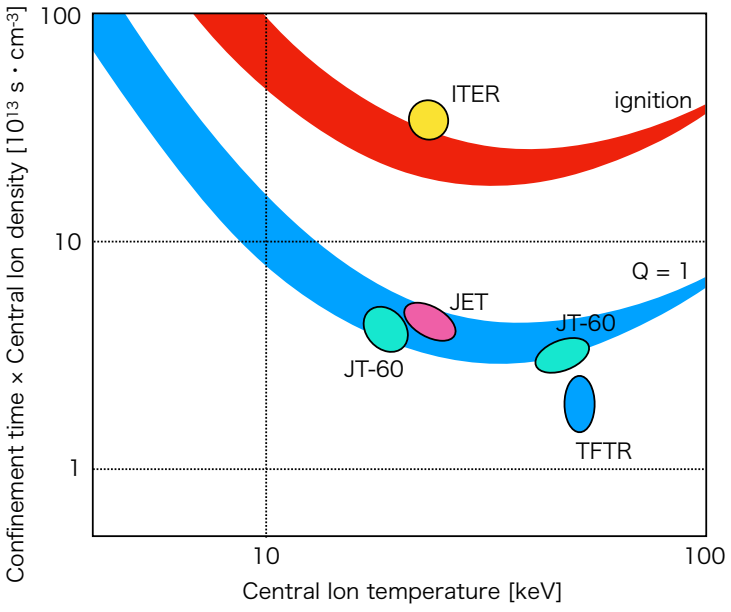

Figure 1.1 Lawson diagram. Blue and red regions show the condition of Q = 1 and ignition, respectively. The parameter regions of several tokamak devices are plotted.

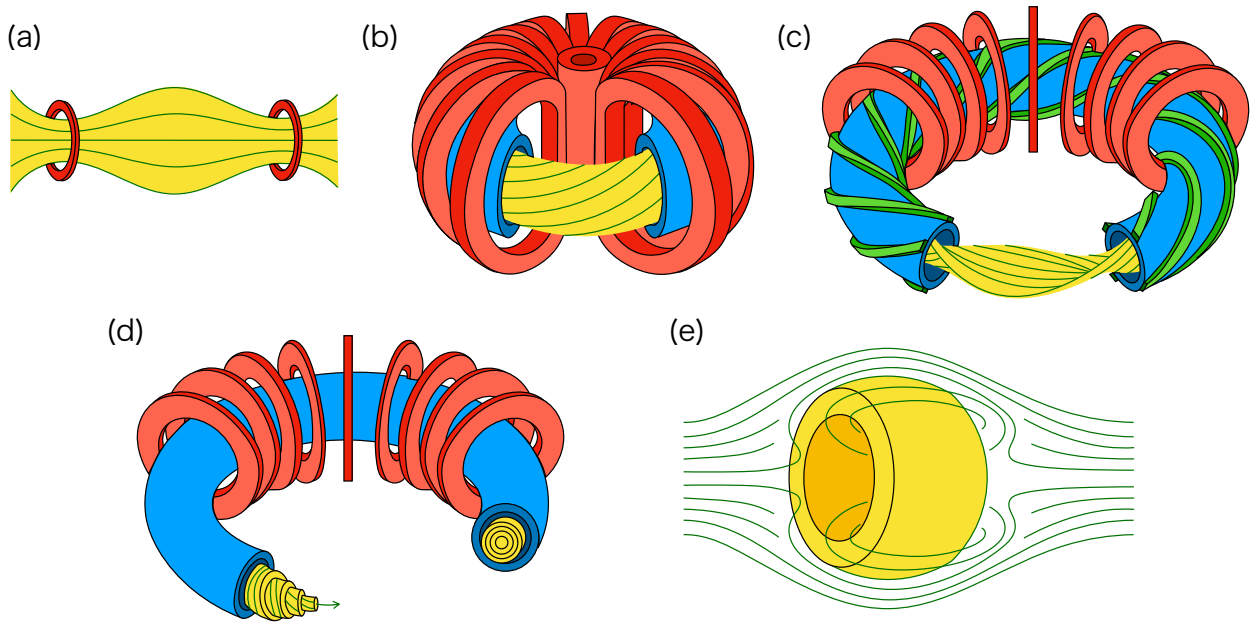

Figure 1.2 Schematic drawing of: (a) a magnetic mirror, (b) a tokamak, (c) a stellarator, (d) a reversed field pinch, and (e) a field reversed configuration.

heating of alpha particles. When the reaction become self-sustaining, which is called ignition, Q becomes infinite. Figure 1.1 (Lawson diagram) shows the condition of Q = 1, and ignition as blue and red regions, respectively [1]. The vertical and horizontal lines are described as products of the central ion density and the confinement time, and the ion temperature, respectively.

Plasma confinement is necessary to keep plasmas at high density and hot long enough to undergo fusion reactions. There are two general principles of confinement: magnetic confinement and inertial confinement. First, magnetic confinement attempts to use the cyclotron motion of charged particles around a magnetic field. Figure 1.2 shows a schematic drawing of several types of magnetic confinement device. Figure 1.2 (a) shows magnetic mirror confinement, which will be explained in Section 2.1. The other examples of magnetic confinement with magnetic loops include a tokamak (Fig. 1.2 (b)) [2-4], a stellarator (Fig. 1.2 (c)) [5,6], a reversed field pinch (Fig. 1.2 (d)) [7], and a field reversed configuration (Fig. 1.2 (e)) [8,9]. The most highly developed system is the tokamak. The parameter regions of several tokamak devices (i.e., JT-60, JET and TFTR) are plotted in Fig. 1.1 [3,10,11]. A new tokamak device, called ITER, is currently in development thanks to the collaboration of China, the European Union, India, Japan, Korea, Russia, and the United States. One of the goals of ITER is to produce 500 MW of fusion power with 50 MW injected heating power ($Q \geq 10$) for pulses of 400 seconds. Several other projects are underway to develop fusion power [12,13]. Second, in inertial confinement high-energy laser beams are injected to a target filled with deuterium and tritium. The heated outer layer explodes the target and the target is compressed by a reaction force that accelerates it inward. The fuel is then heated and becomes high density due to the implosion, and fusion reactions then occur [14].

1.2 Studies of Divertor Physics in Linear Plasma Devices

In fusion reactors, damage to the device materials from the heat load of high temperature and high-density core plasma is an important issue [15]. A divertor is installed to appropriately reduce the heat and particle flux flowing from the core plasma along the magnetic field lines, as shown in Fig. 1.3. In fusion reactors, the steady

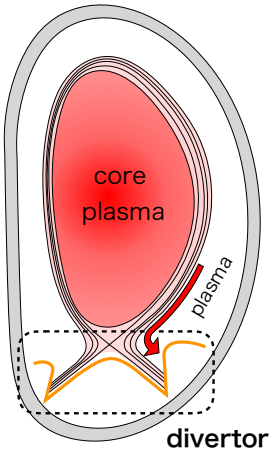

Figure 1.3 Schematic drawing of a cross-section of a typical tokamak device.

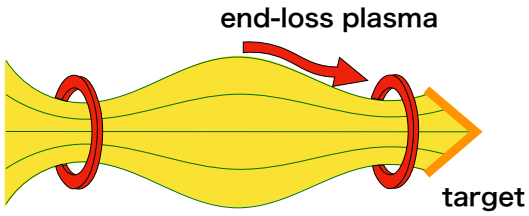

Figure 1.4 Schematic drawing of a linear device.

heat flux from the core plasma to the divertor is expected to exceed 10 MW/m^2. Therefore, it is necessary to develop an effective method for reducing the heat flux by clarifying the divertor's physics. In a linear plasma device with an open magnetic field configuration, experiments utilizing end-loss plasmas flowing along the magnetic field lines are performed to study the divertor's physics in the fusion reactor [16-20]. A target that simulates the divertor for these studies is installed at the end region, as shown in Fig. 1.4.

Linear devices offer simple geometrical configuration, measurement accessibility, and flexible plasma conditions to study the divertor's physics. In these studies, control of the plasma parameters, especially ion energy distribution, is required because high ion temperature (~100 eV) and high ion flux (10^{23} - 10^{25} m^{-2}s^{-1}) are expected at divertor and scrape-off layer plasmas in the fusion reactor. However, many linear devices that

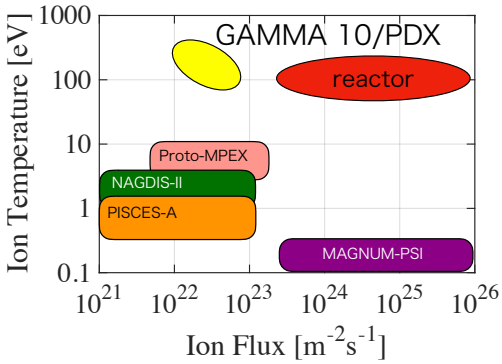

Figure 1.5 Parameter region of several linear devices and a fusion reactor.

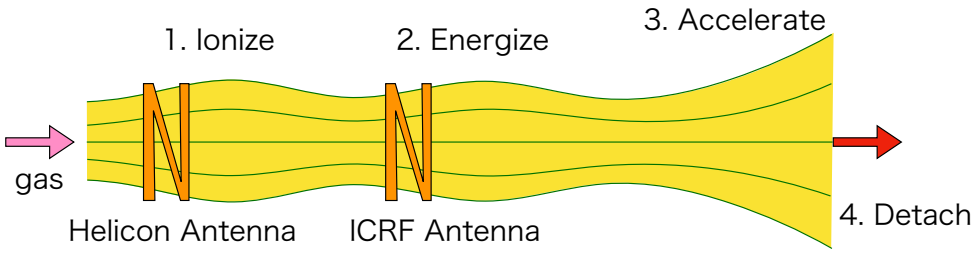

Figure 1.6 Schematic drawing of a plasma thruster.

are currently in operation have low ion temperature and low ion flux, as shown in Fig. 1.5 [18,20-24]. Ion heating with ion cyclotron range of frequency (ICRF) waves is carried out in several devices to increase the ion temperature and the ion flux by enhancing the end-loss ions, including GAMMA 10/PDX [19,20].

1.3 Development of a Plasma Thruster

Enhancement of the end-loss ions is an important issue for the development of a spacecraft plasma thruster. In a spacecraft propulsion system, it is necessary to reduce weight and improve long-term durability. Chemical rockets have high thrust, low specific impulse (total impulse delivered per unit of propellant consumed), while electric propulsion has low thrust and high specific impulse. A plasma thruster with high specific impulse and long-term durability because it does not use electrodes is intended to bridge the gap between chemical rockets and the electric propulsion. However, high thrust has not yet been demonstrated.

Figure 1.6 shows a schematic drawing of a Variable Specific Impulse Magnetoplasma Rocket (VASIMR), which is one method of developing a plasma thruster [25,26]. The plasma is produced by a helicon RF system with neutral gas fuel. The ions are heated with ICRF waves and flow to a divergent magnetic field configuration. The parallel velocity of the ions increases with the decrease of the magnetic field strength, under the conservation of the energy and magnetic moment, and the rocket then ejects the ions. To increase the thrust, studies have been conducted on the influence of plasma density, species of the neutral gas, magnetic field configuration, diameter of the engine, and optimization of the ICRF heating on the thrust [25–30].

1.4 ICRF Waves

ICRF waves are excited by an ICRF antenna and propagate in the plasmas, where they interact with ions by resonating with ions at the resonance layer. Ion heating with ICRF waves is one of the most powerful methods to control the ion energy distribution because it can directly interact with the ions. The results of the control of the ion energy distribution using ICRF waves in various devices, such as torus devices and linear devices, have previously been reported [19, 20, 25, 26, 31–33]. In addition, wave-particle interactions are an important issue in a collisionless space plasma because they are thought to play a crucial role in the energy transfer between particles. Research of the energy transfer of particles via these wave-particle interactions has been carried out using simulation and observations [34–38].

In GAMMA 10/PDX tandem mirror device, plasmas are produced and heated with ICRF waves. The additional ICRF heating has been performed with various combinations of ICRF antennas and frequencies to control the end-loss ion flux and temperature. The energy distribution of end-loss plasmas is obtained at each

discharge by measuring the end-loss particles. The experimental results of the interaction with ICRF waves and end-loss ions and electrons have previously been reported [39–43].

1.5 Organization of the Thesis

This thesis describes the experimental results of the enhancement of end-loss ions by using ICRF waves that can control the energy distribution. Chapter 2 presents the principles of magnetic mirror confinement and electromagnetic wave propagation. In addition, the GAMMA 10/PDX and its ICRF systems, fueling systems and plasma gun are introduced. Then, Chapter 3 describes the diagnostic tools for the end-loss ions, reflectometers for observing the density profiles and spatial structure of the ICRF waves, and diagnostic tools for the power from ICRF oscillators. Chapter 4 describes and discusses the experimental results. In particular, the results of the enhancement of the end-loss ion flux are introduced in Section 4.1. The experimental results of additional ICRF heating and the results of feature selection are also described. Meanwhile, Section 4.2 discusses the enhancement of the high-energy end-loss ions using ICRF waves. Finally, Chapter 5 summarizes the results of this thesis.

2 EXPERIMENTAL SETUPS

2.1 Magnetic Mirror Confinements

A magnetic mirror is a plasma confinement method that utilizes a reflection of charged particles in an inhomogeneous magnetic field. When the charged particles move in an inhomogeneous magnetic field strength B in a parallel direction to the magnetic field line, their pitch angle θ is changed by a change of B. The magnetic momentum μ, which is the product of the electrical current I and the area of circular motion S, is given by

$$\mu = I \times S = \frac{mv_{\perp}^2}{2B} \tag{2.1}$$

and the total kinetic energy of the particle ε is given by

$$\varepsilon = \frac{1}{2}mv_{\perp}^2 + \frac{1}{2}mv_{\parallel}^2 + q\phi \tag{2.2}$$

where m is mass, q is electric charge, $v_{\perp}$ is the velocity of the particle in the perpendicular direction to the magnetic field line and $v_{\parallel}$ is the velocity in the parallel direction of the charged particle. ϕ is the profile of the electrostatic potential along the magnetic field line. Energy ε and magnetic momentum μ are both conservative. Then, the velocity in the parallel direction $v_{\parallel}$ can be written as

$$v_{\parallel} = \pm\sqrt{v^2 - \frac{2}{m}\mu B - q\Delta\phi} \tag{2.3}$$

where v is the velocity of the particle ($v=\pm\sqrt{v_{\perp}^2 + v_{\parallel}^2}$) and $\Delta\phi$ is the difference of the potential. Therefore, $|v_{\parallel}|$ increases/decreases with the decrease/increase of B, and the charged particles are reflected when B is sufficiently high. The condition of the reflection of the charged particle is given as

$$\sin^2\theta = \frac{B}{B_{ref}}\left(1 - \frac{2q\Delta\phi}{mv^2}\right) \tag{2.4}$$

where B_{ref} is magnetic field strength at the reflection position. The particles that the pitch angle is smaller than

$$\sin^2\theta < \frac{B_0}{B_M}\left(1 - \frac{2q\Delta\phi}{mv^2}\right) \tag{2.5}$$

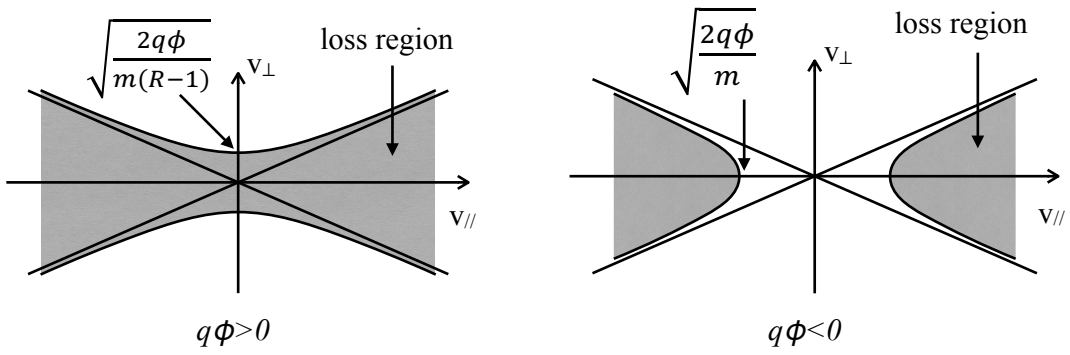

Figure 2.1 Loss region (gray areas) of a charged particle in velocity space.

where B_M and B_0 are the maximum and minimum strength of the mirror magnetic field, respectively, escape from the mirror magnetic field. The ratio of the B_M and B_0 is called a mirror ratio R.

$$R = \frac{B_M}{B_0} \tag{2.6}$$

The region of Eq. 2.5 is called the loss cone and the plasmas that escape from the magnetic mirror are called the end-loss plasmas. Fig. 2.1 shows the loss region of a charged particle in velocity space.

2.2 GAMMA 10/PDX Tandem Mirror

The GAMMA 10/PDX tandem mirror is composed of five mirror cells: central cell, east and west anchor cells located both sides of the central cell and east and west plug/barrier cells at both ends. Figure 2.2 shows the coil arrangement, magnetic flux tube and magnetic field distribution on the z-axis. Hydrogen plasmas are produced with ICRF waves.

The central cell has a simple magnetic mirror configuration for main plasma confinement and is 5.6 m in length. The magnetic field strength at the midplane is 0.4 T and the ion cyclotron resonance frequency is 6.2 MHz. The maximum magnetic field strength is 2 T and the mirror ratio is 5. Limiters with a diameter of 36 cm are installed near the midplane (z = 33 cm). The anchor cells have minimum-B configuration for magneto-hydrodynamic (MHD) stabilization of the whole plasma. The length of the anchor cells is 4.76 m. The magnetic field strength at the midplane is 0.6 T and the ion cyclotron resonance frequency is 9.4 MHz. The mirror ratio is 3.3. Production of high-pressure plasmas in the anchor cells is required for MHD stabilization [44–45]. The plug/barrier cells have an axisymmetric configuration and are 2.48 m in length. The magnetic field strength at the midplane is 0.5 T and the ion cyclotron resonance frequency is 7.6 MHz. The maximum magnetic field strength is 3 T and the mirror ratio is 6. The formation of the confinement potential is performed with electron cyclotron heating [46]. Also, the additional heating with ICRF waves is carried out [47–48].

2.3 ICRF Waves in Magnetized Plasma on GAMMA 10/PDX

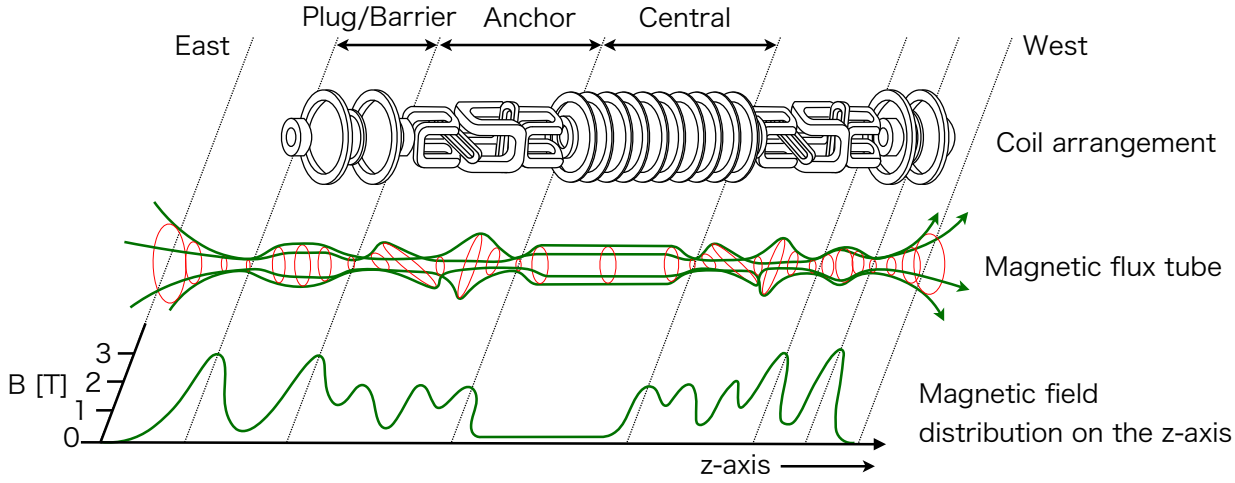

Figure 2.2 Schematic drawing of GAMMA 10/PDX, which shows the coil arrangement, magnetic field tube and magnetic field distribution on the z-axis.

The electromagnetic fields that are generated by the plasma current are written by the Maxwell's equation,

$$\begin{aligned} \nabla \cdot \boldsymbol{E} &= \sum_{s=i,e} q_s n_s \\ \nabla \times \boldsymbol{E} &= -\frac{\partial \boldsymbol{B}}{\partial t} \\ \nabla \cdot \boldsymbol{B} &= 0 \\ \nabla \times \boldsymbol{B} &= \mu_0 \left(\boldsymbol{J} + \epsilon_0 \frac{\partial \boldsymbol{E}}{\partial t} \right) \end{aligned} \tag{2.7}$$

where $\boldsymbol{E}$ is the electric field, $\boldsymbol{B}$ is the magnetic field, n is charge density, μ_0 is the permeability and ϵ_0 is permittivity of free space. Here, the $\boldsymbol{E}$ and $\boldsymbol{B}$ are assumed as follows

$$\begin{aligned} \boldsymbol{E} &\propto \exp\big(i(\boldsymbol{k} \cdot \boldsymbol{r} - \omega t)\big) \\ \boldsymbol{B} &\propto \exp\big(i(\boldsymbol{k} \cdot \boldsymbol{r} - \omega t)\big) \end{aligned} \tag{2.8}$$

where $\boldsymbol{k}$ is the wavenumber, $\boldsymbol{r}$ is the space coordinates and ω is the wave angular frequency. We then obtain,

$$\mathrm{i}\boldsymbol{k} \times \boldsymbol{B} = \mu_0(\boldsymbol{J} - i\omega\epsilon_0 \boldsymbol{E}) \tag{2.9}$$

$$\mathrm{i}\boldsymbol{k} \times \boldsymbol{E} - i\omega \boldsymbol{B} = 0. \tag{2.10}$$

We combine the plasma current and the displacement current,

$$\boldsymbol{J} - i\omega\epsilon_0 \boldsymbol{E} \equiv -i\omega\epsilon_0 \overleftrightarrow{\boldsymbol{K}} \cdot \boldsymbol{E} \tag{2.11}$$

where $\overleftrightarrow{\boldsymbol{K}}$ is the dielectric tensor. By substituting Eq. 2.10 into Eq. 2.9, we obtain,

$$\frac{c^2}{\omega^2} \boldsymbol{k} \times (\boldsymbol{k} \times \boldsymbol{E}) = -\boldsymbol{E} + \frac{1}{i\omega\epsilon_0} \boldsymbol{J} = -\begin{bmatrix} S & -iD & 0 \\ iD & S & 0 \\ 0 & 0 & P \end{bmatrix} \cdot \begin{bmatrix} E_x \\ E_y \\ E_z \end{bmatrix} \equiv -\overleftrightarrow{\boldsymbol{K}} \cdot \boldsymbol{E} \tag{2.12}$$

where c is the speed of light,

$$c^2 = \frac{1}{\epsilon_0 \mu_0}. \tag{2.13}$$

The right-handed coordinate system that $B_x = B_y = 0$, $B_z = B$ and $k_y = 0$ is used. The elements of the dielectric tensor are defined as follows

$$\begin{aligned} S \equiv K_1 &\equiv \frac{1}{2}(R + L) = 1 - \sum_s \frac{\omega_{ps}^2}{\omega^2 - \omega_{cs}^2} \\ D \equiv iK_2 &\equiv \frac{1}{2}(R - L) = 1 - \sum_s \frac{\epsilon_s \omega_{cs} \omega_{ps}^2}{\omega(\omega^2 - \omega_{cs}^2)} \\ P \equiv iK_3 &= 1 - \sum_s \frac{\omega_{ps}^2}{\omega^2} \\ K_1 + iK_2 \equiv R &\equiv S + D = 1 - \sum_s \frac{\omega_{ps}^2}{\omega(\omega + \epsilon_s \omega_{cs})} \\ K_1 - iK_2 \equiv L &\equiv S - D = 1 - \sum_s \frac{\omega_{ps}^2}{\omega(\omega - \epsilon_s \omega_{cs})} \end{aligned} \tag{2.14}$$

where ϵ_s is the sign of the charge for species.

Here, we explain the index of the refraction vector $\boldsymbol{n}$

$$\boldsymbol{n} = \frac{\boldsymbol{k}c}{\omega} \tag{2.15}$$

whose direction is that of the wavenumber and magnitude is the index of refraction. By substituting Eq. 2.15 into Eq. 2.12, we obtain

$$\boldsymbol{n} \times (\boldsymbol{n} \times \boldsymbol{E}) + \overleftrightarrow{\boldsymbol{K}} \cdot \boldsymbol{E} = 0. \tag{2.16}$$

By using a vector calculation

$$\boldsymbol{n} \times (\boldsymbol{n} \times \boldsymbol{E}) = \boldsymbol{n} \cdot (\boldsymbol{n} \cdot \boldsymbol{E}) - n^2 \boldsymbol{E}, \tag{2.17}$$

Eq. 2.16 can be rewritten as

$$\begin{bmatrix} S - n_\parallel^2 & -iD & n_\perp n_\parallel \\ iD & S - n^2 & 0 \\ n_\perp n_\parallel & 0 & P - n_\perp^2 \end{bmatrix} \cdot \begin{bmatrix} E_x \\ E_y \\ E_z \end{bmatrix} = 0. \tag{2.18}$$

To have a nontrivial solution, Eq. 2.18 requires that the determinant of coefficients becomes zero. This condition gives the dispersion relation,

$$P n_\parallel^4 + \Big((S+P) n_\perp^2 - 2PS \Big) n_\parallel^2 + (n_\perp^2 - P)(S n_\perp^2 - LR) = 0 \tag{2.19}$$

In special cases where the wavenumber is parallel ($n_\perp^2 = 0$) and perpendicular ($n_\parallel^2 = 0$) to the magnetic field, the dispersion equation is obtained as follows.

1. Propagation parallel to the magnetic field
   a) $P = K_3 = 0$ (plasma oscillations)
   b) $n_\parallel^2 = R = K_1 + iK_2$ (wave with right-hand polarization)
   c) $n_\parallel^2 = L = K_1 - iK_2$ (wave with left-hand polarization)
2. Propagation perpendicular to the magnetic field
   a) $n_\perp^2 = P = K_3$ (ordinary wave (O-mode))
   b) $n_\perp^2 = \frac{LR}{S} = \frac{(K_1^2 + K_2^2)}{K_1}$ (extraordinary wave (X-mode))

The cutoff and resonance phenomena occur when $\boldsymbol{n}$ becomes zero and infinite, respectively.

In GAMMA 10/PDX, the ICRF waves that satisfy $\omega \ll \omega_{ce}, \omega_{pe}$ are excited and $\omega_{pi} \ll \omega_{pe}$. In these assumptions, Eq. 2.19 can be rewritten as

$$\begin{aligned} P &\approx -\frac{\omega_{pe}^2}{\omega^2} \\ R &\approx 1 - \frac{\omega_{pe}^2}{(\omega + \omega_{ci})(-\omega_{ce})} = 1 + \frac{\omega_{pi}^2}{\omega_{ci}(\omega + \omega_{ci})} \\ L &\approx 1 - \frac{\omega_{pe}^2}{(\omega - \omega_{ci})\omega_{ce}} = 1 - \frac{\omega_{pi}^2}{\omega_{ci}(\omega - \omega_{ci})}. \end{aligned} \tag{2.20}$$

From Eq. 2.18,

$$\begin{aligned} \left| \frac{E_x}{E_z} \right| &\approx -P \approx \frac{\omega_{pe}^2}{\omega_{ci}^2} \gg 1, \\ \left| \frac{E_x}{E_y} \right| &\approx \left| \frac{S}{D} \right| = \left| \frac{R+L}{R-L} \right| \sim 1 \end{aligned} \tag{2.21}$$

Hence, the contribution of E_z is negligible. The dispersion equation for ICRF waves is given as

$$\begin{vmatrix} S - n_\parallel^2 & -iD \\ iD & S - n^2 - n_\perp^2 \end{vmatrix} = 0, \tag{2.22}$$

$$n_\parallel^4 + (n_\perp^2 - 2S) n_\parallel^2 - (S n_\perp^2 - LR) = 0. \tag{2.23}$$

The answer is obtained as

$$n_\parallel^2 = \frac{1}{2} \left[2S - n_\perp^2 \pm \sqrt{(n_\perp^2 - 2S)^2 + 4(S n_\perp^2 - RL)} \right]. \tag{2.24}$$

In GAMMA 10/PDX, the ICRF waves in the case of $n_\perp^2 = 0$ that

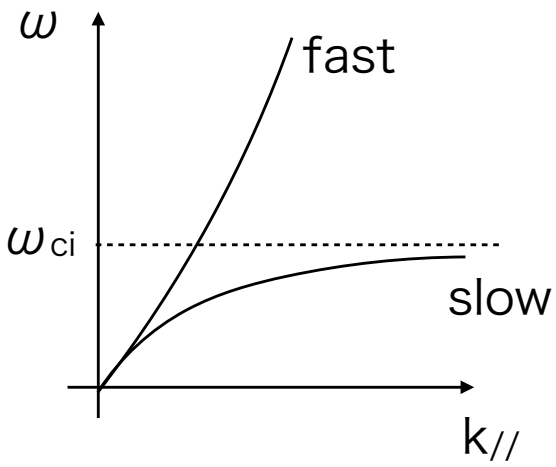

Figure 2.3 Dispersion relation of fast and slow waves which propagate along the magnetic field.

$$n_{\parallel}^2 = R \tag{2.25}$$

$$n_{\parallel}^2 = L \tag{2.26}$$

are used. Figure 2.3 shows the dispersion relation of the ICRF waves of Eq. 2.25 and Eq. 2.26, which are called fast wave and slow wave, respectively. The fast wave and the slow wave have a higher and a lower phase velocity than Alfvén velocity, respectively. The fast wave has no resonance and the cutoff layer and can propagate in the high-density region. In GAMMA 10/PDX, this is used for plasma production. Meanwhile, the slow wave has a resonance layer at the ion cyclotron frequency. Therefore, the strong interaction between the wave field and the ions is used for ion heating.

2.4 Ion Cyclotron Range of the Frequency System

Three ICRF power amplifier systems—called RF1, RF2 and RF3—are installed in GAMMA 10/PDX. The ICRF systems are composed of a signal generator (SG), wide band amplifier (WBA), intermediate power amplifier (IPA) and final-stage power amplifier (PA). The ICRF waves generated from SG are amplified in stages. RF1 and RF2 have two final outputs and RF3 has one final output. The nominal maximum output powers are 300 kW for RF1 and RF2, and 200 kW for RF3. Figure 2.4 gives a schematic drawing of the magnetic field lines and ICRF antennas installed in GAMMA 10/PDX. Ten sets of ICRF antenna are installed: two Nagoya Type-III (Type-III) antennas and two double half turn (DHT) antennas in the central cell, a double arc type (DAT) antenna in the east anchor cell, two DAT antennas in the west anchor cell, a Type-III antenna in the west plug/barrier cell, and two circle type antennas in the east end region.

In normal discharges, RF1 is connected to two Type-III antennas located in the central cell for plasma production. The Type-III antennas are driven with frequencies of 9.9 MHz (east side) and 10.3 MHz (west side) with an input power of about 100 kW. Fast waves produce the plasmas in the central cell. In addition, the fast waves excited with the Type-III antennas propagate to the anchor cells and are converted to slow waves in the field transition region between the central and the anchor cells, and they heat ions near the midplane of the anchor cells for the MHD stability of GAMMA 10/PDX [44-45]. A few 10^{18} m^{-3} electron densities in the central cell and the anchor cells are achieved by the ICRF heating. RF2 and RF3 are connected to the ICRF antennas, depending on the purpose of the additional heating experiments. Usually, RF2 is connected to two DHT antennas that are located near both ends of the central cell and ICRF waves with a frequency of 6.36 MHz, which have resonance layers near the midplane of the central cell, are excited for ion heating [49].

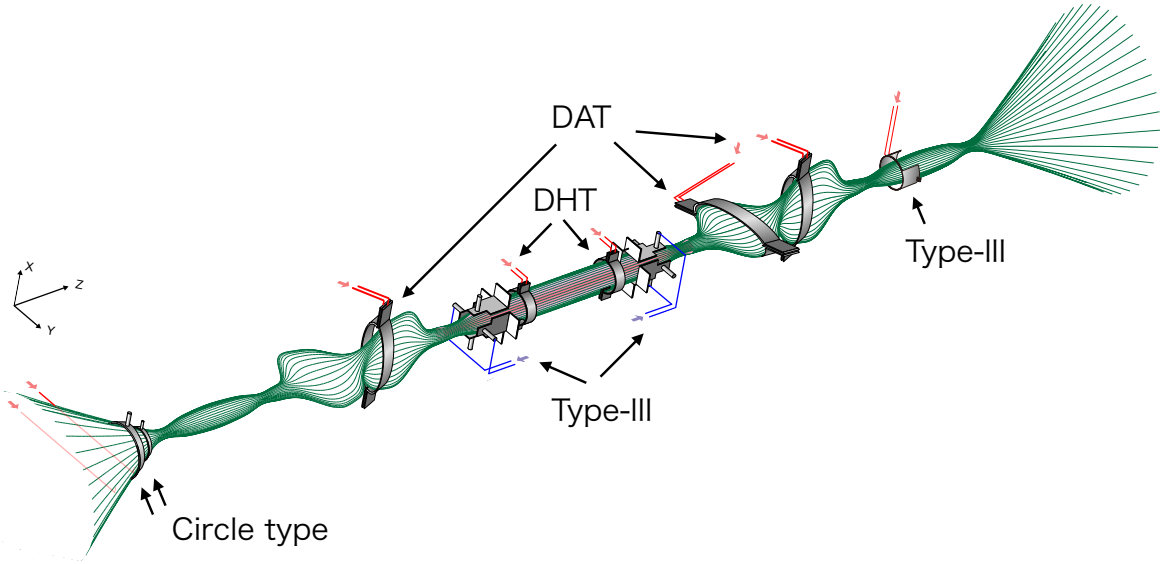

Figure 2.4 Schematic drawing of the magnetic field line and ICRF antennas in GAMMA 10/PDX.

2.5 Gas Puffing System

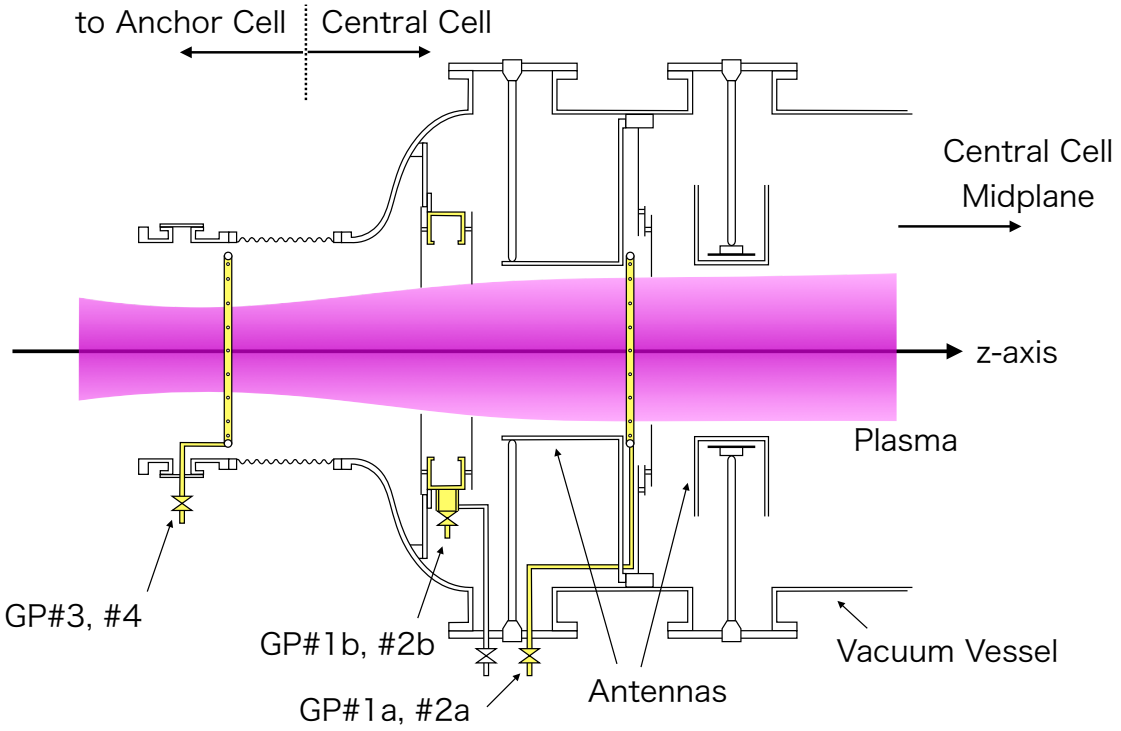

Figure 2.5 Schematic drawing of the gas puffing system in GAMMA 10/PDX. One side of the central cell near the mirror throat is described.

The plasmas in GAMMA 10/PDX are sustained by RF systems with a hydrogen gas puff. Figure 2.5 gives a schematic drawing of the gas puffing systems in the one side of the central cell. The gas puffing systems are mainly installed near both the mirror throat of the central cell. In normal discharges, four gas puffing systems are used, named GP#1b, GP#2b, GP#3 and GP#4. GP#2b and GP#4 are located at the opposite side of the central cell. GP#1b and GP#2b are box type and have a fast response. Therefore, they are used to build up the plasmas with a short-pulse and a high pressure. GP#3 and GP#4 are ring type and can supply gas evenly in the azimuthal direction. Therefore, they are used to sustain the plasmas with a long pulse. GP#1a and GP#2a are ring type and are used for additional gas puffing in the central cell. In addition, a pipe type GP#7 is installed near the midplane of the central cell and a ring type GP#5 and GP#6 are installed at the east and west plug/barrier cells, respectively.

2.6 Plasma Gun

Seed plasma is injected along the magnetic field line from the east open end, and heated and sustained by ICRF waves and gas puffing. A pulsed Magneto Plasma Dynamic Arc-jet (MPDA) is injected during 1 ms at the startup of the plasma to form an initial target plasma for further heating with high power ICRF waves [50]. Figure 2.6 gives a schematic drawing of the plasma gun. The plasmas are produced between an anode and a cathode, and accelerated by the $\boldsymbol{j}\times\boldsymbol{B}$ force, where $\boldsymbol{j}$ is the radial component of the discharge current and $\boldsymbol{B}$ is the azimuthal component of the self-induced magnetic field.

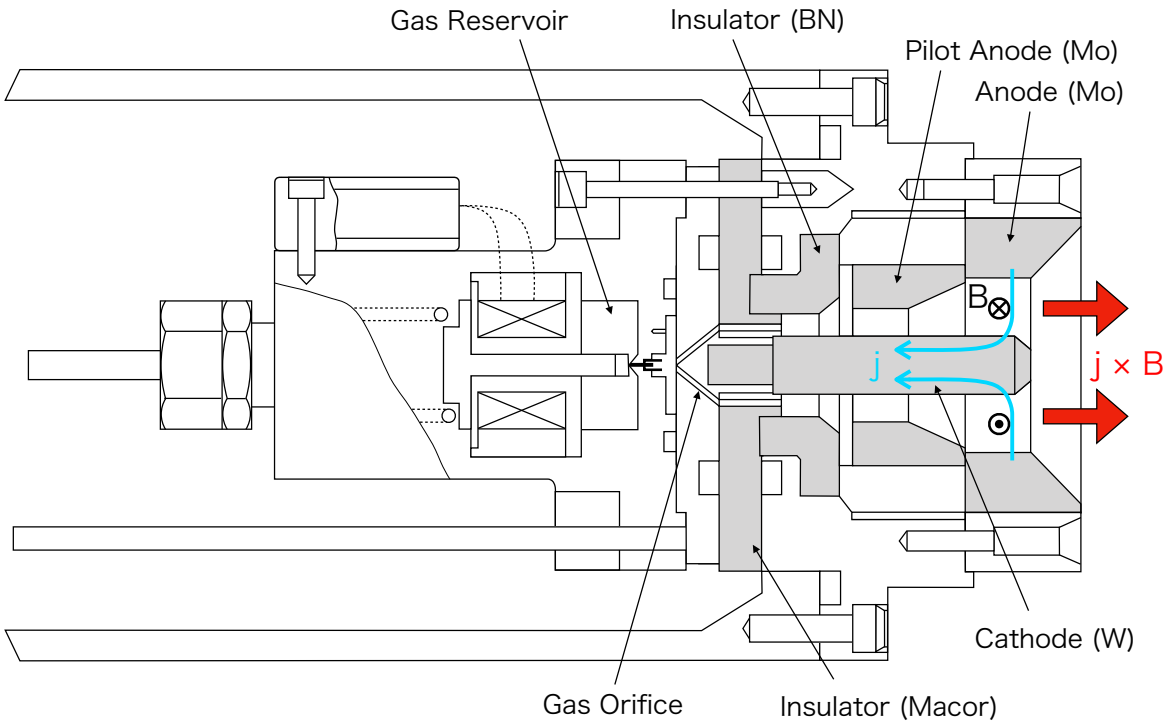

Figure 2.6 Schematic drawing of the plasma gun.

3 DIAGNOSTIC TOOLS

3.1 End-Loss Energy Component Analyzer (ELECA)

The parallel and the perpendicular velocity distribution functions of the end-loss ions are measured using an End-Loss Energy Component Analyzer (ELECA). The ELECA is installed at the east end region, z = -13.6 m, where the strength of magnetic field is about 0.01 T and is aligned with the magnetic field direction. The pitch angle of ions flowing from the upstream is lower than about 3.3˚ at ELECA. The radial position mapping into the midplane of the central cell through the magnetic field line is 4.4 cm (r_{cc} = 4.4 cm). Figure 3.1 gives schematic views of ELECA. The ELECA mainly consists of a collimator, a movable rectangular entrance slit, an entrance aperture, cylindrical electrodes, a rectangular exit slit, and a MCP detector.

3.1.1 Design of the ELECA

A collimator in front of the entrance aperture consist four step of copper plates with sharp knife edges and is cut in a cone shape with an acceptance angle that is large enough to measure the ions flowing from the upstream. Because copper metal has a small reflection coefficient for the UV rays, the intensity of the UV rays decreases with reflections of rays on the copper plates. The width of the rectangular entrance slit is 0.23 mm and it is installed aligned along the Z_a-axis. When the entrance slit is inserted, the ions that have a r_{ent} velocity component cannot enter the entrance aperture. The entrance aperture is a small pin hole with a diameter of 0.08 mm. The cylindrical electrodes are made of copper plates with a deflection angle of 127.3˚ ($\pi/\sqrt{2}$ radian), and the radiuses of the inner and outer electrodes are r_1 = 4.0 and r_2 = 5.0 cm, respectively. The outer electrode has two holes to install UV dumps. The direct UV rays enter into the UV dump from the first hole, which is covered with a high-transparency tungsten mesh (> 90%) coated with frosted micro-carbon. The second hole and UV dump are installed to absorb the scattered UV rays. The exit slit has a width of 2 mm and a length of 30 mm. The MCP detector is divided into 20 portions aligned along the exit slit, and the width of each channel and the gap between the channels are 0.82 mm and 0.1 mm, respectively. All of the components are covered with a copper housing with a thickness of 10 mm to absorb UV rays and x rays.

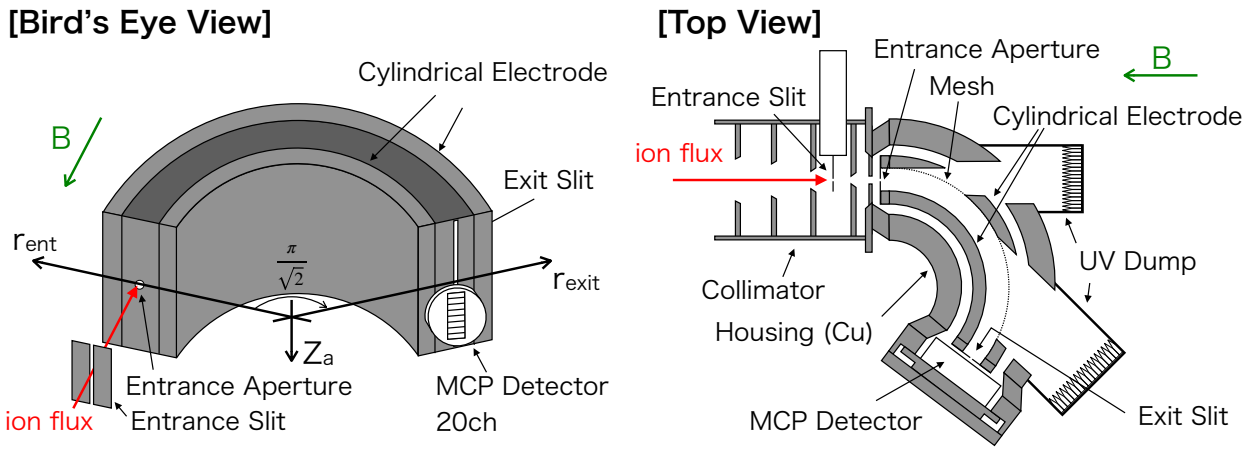

Figure 3.1 Schematic drawing of ELECA.

The parallel velocity component of the end-loss ions is analyzed by the electric field E_r between the cylindrical electrodes. To keep the potential grounded on the cylindrical central surface, voltages V_1 and V_2 are applied in the inner and the outer electrodes, as follows

$$V_1 = \int_{r_0}^{r_1} E_r dr = V_0 \frac{ln(r_1/r_0)}{ln(r_2/r_1)} = -0.5278\, V_0 \tag{3.1}$$

$$V_2 = \int_{r_0}^{r_2} E_r dr = V_0 \frac{\ln(r_2/r_0)}{\ln(r_2/r_1)} = 0.4722\, V_0 \tag{3.2}$$

where V_0 is the electric potential difference. The incidence ions from the entrance aperture with the energy of ε are as follows

$$\varepsilon = \frac{qV_0}{2\ln(r_2/r_1)} \tag{3.3}$$

Which can pass through the exit slit and be detected by MCP detector.

The MCP gain is obtained by experiments characterization of the MCP using ion beam with an energy of 0.1 – 10 keV [51]. The MCP gain g is given by

$$\xi = -14.25 + 3.367 \ln \varepsilon - 0.1859(\ln \varepsilon)^2 \tag{3.4}$$

$$g = \xi(\varepsilon) \exp\left(-106 + 127V_{mcp} - 35V_{mcp}^2\right) \tag{3.5}$$

where ξ is the relative sensitivity, V_{mcp} is the MCP bias voltage in V and the ion energy ε is in eV. In addition, the MCP gain saturates when the input current that produces the output current density equals 5% of the strip current density. Figure 3.2 shows the output current of MCP detector (channel 10) as a function of the ion energy. The red and blue lines describe the ion current, which are measured by sweeping the voltage between the electrodes from high energy to low energy, and vice versa, respectively, when the plasma parameters are kept constant. The V_{mcp} is 1.7 kV. The ion current of

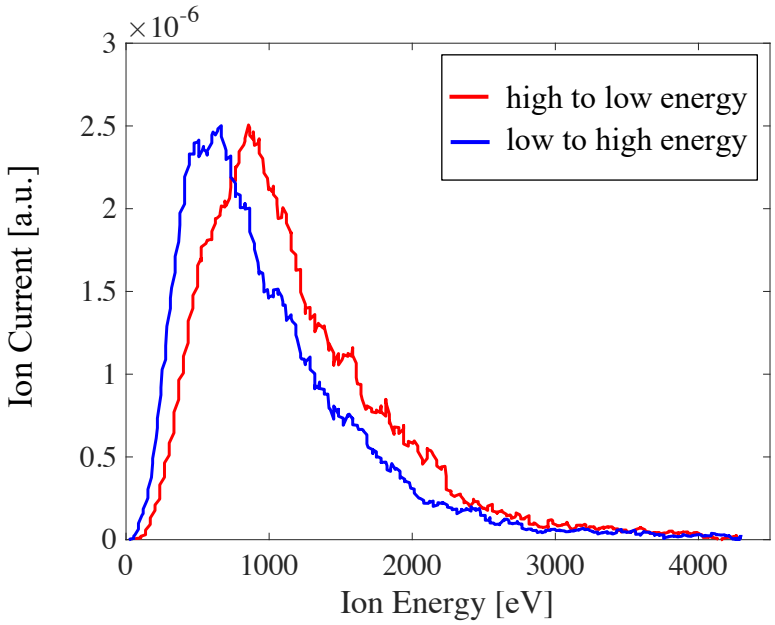

Figure 3.2 Output current of the MCP detector (channel 10) as a function of ion energy. The red and blue lines describe the ion current and are measured by sweeping voltage between the electrodes from high energy to low energy, and vice versa, respectively, and V_{mcp} is 1.7 kV.

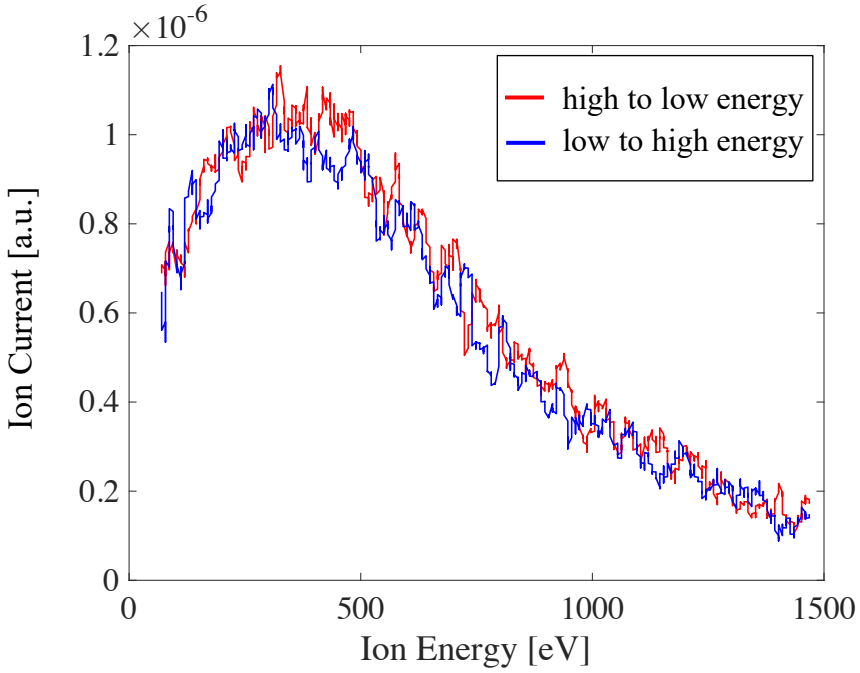

Figure 3.3 Output current of the MCP detector (channel 10) as a function of ion energy. The red and blue lines describe the ion current and are measured by sweeping voltage between the electrodes from high energy to low energy, and vice versa, respectively, and V_{mcp} is 1.6 kV.

the red line is bigger than the blue line at the high-energy region and is smaller at the low-energy region. This indicates that the MCP gain is decreased with the saturation of the MCP. Hence, the output ion current on the low energy of the red line and the high energy of the blue line is lower than the appropriate ion current. In contrast, the output ion current is almost the same when the voltage is swept in a decreasing direction (red line) and an increasing direction (blue line) by decreasing V_{mcp} to 1.6 kV, as shown in Fig. 3.3. This indicates that the MCP saturation is eliminated by the decrease of the V_{mcp}.

3.1.2 Trajectories of the Incidence Ions in ELECA

The trajectories of the incidence ions in ELECA have been estimated by numerical calculation to evaluate the influence of the force by electric field between the electrodes and $\boldsymbol{j}\times\boldsymbol{B}$ force. The equation of motion of the ions is obtained as

$$m\frac{d\boldsymbol{v}}{dt} = q\boldsymbol{E} + q\boldsymbol{v}\times\boldsymbol{B} \tag{3.6}$$

where $\boldsymbol{v}$ is the velocity of the ions, $\boldsymbol{E}$ is the electric field and $\boldsymbol{B}$ is the magnetic field. For simplicity, the ideal cylindrical electric field and uniform magnetic field in the perpendicular direction to the entrance aperture are assumed to be

$$\boldsymbol{E} = \frac{qV_0}{r\ln\left(\frac{r_2}{r_1}\right)}\frac{\boldsymbol{r}}{r} \tag{3.7}$$

The equation of motion of ions with various energy and pitch angle is solved using Runge-Kutta 4 algorithm.

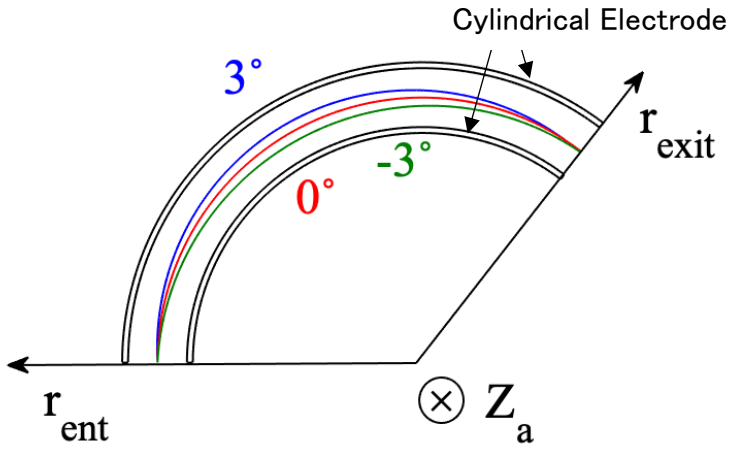

Figure 3.4 Top view of ELECA and the trajectories of ions with an energy of 1000 eV. The trajectories of the ions with a pitch angle with -3˚, 0˚ and 3˚ with velocity component in the direction of Z_a is zero are plotted.

Figure 3.4 shows a top view of ELECA and the trajectories of the ions with an energy of 1000 eV. The voltage to collect these ions between the electrodes is 446 V. The velocity component in the direction of Z_a is zero and the velocity component in the direction of r_{ent} velocity component of the ions varies in the pitch angle between -3 and 3 degrees. The trajectories of these ions are again focused at the exit slit with a deflection angle of 127.3˚. This is consistent with the trajectories that are derived by the formalism of the time-dependent Lagrange equations.

The trajectories of the ions that have non-zero Z_a velocity component with zero r_{ent} velocity component are calculated to simulate the situation of the ELECA when a movable rectangular entrance slit is inserted. Figure 3.5 shows the trajectories of the ions. The orbits of the ions are curved by the force of the electric field and they move downward by the $\boldsymbol{j}\times\boldsymbol{B}$ force. The MCP channels are aligned along Z_a-axis to measure the pitch angle (perpendicular velocity) of the ions. Figure 3.6 shows the measurement region of each MCP channel in

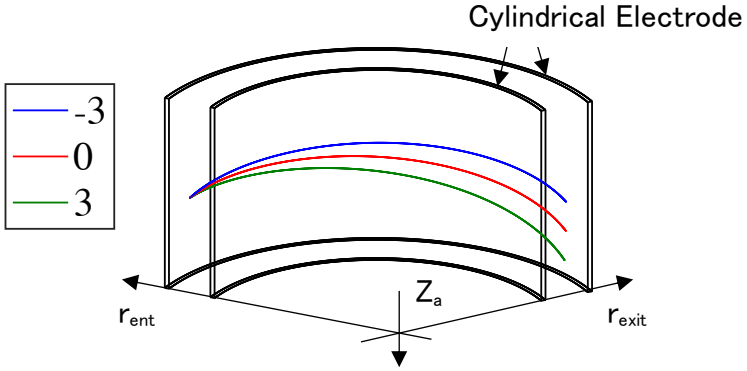

Figure 3.5 Bird's eye view of ELECA and the trajectories of the ions with an energy of 1000 eV. The trajectories of the ions with a pitch angle with -3˚, 0˚ and 3˚ when the r_{ent} velocity component is zero are plotted.

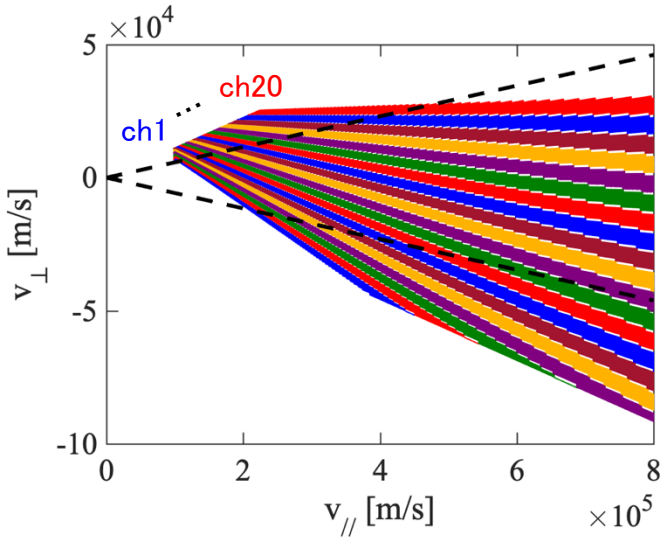

Figure 3.6 The measurement region of each MCP channel in velocity space.

velocity space. Therefore, the pitch angle distribution (perpendicular velocity distribution function) is obtained by imaging the ions on an exit plane, shown as a channel number of the MCP.

3.1.3 Velocity Distribution Function

The velocity distribution function $f(v_\perp, v_\parallel)$ at the entrance aperture of ELECA is derived from the output current of each channel of the MCP. In this chapter, the velocity distribution functions with and without the movable entrance slit are introduced.

i) Velocity Distribution Function Without an Entrance Slit

Figure 3.7 shows the measurement regions of ELECA in (a) the $v_\parallel - v_\perp$ space and (b) the $v_{\perp rent} - v_{\perp Za}$ space. The solid hyperbolic line indicates the boundary of the loss cone of the ions. The small element of the volume in the velocity space can be written by

$$dV = dv_\parallel \cdot d(v_\parallel tan\theta) \cdot d\left(\sqrt{v_\perp^2 - (v_\parallel tan\theta)^2}\right). \tag{3.8}$$

where the θ is pitch angle of the end-loss ions. The density Δn in the small element of the volume is described as

$$\begin{aligned} \Delta n &= f(v_\perp, v_\parallel)dV \\ &= f(v_\perp, v_\parallel) \cdot dv_\parallel \cdot d(v_\parallel tan\theta) \cdot d\left(\sqrt{v_\perp^2 - (v_\parallel tan\theta)^2}\right) \\ &\cong f(v_\perp, v_\parallel) \frac{v_\parallel v_\perp dv_\parallel dv_\perp d\theta}{\cos^2\theta \sqrt{v_\perp^2 - (v_\parallel tan\theta)^2}}. \end{aligned} \tag{3.9}$$

The equation is obtained,

$$\frac{d\theta}{cos^2\theta} = \frac{dz}{l_{mp}} \tag{3.10}$$

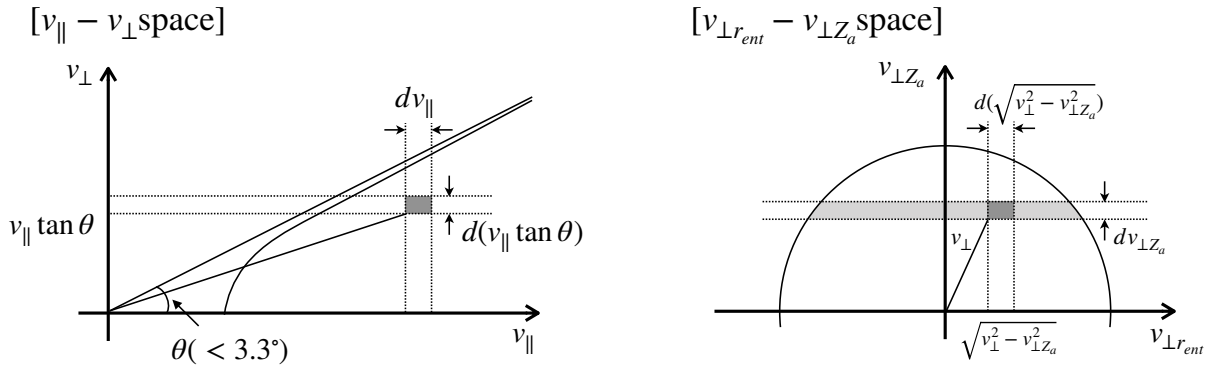

Figure 3.7 Measurement regions of ELECA in (a) the $v_{\parallel} - v_{\perp}$ space and (b) the $v_{\perp rent} - v_{\perp Za}$ space without an entrance slit.

where the l_{mp} is the length of the circumferential direction of the middle of the electrodes and z is the distance from the center of the electrode along the Za-axis to the MCP channel. Because the magnetic field strength at the location of ELECA is low (about 0.01 T), the energy of ions ε can be approach to $mv_{\parallel}^2/2$ and

$$dv_{\parallel} = \frac{d\varepsilon}{\sqrt{2m\varepsilon}} \tag{3.11}$$

is obtained. By substituting into Eq. 3.9, we may rewrite that the equation as

$$\Delta n = f(v_{\perp}, v_{\parallel}) \frac{v_{\perp} dv_{\perp} d\varepsilon\, dz}{m\, l_{mp} \sqrt{v_{\perp}^2 - \kappa^2}} \tag{3.12}$$

where κ is defined as $z/l_{mp}\sqrt{2\varepsilon/m}$. The number of ions incidence into the MCP detector $\mathrm{I}(\varepsilon, \kappa)$ with the energy between $\varepsilon + \Delta\varepsilon$ and the location between $z + \Delta z$ is obtained as

$$\mathrm{I}(\varepsilon, \kappa) = \frac{2\sqrt{2\varepsilon}\, \Delta\varepsilon\, \Delta z\, \delta S}{\sqrt{m^3}\, l_{mp}} \int_{\kappa}^{v_{\perp}max} \frac{f(v_{\perp}, v_{\parallel})\, v_{\perp} dv_{\perp}}{\sqrt{v_{\perp}^2 - \kappa^2}} \tag{3.13}$$

where δS is the area of the entrance aperture. The velocity distribution function is obtained by performing Abel inversion on Eq. 3.13, as follows

$$f(v_{\perp}, v_{\parallel}) = \frac{\sqrt{m^3}\, l_{mp}}{\pi\sqrt{2\varepsilon}\, \Delta\varepsilon\, \Delta z\, \delta S} \int_{\kappa}^{v_{\perp}max} \frac{\mathrm{dI}(\varepsilon, \kappa)}{d\kappa} \frac{d\kappa}{\sqrt{\kappa^2 - v_{\perp}^2}}. \tag{3.14}$$

$\mathrm{I}(\varepsilon, \kappa)$ is obtained from the MCP detector by sweeping the voltage between the electrodes.

ii) Velocity Distribution Function With an Entrance Slit

The incidence ions are limited on $v_{\perp rent}$ by the entrance slit, as shown in Fig. 3.8. When the integrated width Δv_w is small enough, Eq. 3.13 is rewritten by

$$\mathrm{I}'^{(\varepsilon,\kappa)} = \frac{\sqrt{2\varepsilon}\, \Delta v_w\, \Delta\varepsilon\, \Delta z\, \delta S}{\sqrt{m^3}\, l_{mp}} f(v_{\perp}, v_{\parallel}) \tag{3.15}$$

and the velocity distribution is obtained without Abel inversion, as follows

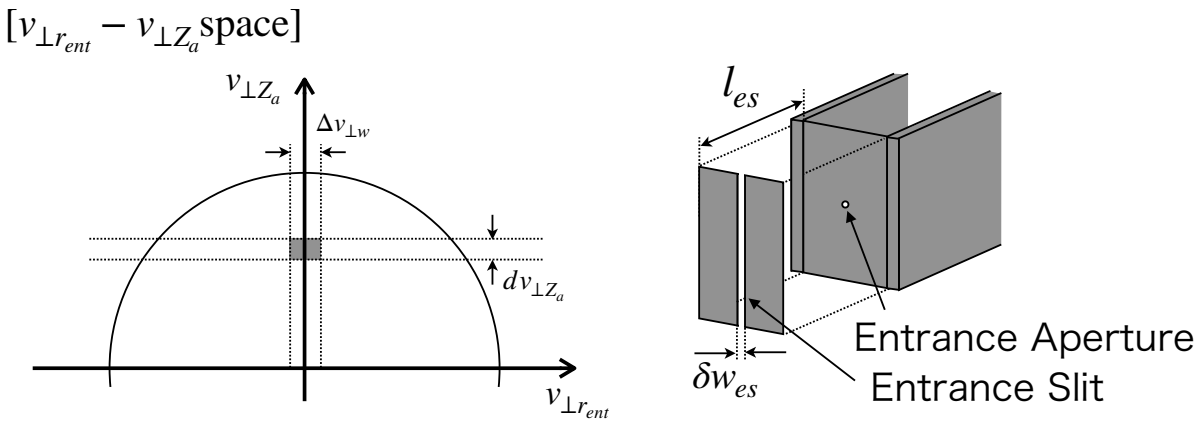

Figure 3.8 The measurement region of ELECA in the $v_{\perp rent} - v_{\perp Za}$ space with the entrance slit.

$$f(v_\perp, v_\parallel) = \frac{\sqrt{m^3}\, l_{mp}}{\sqrt{2\varepsilon}\, \Delta v_w\, \Delta\varepsilon\, \Delta z\, \delta S} \mathrm{I}'^{(\varepsilon,\kappa)}. \tag{3.16}$$

3.1.4 Energy Distribution Function

The density of the end-loss ions n_{loss} can be written by

$$\begin{aligned} n_{loss} &= \int f(v,\theta,\phi) d\boldsymbol{v} \\ &= \int_0^\infty dv \int_0^\pi d\theta \int_0^{2\pi} d\phi\, f(v,\theta,\phi)\, v^2 sin\theta \end{aligned} \tag{3.17}$$

where the $f(v,\theta,\phi)$ is the velocity distribution of the end-loss ions, v is the velocity of the end-loss ions, which is divided into $v_\perp$ and $v_\parallel$. Angle θ and ϕ are the zenithal and azimuthal angle, respectively, angle θ is the pitch angle of the end-loss ions. Here, if we assume that the velocity distribution is symmetrical with respect to the $v_\parallel$-axis existing only in the loss cone ($< \theta_{max}$), then Eq. 3.17 is rewritten as

$$n_{loss} = \int_0^\infty dv\, f_v(v)\, v^2 \tag{3.18}$$

and

$$f_v(v) \equiv 2\pi \int_0^{\theta max} d\theta\, f(v,\theta)\, sin\theta\,. \tag{3.19}$$

By using the energy ε of the end-loss ions, Eq. 3.18 can be rewritten as

$$n_{loss} = \int \frac{\sqrt{2}}{m^{\frac{3}{2}}} f_v(v)\sqrt{\varepsilon}\, d\varepsilon \tag{3.20}$$

and

$$n_{loss} = \int f_\varepsilon(\varepsilon) d\varepsilon \tag{3.21}$$

where the energy distribution is defined as

$$f_\varepsilon(\varepsilon) \equiv \frac{\sqrt{2}}{m^{\frac{3}{2}}} f_v(v)\sqrt{\varepsilon}. \tag{3.22}$$

The output ion current $\Delta J_{loss}(\varepsilon)$ with the energy between ε and $\varepsilon + \Delta\varepsilon$ is obtained with

$$\Delta J_{loss}(\varepsilon) = envs = e\, f_\varepsilon(\varepsilon)\, \varepsilon\, C_A \sqrt{\frac{2\varepsilon}{m}}\, \delta S \tag{3.23}$$

where C_A is the energy resolution $\frac{\Delta\varepsilon}{\varepsilon}$. Therefore, the energy distribution function is described as

$$f_\varepsilon(\varepsilon) = \frac{\sqrt{m}}{\sqrt{2}\, e\, \delta S \sqrt{\varepsilon^3}\, C_A} \Delta J_{loss}(\varepsilon). \tag{3.24}$$

3.2 End-Loss Ion Energy Analyzer (ELIEA)

The ion flux and the parallel ion energy distribution of the end-loss ions and the potential of the upstream plasma are measured using the End-Loss Ion Energy Analyzer (ELIEA). The ELIEA is installed at both end regions. There are 10 and 20 channels of ELIEA at the east and west end region, respectively, as shown in Fig. 3.9. The radial positions as converted to the radius in the central cell (r_{cc}) of the channels are 2.59cm, 5.26 cm, 8.25 cm, 11.19 cm and 14.64 cm. Figure 3.10 gives a schematic view of ELIEA, which consists of an ion repeller grid, an ion energy control grid, a secondary electron repeller grid and a collector plate.

The ion repeller grid is installed with an angle of 42˚ and the grounded ion energy control grid with triangular structure is installed between the ion repeller grid and the collector plate. A positive voltage is applied at the ion repeller grid and the perpendicular electric field with respect to the ion repeller grid is formed between the ion repeller grid and the ion energy control grid. The incident ions are reflected by the electric field and are collected as the ion current by the collected plate. The ion current can be written as follows

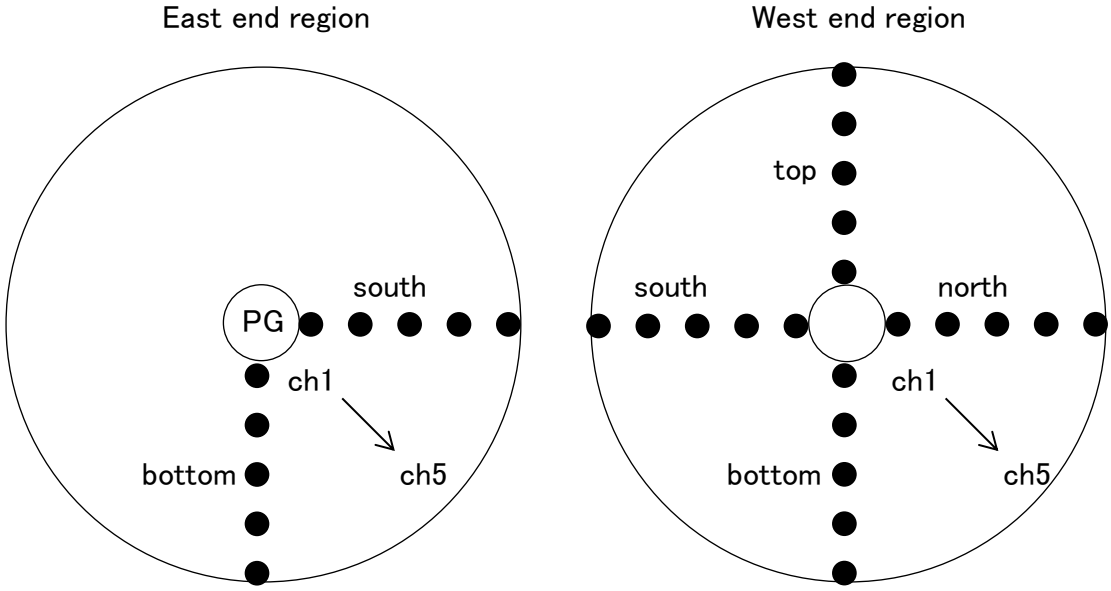

Figure 3.9 Radial positions of ELIEA at the east and west end regions.

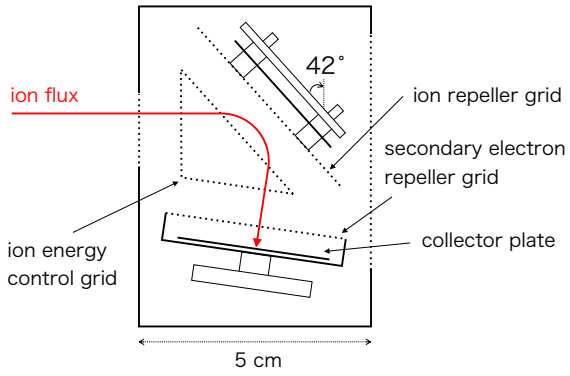

Figure 3.10 Schematic drawing of the ELIEA.

$$I = \int_0^{\frac{V}{cos^2 42°}} dE_{\parallel}\, f(E_{\parallel})\,. \tag{3.25}$$

The energy distribution is obtained by sweeping the voltage of the ion repeller grid. Figure 3.11 shows the typical V-I characteristic observed with ELIEA. In the high voltage region, most end-loss ions are reflected and collected. Hence, the ion current is saturated in the high-energy region and the ion flux of the end-loss ions are estimated from this value. The energy distribution is obtained with the differential of V-I characteristic of ELIEA.

In normal discharge on GAMMA 10/PDX, the potential of the plasmas in the central cell and anchor cells is positive because the electrons of the mirror plasma escape the mirror region much faster than the ions. Hence, the ions flowing from upstream are accelerated by the potential and the energy distribution of the end-loss ions at the end region is shifted to the high-energy region. The potential of the confined plasma (Φ) is obtained from the voltage where the ion current becomes non-zero. Figure 3.12 shows the potential observed with ELIEA as a function of the potential in the central cell observed with a Gold Neutral Beam Probe (GNBP) located at z = 118 m on 77 shots of typical discharges on GAMMA 10/PDX. A dashed line shows that two measured values are equal. The potential observed with ELIEA is almost same as the potential in the central cell because the central cell is the main source of the end-loss ions.

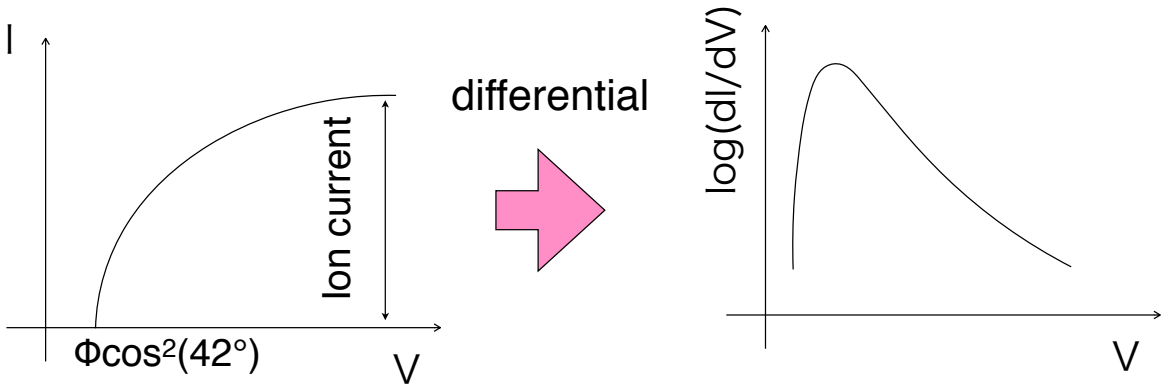

Figure 3.11 Sketch of the typical V-I characteristic observed with ELIEA and the ion energy distribution.

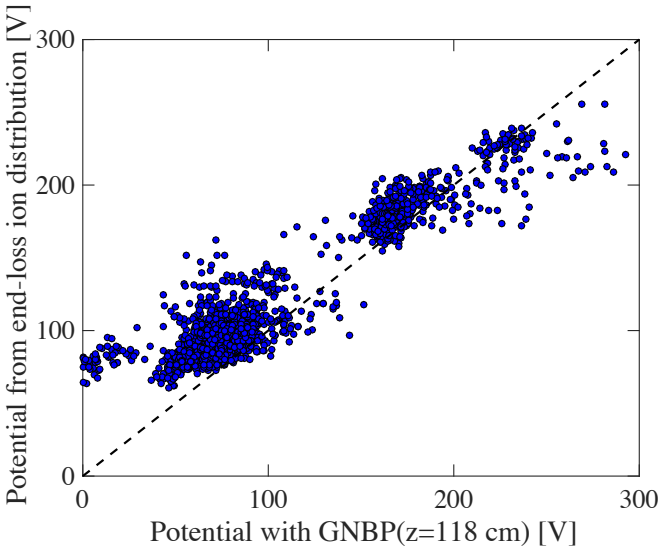

Figure 3.12 The potential observed with ELIEA as a function of the potential in the central cell observed with GNBP.

3.3 Reflectometer

The density profile and the density fluctuation due to ICRF waves are measured using a reflectometer installed in the central cell. We have developed one homodyne frequency modulation (FM) reflectometer and two heterodyne reflectometers to observe these fluctuations. Six sets of X-band with O-mode horn antennas are installed on the interior of vacuum vessel in the central cell: five axial positions of z = 52, 82, 112, 142, 193 cm and a position having a difference of azimuth angle of 78˚ at z = 82 cm.

3.3.1 Measurement of a Density Profile

A homodyne FM reflectometer is used to measure the density profile [52-55]. Figure 3.13 gives a schematic drawing of a FM reflectometer. The frequency of the microwave f_{pr} is swept and a beat signal between reflected wave and reference wave is generated in a mixer. The beat frequency f_{beat} can be written as

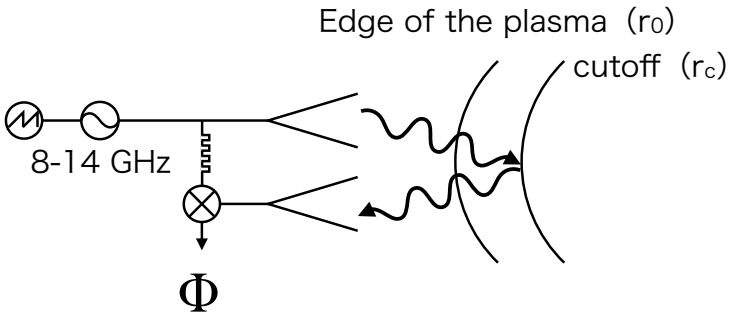

Figure 3.13 Schematic diagram of a FM reflectometer.

$$f_{beat} = \frac{df_{pr}}{dt}\tau_{delay} = \frac{df_{pr}}{dt}\left(\tau_0 + \tau_{plasma}\right) \tag{3.26}$$

where τ_{delay} is a delay time between the reflected wave and the reference wave, τ_0 is the delay time due to circuit and vacuum path length, and τ_{plasma} is the delay time due to plasma. The beat frequency can control the length of the delay line of the reference wave and varies by about 10 MHz on GAMMA 10/PDX. The phase difference $d\phi$ by sweeping the probing frequency f_{pr} can be written as

$$d\phi = 2\pi f_{beat} dt = 2\pi df_{pr}\left(\tau_0 + \tau_{plasma}\right) \tag{3.27}$$

and by substituting Eq. 3.27 into Eq. 3.26, we obtain

$$\frac{1}{2\pi}\frac{d\phi_0}{df_{pr}} = \tau_0 \tag{3.28}$$

$$\frac{1}{2\pi}\frac{d\phi_{plasma}}{df_{pr}} = \tau_{plasma} \tag{3.29}$$

where ϕ_0 and ϕ_{plasma} is a change of the phase due to circuit/vacuum path length and plasma, respectively. The phase ϕ_{plasma} can be written as

$$\phi_{plasma} = 2\frac{2\pi f_{pr}}{c}\int_{r_0}^{r_c} N dr \tag{3.30}$$

where N is the plasma refractive index and r_0 and r_c are the edge of the plasma and cutoff radii, respectively. In the case of O-mode microwave, Eq. 3.30 is rewritten as

$$\phi_{plasma} = 2\frac{2\pi f_{pr}}{c}\int_{r_0}^{r_c}\sqrt{1 - \frac{f_p^2}{f_{pr}^2}}\, dr \tag{3.31}$$

and the cutoff radius r_c is obtained by performing Abel inversion as

$$r(f_{pr}) = r_0 - \frac{c}{\pi}\int_0^{f_{pr}} \frac{1}{2\pi}\frac{d\phi_{plasma}}{df_{pr}}\frac{1}{\sqrt{f_{pr}^2 - f^2}} df\,. \tag{3.32}$$

Because the domain of the integration starts from 0 Hz, it is necessary to observe with another diagnostic or assume the density profile of the edge plasma. In GAMMA 10/PDX, the frequency of the microwave is swept from 8.3 GHz to 14 GHz with O-mode. Therefore, a density profile below the cutoff density of the microwave of 8.3 GHz (0.85×10^{18} m^3) is required. Calibration experiments to obtain the delay time due to circuit and vacuum path length τ_0 Are also required.

i) Delay Time Due to Circuit and Vacuum Path Length

Calibration experiments are performed to observe the delay time due to circuit and vacuum path length τ_0. Figure 3.14 shows a cross-section of the GAMMA 10/PDX and the setup of the calculation experiments. A metallic plate is installed in front of the horn antennas in the vacuum vessel and moves along the radius direction. The delay time τ_0 is observed under various radius with the FM reflectometer. Figure 3.15 shows the raw data of the mixer beat signal and probing frequency as blue and red lines, respectively. Figure 3.16 shows the phase difference obtained with phase extraction of the beat signal using the Complex Demodulation method as a function of the probing frequency [53]. The results of the experiments with several radii of the metallic plate is plotted. The phase is increase linearly with the increase of the frequency. The gradient of the phase $\frac{d\phi_0}{df_{pr}}$ is increased with the decrease of the radius of the metallic plate, as shown in Fig. 3.17. The dashed line describes the fitting line as a linear polynomial. The appropriate calibration value is selected according to the experimental conditions.

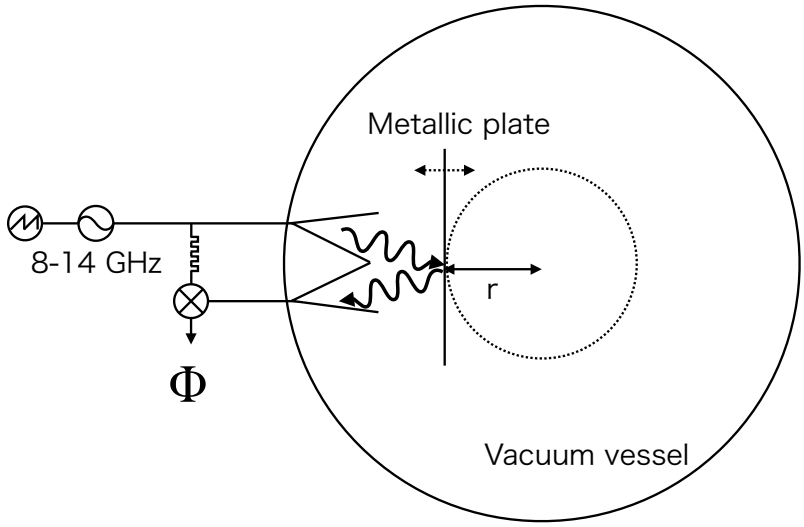

Figure 3.14 Cross-section of the GAMMA 10/PDX and the setup of the calculation experiments.

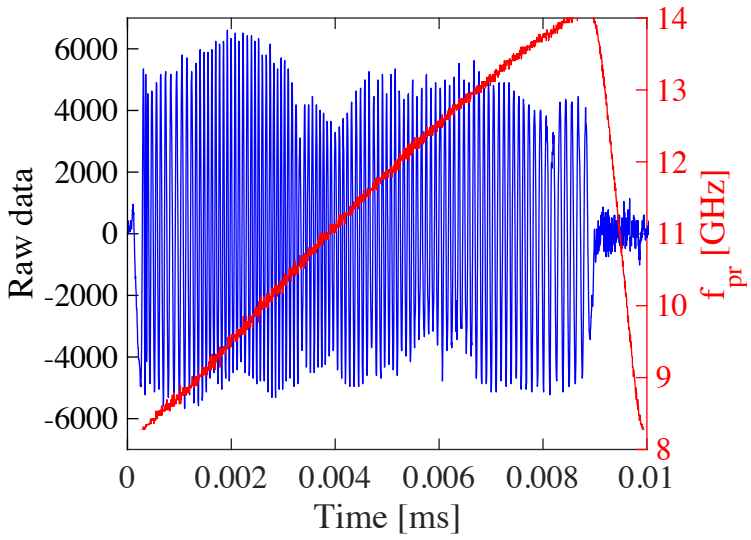

Figure 3.15 The raw data of the mixer beat signal (blue line) and probing frequency of the microwave (red line) on the calibration experiments.

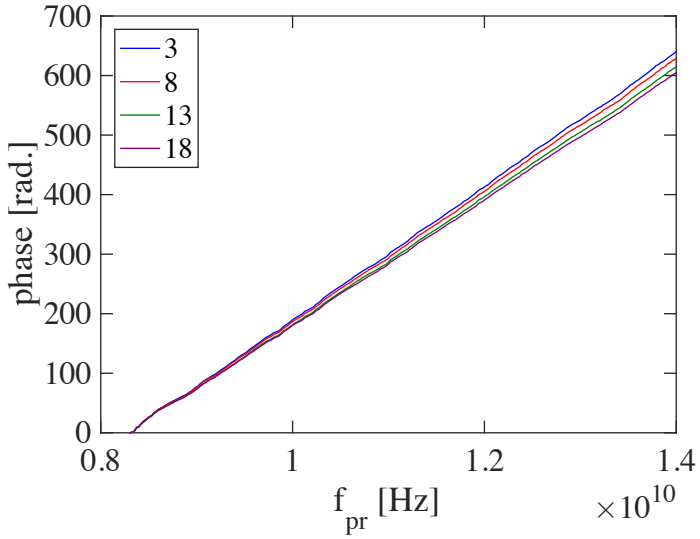

Figure 3.16 Phase due to circuit and vacuum path ϕ_0 as a function of the probing frequency.

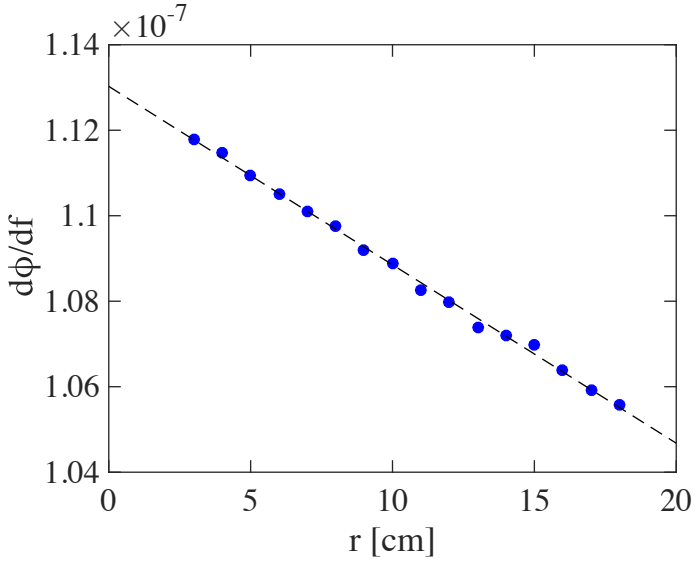

Figure 3.17 The gradient of the phase $\frac{d\phi_0}{df_{pr}}$ as a function of the radius of the metal plate.

ii) Measurement of a Density Profile Using FM Reflectometer

As was explained previously, it is necessary to observe with another diagnostic tool or assume the density profile of the edge plasma. In this chapter, the density profile is assumed as a solid blue line as shown in Fig.3.18. The black-dashed line indicates the cutoff density of the O-mode microwave of 9.0 GHz. Figure 3.19 shows the measured ϕ_{plasma} as a red line of the location of z = 52 cm and fitting curve as a blue line from Fig. 3.18. The frequency sweep speed is 100 kHz, which is sufficiently high for neglecting the density fluctuation. The phase at the frequencies lower than 9 GHz cannot be measured due to noise. Figure 3.20 shows the density profile, which is calculated with Eq. 3.32 using the fitting curve.

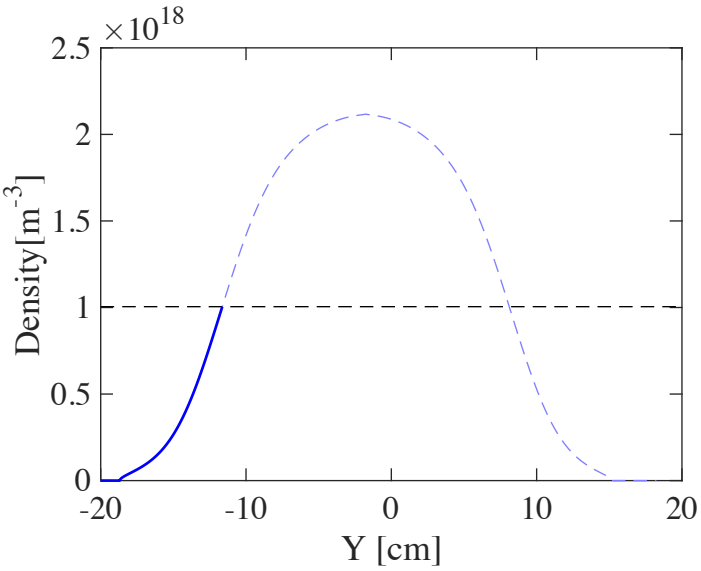

Figure 3.18 Assumed density profile of the edge region.

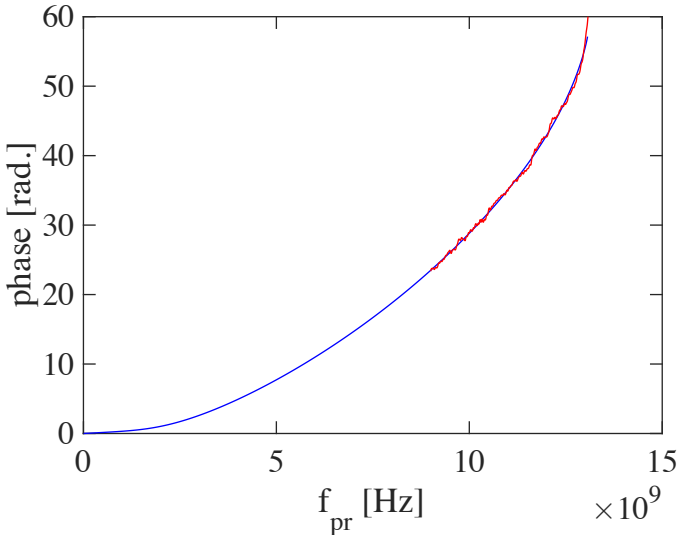

Figure 3.19 Measurment result of the phase due to plasma ϕ_{plasma} as a red line using the horn antenna located at z = 52 cm. The blue line describes the fitting line using the assumed density profile, as shown in Fig.3.18.

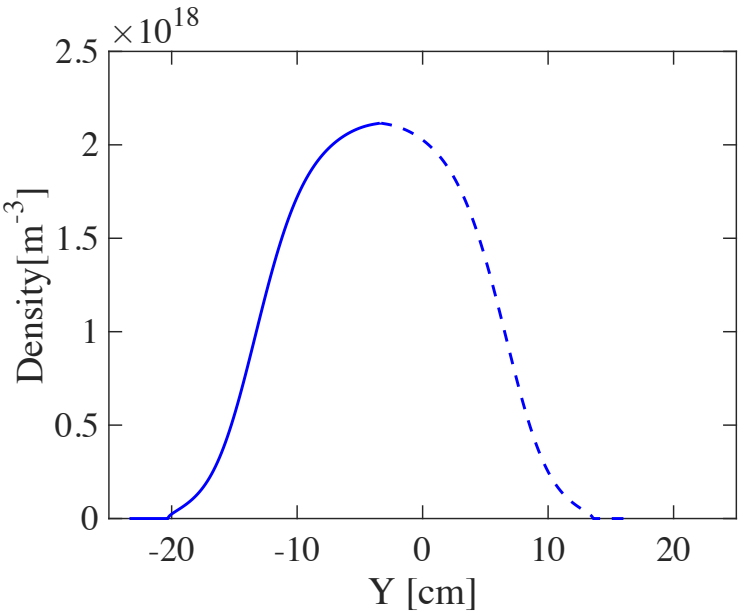

Figure 3.20 The density profile calculated with Eq. 3.31 using the fitting line as shown in Fig. 3.19.

3.3.2 Measurement of Density Fluctuation

The density fluctuations associated with the ICRF waves have been reported in previous studies [56-58]. To evaluate the spatial structure of the ICRF waves, a density fluctuation measurement is performed with a heterodyne reflectometer. Figure 3.21 gives a schematic drawing of the reflection of the incidence microwave near the cutoff density. If the density fluctuates, then the microwave path length L fluctuates because of the change of the reflection position. The density fluctuation level $\left|\frac{\tilde{n}}{n}\right|$ can be written as

$$\left|\frac{\tilde{n}}{n}\right| = \frac{1}{n}\frac{dn}{dr}\tilde{L} \tag{3.33}$$

and the difference of the path length ΔL can be written as

$$\tilde{L} = \frac{\lambda'}{4\pi}\tilde{\phi} \tag{3.34}$$

where λ' is the wavelength of the microwave near the cutoff layer, which is about 1.7 times the wavelength in the vacuum. In the case of O-mode microwave, the cutoff layer is determined by cutoff density n, as was explained in Section 2.3,

$$n = \frac{4\pi^2\epsilon_0 m_e}{q^2} f_{pr}^2 \tag{3.35}$$

The radial position of the measurement can be changed by the frequency of the incidence microwave. In GAMMA 10/PDX, the frequency range of applicable microwaves is X-band (8.2 GHz – 12.4 GHz), because the density in the GAMMA 10/PDX typically has a maximum of about 2×10^{18} m^3 and monotonically decreases towards the edges.

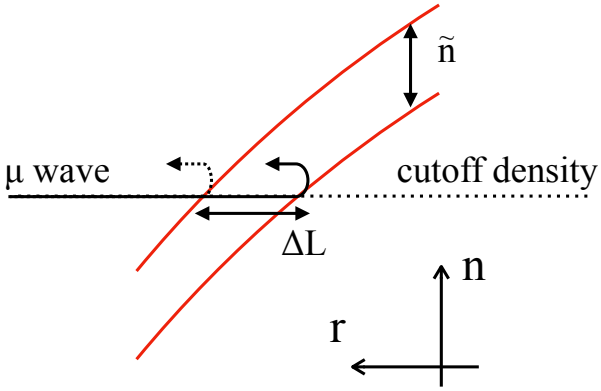

Figure 3.21 Schematic diagram of the reflection of the incidence microwave near the cutoff density.

Figure 3.22 shows a block diagram of the heterodyne reflectometer. The microwave is separated into two paths by a directional coupler. One of them is injected into the plasma and is reflected at the cutoff layer. The microwave received by the horn antenna can written by

$$A\cos\left(\omega_{pr}t+\phi(t)\right) \tag{3.36}$$

where A is the amplitude of the microwave and $\phi(t)$ is the phase shift due to plasma. The microwave from the other path is mixed with the microwave with a frequency of 150 MHz (intermediate frequency),

$$B\cos\left((\omega_{pr}+\omega_{if})t\right) \tag{3.37}$$

where B is the amplitude of the microwave. The microwaves shown in Eq. 3.36 and Eq. 3.37 are mixed and become

$$\frac{AB}{2}\left[\cos\left(\left(2\omega_{pr}+\omega_{if}\right)t+\phi(t)\right)+\cos\left(\omega_{if}t-\phi(t)\right)\right]. \tag{3.38}$$

By passing through bandpass filter, only the second term of Eq. 3.38 remain and applies to the phase detector. In addition, the output of the intermediate frequency oscillator $\cos\left(\omega_{if}t\right)$ applies to the phase detector, and the signal of

$$\begin{aligned} I(t) &= C\cos\left(\phi(t)\right) \\ Q(t) &= C\sin\left(\phi(t)\right) \end{aligned} \tag{3.39}$$

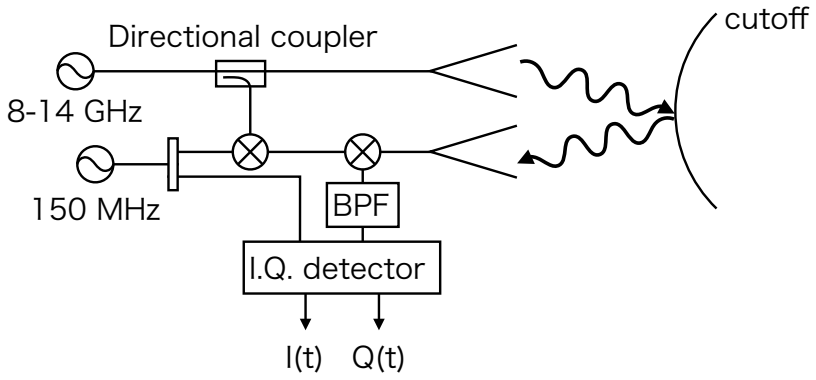

Figure 3.22 Block diagram of a heterodyne reflectometer installed in GAMMA 10/PDX.

where C is the amplitude, is obtained. The phase due to plasma $\phi(t)$ can be written as

$$\phi(t) = \tan^{-1}\frac{Q(t)}{I(t)}. \tag{3.40}$$

Phase Extraction

Figure 3.23 shows the raw data of the reflectometer on a typical discharge on the GAMMA 10/PDX, $I(t)$ and $Q(t)$ as blue and red lines, respectively. The probing frequency of the microwave is 10.0 GHz and a horn antenna located at z = 52 cm is used. Figure 3.24 shows the Lissajous figure of the $I(t)$ and the $Q(t)$ and the colors indicate the number of the data points. The amplitude of the microwave remains non-zero and the

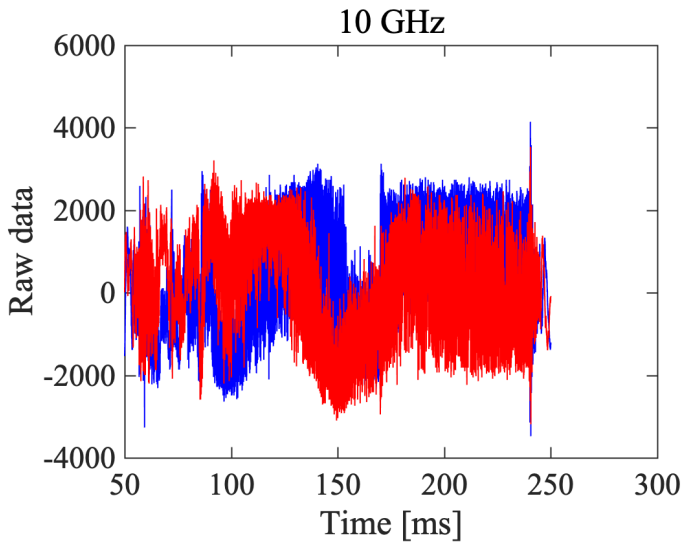

Figure 3.23 Raw data of the phase detector output signal. The probing frequency of the microwave is 10 GHz and a horn antenna located at z = 52 cm is utilized.

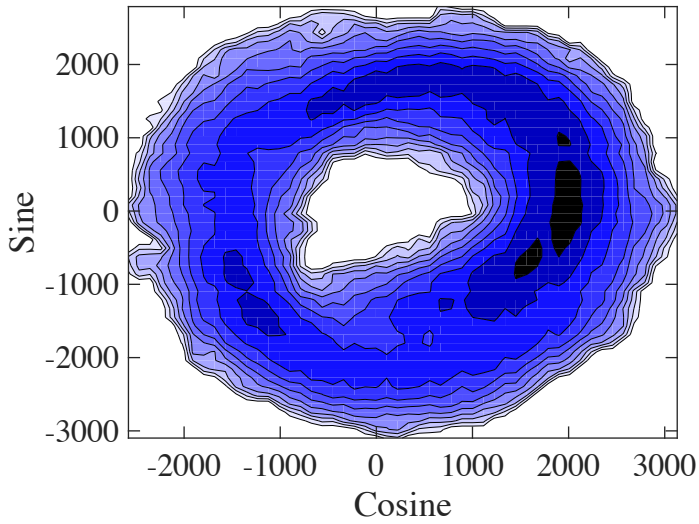

Figure 3.24 Lissajous figure of $I(t)$ and $Q(t)$ shown in Fig. 3.23. The dark colors indicate more data points.

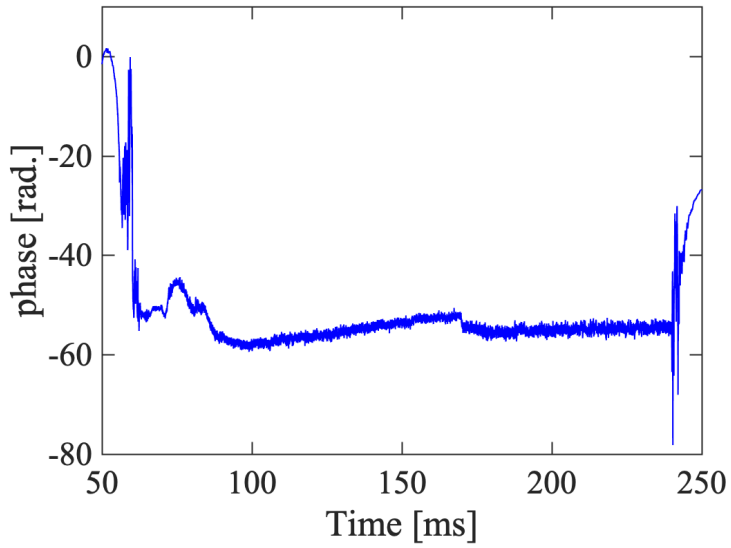

Figure 3.25 Phase due to plasma $\phi(t)$ is obtained by phase extraction with the measurement result as shown in Fig. 3.23.

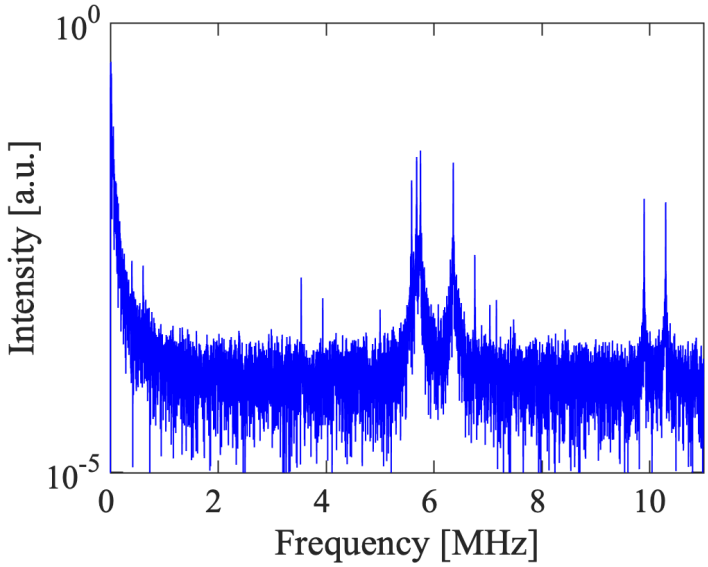

Figure 3.26 Fourier spectrum of the $\phi(t)$ on a typical discharge on the GAMMA 10/PDX.

change of the phase component is observed. The phase extraction is performed with Eq. 3.40 and the phase due to plasma $\phi(t)$ is obtained as shown in Fig. 3.25. The density fluctuation associated with the ICRF waves is obtained by performing fast Fourier transformation. Figure 3.26 shows a Fourier spectrum of the $\phi(t)$. The density fluctuation associated with the ICRF waves from RF1 (10.3 MHz and 9.9 MHz) and RF2 (6.36 MHz) is observed. In addition, the information of simultaneously excited Alfvén Ion Cyclotron (AIC) waves and the waves excited by wave-wave interactions are obtained.

The phase extraction become difficult when the probing frequency is increased. Figure 3.27 and Fig. 3.28 show the Lissajous figure of the $I(t)$ and $Q(t)$ and $\phi(t)$, respectively, observed with an identical discharge as that in Fig. 3.24. When the amplitude of the output signal becomes zero, the phase runaway phenomenon is

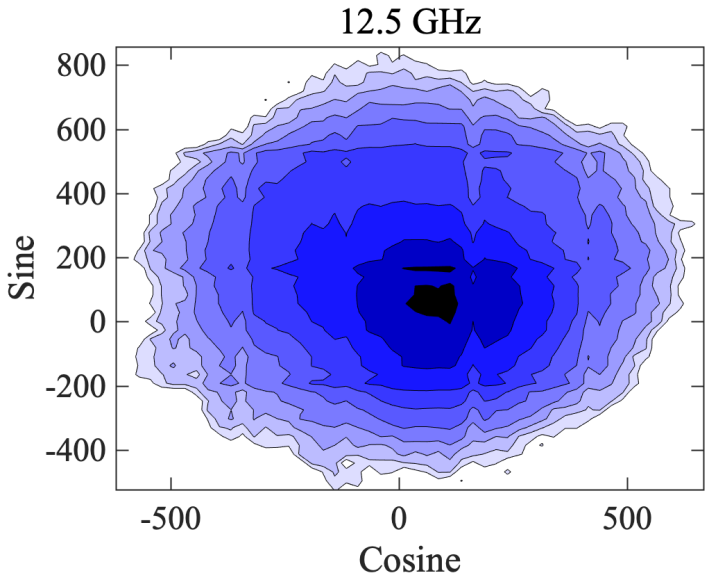

Figure 3.27 Lissajous figure of the $I(t)$ and $Q(t)$ observed with the probing frequency of 12.5 GHz.

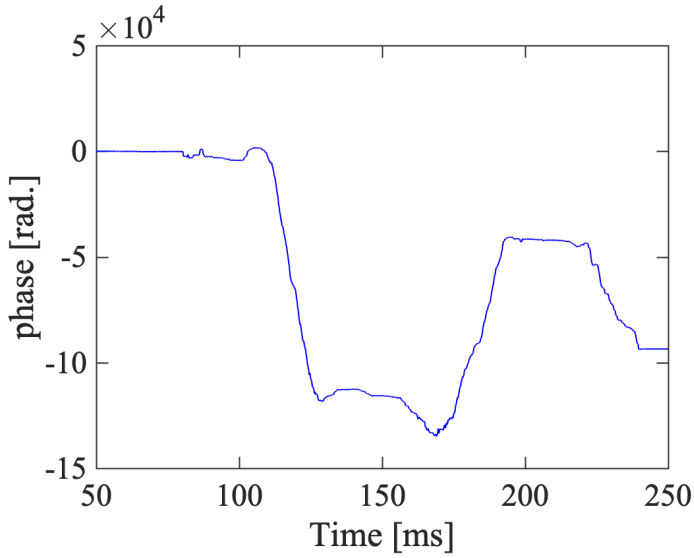

Figure 3.28 Phase due to plasma $\phi(t)$ is obtained by phase extraction with the measurement result as shown in Fig. 3.27.

observed. This suggests that the decrease of the amplitude of the signals is due to the receding cutoff layer and disappearing cutoff layer. In this study, measured ϕ_{plasma} obtained from the phase extraction is used.

3.4 Measurement of Input Power and Radiated Power from ICRF Oscillator

Figure 3.29 shows a circuit model for the measurement of the input power and the radiated power from an ICRF oscillator. The ICRF wave is transmitted from the oscillator to the circuit, which consists of a matching circuit, ICRF antenna, and plasma.

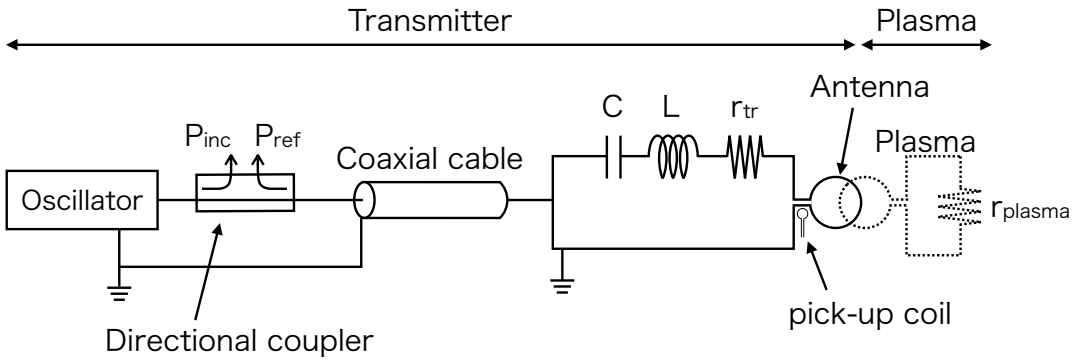

Figure 3.29 Schematic diagram of the circuit model for the measurement of the input power and the radiated power from ICRF oscillator.

Input Power

Here, the input power is measured with the directional coupler installed next to the oscillator. Forward power P_{inc} and reflected power P_{ref} are measured and the input power of the ICRF wave P_{in} is defined as

$$P_{in} = P_{inc} - P_{ref}. \tag{3.41}$$

Radiated Power

The input power is absorbed with the resistance of the transmitter circuit r_{tr}, and is radiated from the antenna and absorbed by the plasma. The input power can be written as

$$P_{in} = P_{net} + P_{tr}. \tag{3.42}$$

where P_{net} is the radiated power from the antenna absorbed by the plasma and P_{tr} is the absorbed power with the resistance of the transmitter circuit. In addition, the current flowing on the circuit I_{rf} is measured with the pick-up coil installed near the antenna. Then, Eq. 3.42 is rewritten as

$$P_{in} = P_{net} + \frac{1}{2} r_{tr} I_{rf}^2. \tag{3.43}$$

The resistance of the transmitter circuit r_{tr} can be estimated with the power injection before the plasma discharge, which is called a pre-pulse. Because there is no plasma in the vacuum vessel, the input power is absorbed by the transmitter circuit:

$$P'_{in} = P'_{tr} = \frac{1}{2} r_{tr} I'^2_{rf} \tag{3.44}$$

$$r_{tr} = \frac{2P'_{in}}{I'^2_{rf}}. \tag{3.45}$$

Therefore, the radiated power is obtained by substituting Eq. 3.45 into Eq. 3.43

$$P_{net} = P_{in} - \frac{P'_{in}}{I'^2_{rf}} I_{rf}^2. \tag{3.46}$$

Antenna loading is defined as the ratio of the radiated power and the input power

$$Antenna\ Loading = \frac{P_{net}}{P_{in}} = \frac{r_{plasma}}{r_{plasma} + r_{tr}}. \tag{3.47}$$

4 EXPERIMENTAL RESULTS AND DISCUSSIONS

4.1 Enhancement of End-loss Ion Flux Using ICRF Waves

In GAMMA 10/PDX, plasmas are produced in the central cell and the anchor cells. The plasma densities are on the order of 10^{18} m^{-3}. In contrast, the plasma density at the end region where the divertor module is installed is on the order of 10^{16} m^{-3}, which is one hundredth of the plasma densities in the central cell and the anchor cells. This happens because the main plasmas are confined in the magnetic mirror configuration. Therefore, it is necessary to enhance the particle flux of the end-loss plasmas on a mirror confined plasma.

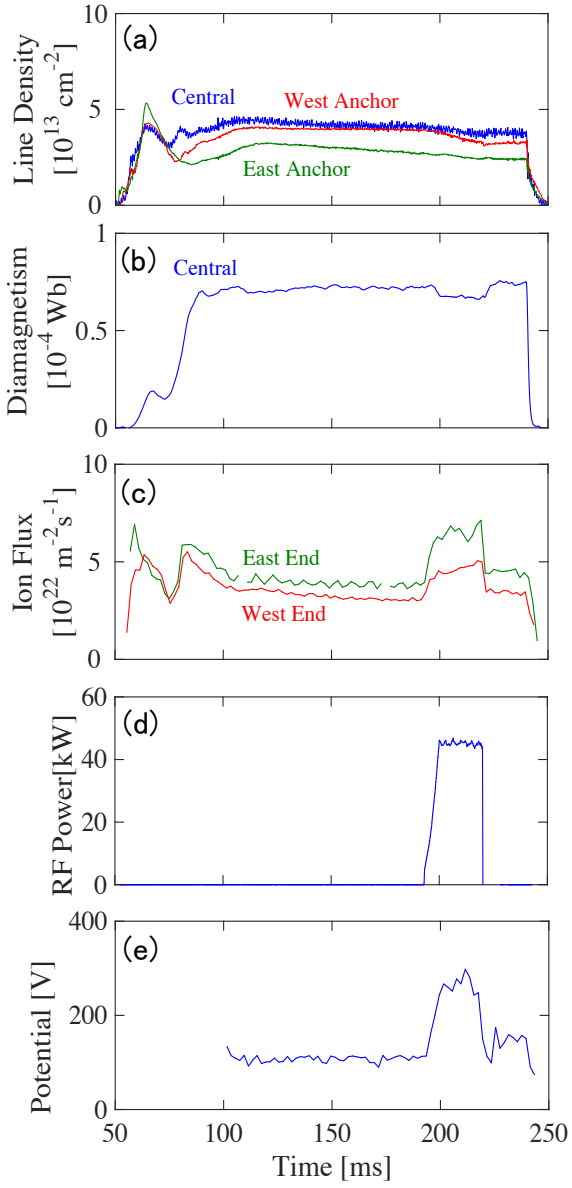

Figure 4.1 Time evolution of (a) line densities in the central cell (blue line), east anchor cell (green line) and west anchor cell (red line), (b) diamagnetism in the central cell and (c) ion currents at the east (green line) and west (red line) end regions, (d) input power of RF3 connected with the west DAT antenna and (e) the potential.

To increase the particle flux of the end-loss ions, additional heating using ICRF waves has been performed with various combinations of ICRF antennas and frequencies [59–61]. Figure 4.1 shows an example of a discharge where the ion flux increases with the additional heating. The base plasmas are produced with ICRF waves (9.9 MHz and 10.3 MHz) excited by the Type-III antennas in the central cell connected with RF1, and the ion heating in the central cell is carried out with ICRF waves (6.36 MHz) excited by DHT antennas in the central cell connected with RF2. Additional heating with the ICRF wave with a frequency of 6.0 MHz excited by the DAT antenna in the east anchor cell connected with RF3 is carried out from 190 ms to 220 ms. Given that the ICRF wave with ae frequency of 6.0 MHz only has a resonance layer at the end region, there is no resonance heating in the central cell and the anchor cells by that wave. Figure 4.1 shows (a) line densities in the central cell (blue line) and the west (red line) and east (green line) anchor cells, (b) the diamagnetism in the central cell, (c) the ion flux of the end-loss ions observed at the west (red line) and east (blue line) end regions, (d) the input power of the additional heating and (e) the potential observed with west ELIEA. The ion flux at both the end regions and the potential increase remarkably with the additional heating, although the line densities have no significant change and the diamagnetism decreases a little. This suggests that a change of the parameters excepting the line density affects the ion flux with ICRF waves.

Figure 4.2 shows the ion flux of the end-loss ions as a function of the line density in the central cell. Experimental results on the discharges for about three years are plotted. Those discharges in which the ion additional heating in the plug/barrier cell or the electron cyclotron heating is applied and/or the obstacles (e.g. probe, divertor module and so on) are inserted between the confinement region and the end region are excluded. The gray dots are data points (about 130,000 points), the blue dots show the average of the ion flux at each line density in the central cell, and the error bar shows the standard deviation. The ion flux increases with the line density increase. However, even if the line density is almost the same, the ion flux may not be same value as shown in Fig. 4.1. Figure 4.3 gives a histogram of the ion flux under the fixed line density in the central cell and the dashed lines show the average of the ion flux. Because all of the histograms have a large standard deviation, it is suggested that the ion flux of the end-loss ions is determined by several parameters and not only the line density in the central cell. To discuss the effect of ICRF wave on end-loss ion flux as shown in Fig. 4.1 and to enhance the ion flux, the relationship between the ion flux and several plasma parameters is investigated with feature selection using Least Absolute Shrinkage and Selection Operator (LASSO).

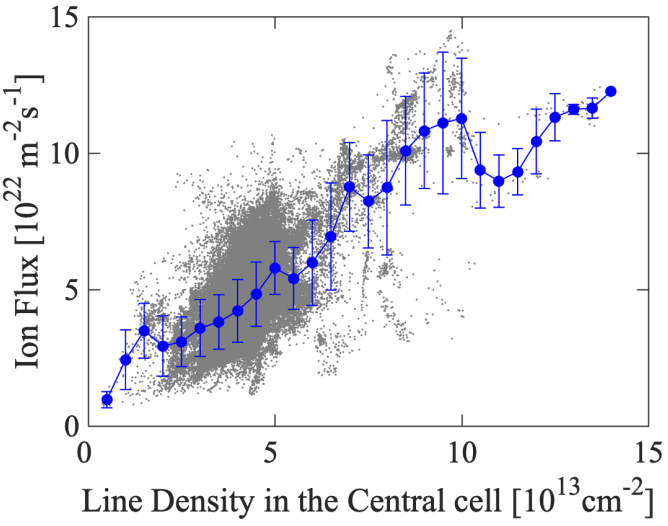

Figure 4.2 The ion flux of the end-loss ions as a function of the line density in the central cell.

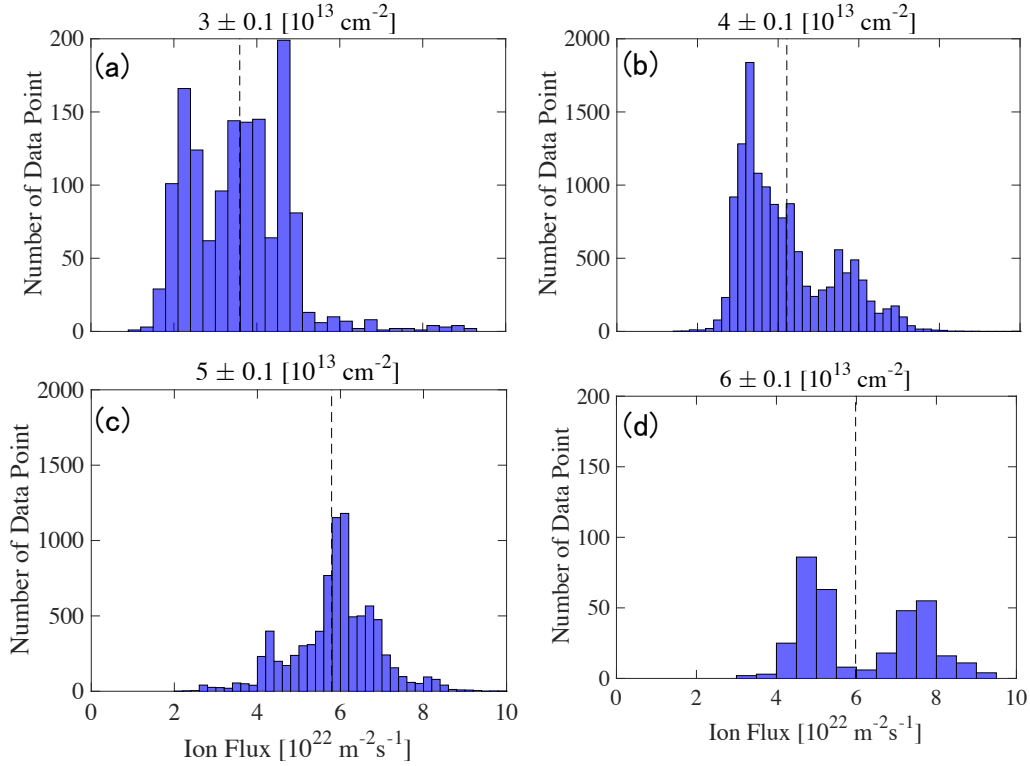

Figure 4.3 Histograms of the ion flux of the end-loss ions under fixed line density in the central cell of (a) 3 ± 0.1 × 10^{13} cm^{-2}, (b) 4 ± 0.1 × 10^{13} cm^{-2}, (c) 5 ± 0.1 × 10^{13} cm^{-2} and (d) 6 ± 0.1 × 10^{13} cm^{-2}.

4.1.1 Feature Selection Using LASSO

Feature selection is used to make a model easier and to remove variables. In this chapter, we use feature selection to make a model of the ion flux of the end-loss ions and to quantitatively discuss the effect of several parameters. The feature selection is performed with the measured values of the line densities in the central cell, both anchor cells and the west barrier cell, potential observed with west ELIEA, the diamagnetism in the central cell, and the intensity of Hα in the central cell on the discharges (as shown in Fig. 4.2). The histograms of each parameters are shown in Fig. 4.4.

Unfortunately, these measured values are not good enough to make a nonlinear model. Figure 4.5 (a) shows the potential dependence of the ion flux when the other six parameters are almost same (the difference is less than 10 %) as blue dots. The ion flux increases linearly with the increase of the potential and has variation due to noise and analyzes error from the insufficient parameters. The solid lines are fitting lines, assuming linear, quadratic, and cubic polynomials as red, green, and purple, respectively. In this case, the linear model is the most appropriate. However, the residual sum of squares (RSS) of the linear model is higher than the others, as shown in Fig. 4.5 (b). This suggests that the model is overly complex, which is called overfitting, and cannot explain the relationship between the parameters. To avoid overfitting, the ion flux model is assumed to be linear, as follows

$$\boldsymbol{y} = \boldsymbol{A}\boldsymbol{x} + \boldsymbol{\varepsilon}$$

$$y = \begin{pmatrix} y_1 \\ \vdots \\ y_n \end{pmatrix}, A = \begin{pmatrix} a_{11} & \cdots & a_{1p} \\ \vdots & \ddots & \vdots \\ a_{n1} & \cdots & a_{np} \end{pmatrix}, x = \begin{pmatrix} x_1 \\ \vdots \\ x_p \end{pmatrix}, \varepsilon = \begin{pmatrix} \varepsilon_1 \\ \vdots \\ \varepsilon_n \end{pmatrix} \tag{4.1}$$

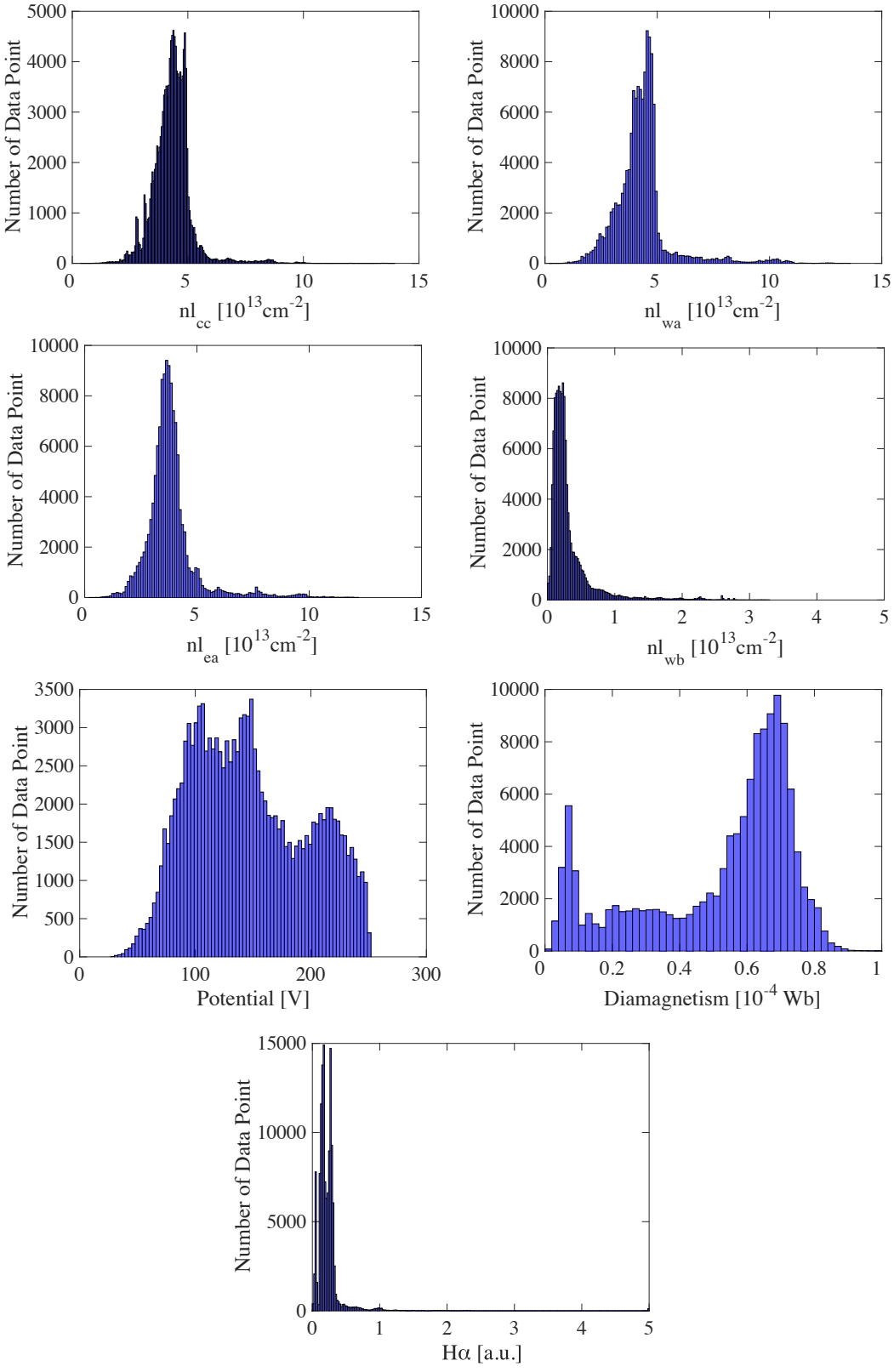

Figure 4.4 The histograms of each measured value on the discharges as shown in Fig. 4.1.2.

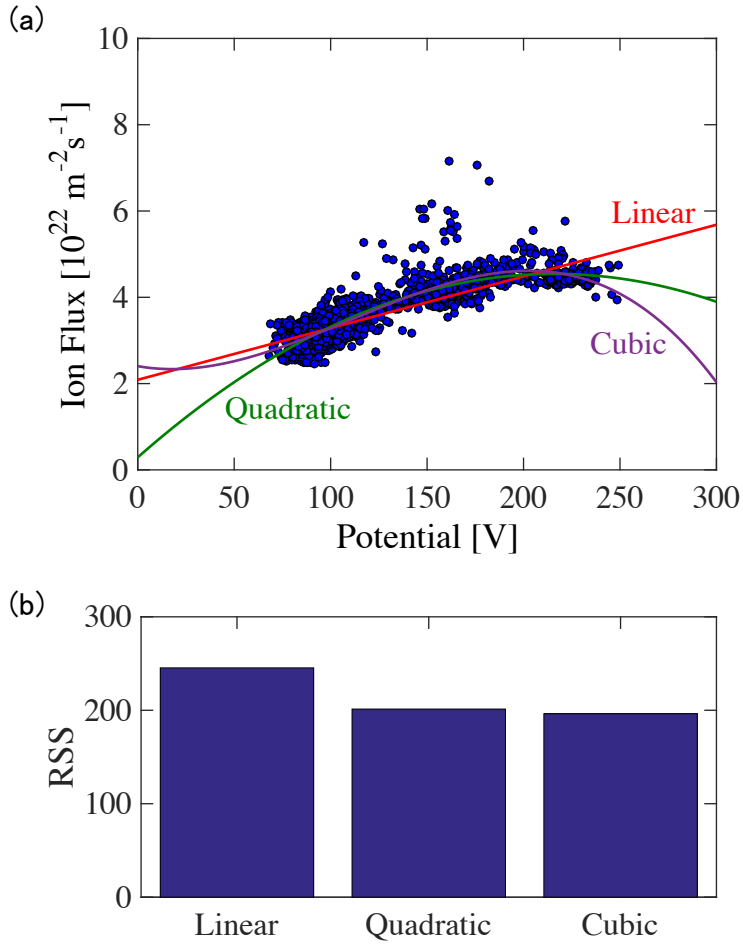

Figure 4.5 (a) The potential dependence of the ion flux when the other six parameters are almost the same (the difference is less than 10 %). (b) The RSS of the fitting lines assumed as linear, quadratic, and cubic polynomials.

where **y** is response vector, **A** is design matrix, **x** is coefficient vector and ε is error vector. In this study, **y** is the vector of the measured values of the ion flux; **A** is the matrix of the measured values of the line densities, the potential, the diamagnetism, and the intensity of Hα; and **x** is the vector of the coefficients of each measured value. The coefficient vector is determined using LASSO.

LASSO is a powerful method that perform the feature selection [62-64]. The LASSO method solves an optimization problem that has a constraint function of the sum of the absolute value of the coefficients as follows

$$\hat{\boldsymbol{x}} = \arg\min_{\boldsymbol{x}} [\|\boldsymbol{y} - \boldsymbol{A}\boldsymbol{x}\|_2^2 + \lambda \|x\|_1] \tag{4.2}$$

$$\|x\|_n = \left(\sum_{i=1}^{p} |x_i|^n \right)^{1/n} \tag{4.3}$$

where λ (≥ 0) is a constant value that control the strength of penalty, p is length of the vector of $\boldsymbol{x}$. Figure 4.6 shows a LASSO estimation diagram. Circles around $\hat{\boldsymbol{x}}$ show the contour of the least square error function and the diamond shows the constraint function. The LASSO method finds the first point where the error function border touches the constraint function. In the case shown in Fig.4.6, the position of the star at the corner of the diamond shows that coefficient x_2 of zero is selected. Those variables that have a non-zero coefficient after the

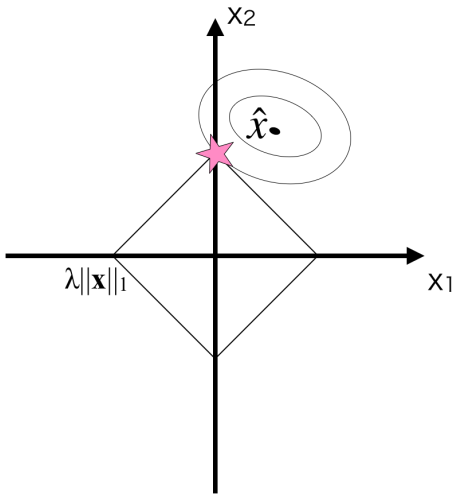

Figure 4.6 LASSO estimation diagram, the contours of error and constraint functions are plotted.

feature selection process are selected to be part of the model. In this study, the coefficient vector is estimated using a coordinate descent algorithm. The standardization of the design matrix **A**, and the average centering and the standardization of **A** and the response vector **y** is performed as follows

$$\sum_{i=1}^{n} y_i = 0, \sum_{i=1}^{n} a_{ij} = 0, \frac{1}{n}\sum_{i=1}^{n} a_{ij}^2 = 1, j = 1, \cdots, p \tag{4.4}$$

Figure 4.7 shows the coefficients of each measured value as a function of the strength of penalty λ. The coefficients become zero with the increase of λ. The potential and the line densities positively and the diamagnetism and the intensity of Hαnegatively affect to the ion flux steadily. Figure 4.8 shows the RSS as a function of λ,

$$\text{RSS} = \sum_{i=1}^{n} \varepsilon_i^2 \tag{4.5}$$

Figure 4.8 (b) gives an enlarged view of the above. The RSS decreases with a decrease of λ because the model becomes complex. However, when the λ is too small, the model cannot explain the relationship between parameters, due to overfitting. To choose the appropriate value of the λ, we use the *K*-fold cross-validation and one standard error rule.

In the *K*-fold cross-validation method, the measured values are split into k number of subsets and the feature selection process is carried out with the all but one of the subsets. The process is iterated k times with a different subset reserved for each time. The RSS of the model and the subset which is left is calculated k times and the final RSS of this model is determined by averaging the RSSs (k patterns). In this study, the *K*-fold cross-validation method is carried out with k = 10. The error bar shown in Fig 4.8 is the standard deviation. The simplest model that has an RSS that is no more than one standard error above the model with the lowest RSS (one standard error rule) is selected. In this case, the λ of 3×10^{-6} is chosen.

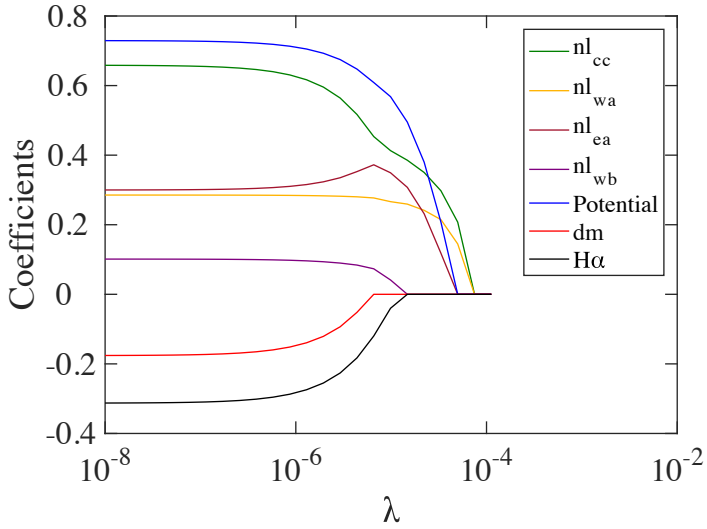

Figure 4.7 The coefficients of each measured value as a function of the strength of penalty λ.

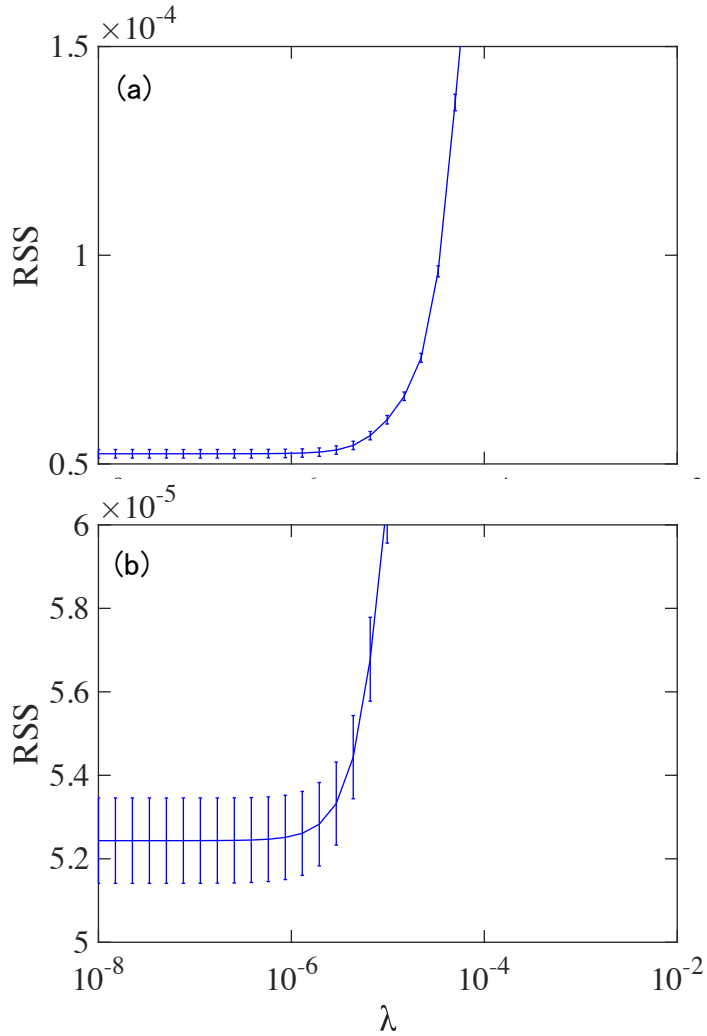

Figure 4.8 (a) The average of the RSS calculated by *K*-fold cross-validation as a function of λ and (b) enlarged view. The error bar shows the standard deviation of RSSs.

The coefficients of each variable (measured values) are shown in Fig. 4.9. Every variable has non-zero coefficient, and the line density in the central cell and the potential is effective in this model. The coefficients of the line densities in the anchor cells and the west barrier cell are about half and 1/7 of the coefficient of the line density in the central cell, respectively. The diamagnetism and the intensity of Hα negatively affect the ion flux. Figure 4.10 shows the response vector **y** (the ion flux after average centering) as a function of the product of design matrix **A** and coefficient vector **x** (**Ax**). Here, **y** is the experimental results of the ion flux and **Ax** is the result of the model. The gray dots plot every data point, the blue dots show the average of the **y** at each **Ax** and the error bar shows the standard deviation. The black-dashed line shows **y** = **Ax**. The blue dots are close to the black line; therefore, this model is able to show the tendency of the ion flux. Figure 4.11 shows the histogram of the ion flux under the fixed **Ax** and the dashed lines show the average of the ion flux. The standard deviation becomes smaller than the histograms, as shown in Fig. 4.3.

The relationship between each variable and the ion flux is estimated with feature selection using LASSO. Every seven variables have a linear relation with the ion flux, but the physics of the influence of each variable on the ion flux are not clear. In addition, it is possible that a high correlation between the parameters that are not the ion flux would cause the non-zero coefficient of the parameters. If this is the case, then it is unclear that the parameters as shown in Fig. 4.9 are significant variables that have independent information. It is also possible for the parameters to change as a result of the change of the ion flux. Hence, it is necessary to consider choosing the parameter to enhance the ion flux.

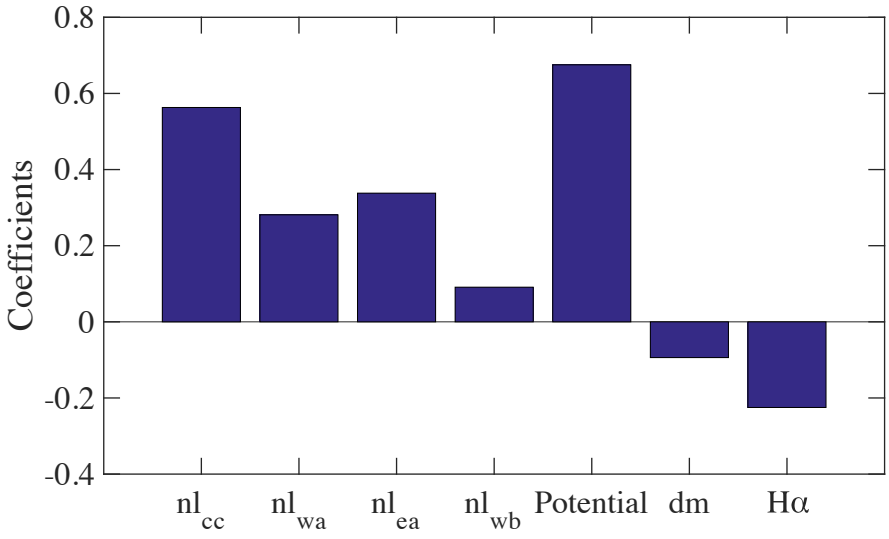

Figure 4.9 The coefficients of the parameters of the measurements; the line densities in the central cell (nl_{cc}), the west anchor cell (nl_{wa}), the east anchor cell (nl_{ea}), the west barrier cell (nl_{wb}), the potential observed with west ELIEA, the diamagnetism in the central cell (dm) and the intensity of Hα in the central cell.

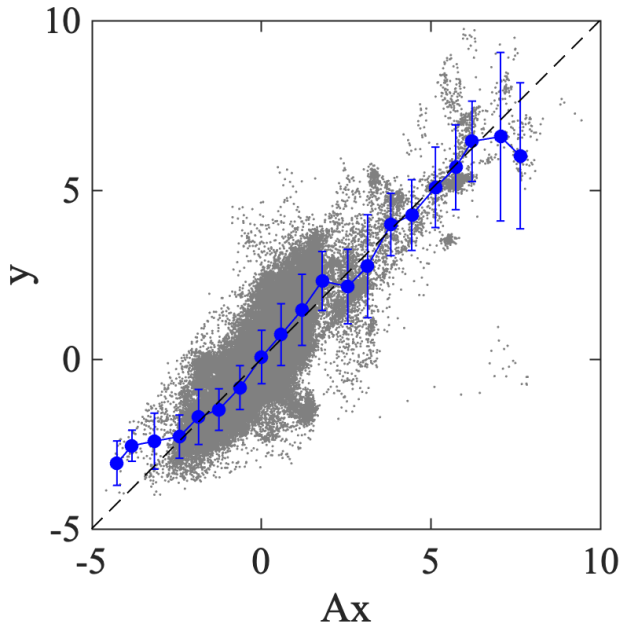

Figure 4.10 The response vector **y** (the ion flux after average centering) as a function of the product of design matrix **A** and coefficient vector **x** (**Ax**).

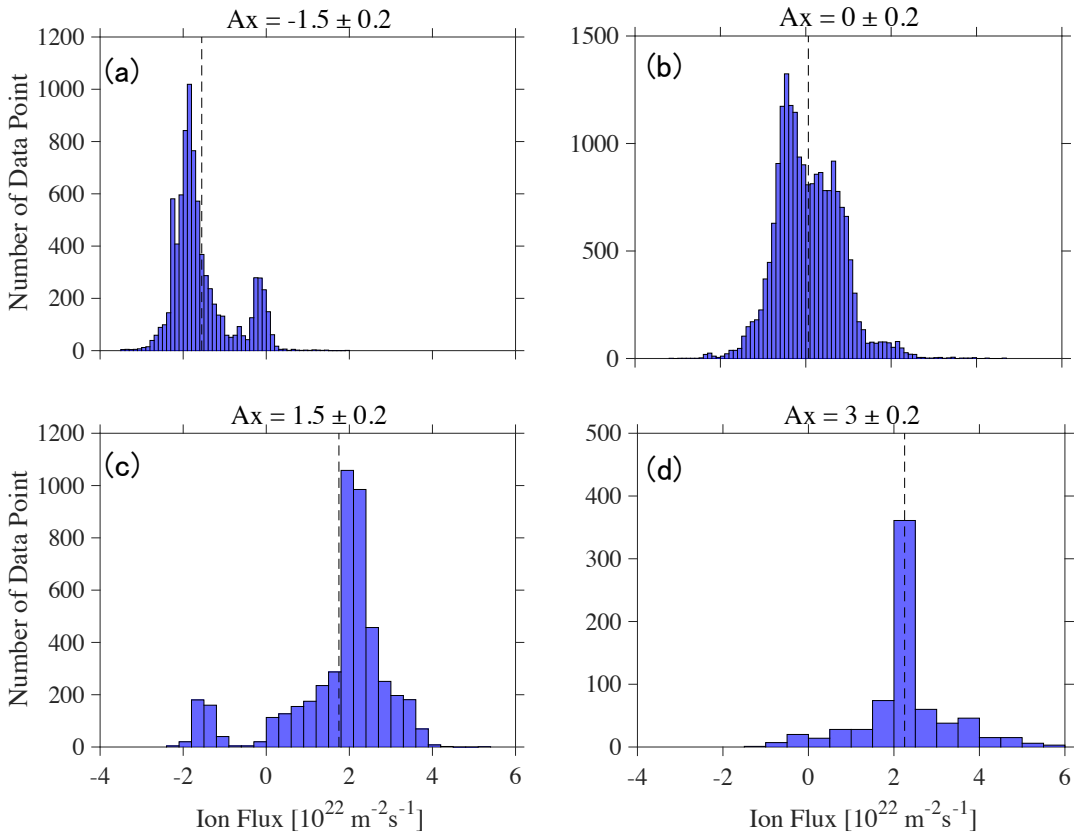

Figure 4.11 Histograms of the ion flux of the end-loss ions under fixed Ax of (a) -1.5 ± 0.2, (b) 0 ± 0.2, (c) 1.5 ± 0.2 and (d) 3 ± 0.2.

i) Influence of Density

As was explained previously, the plasma density positively affects the ion flux of the end-loss ions. The ion flux increases with the increase of the density because of the increase of the plasma production and the ions dropping into the loss cone. These processes can occur at any location on the same magnetic tube where the ion flux is being observed with ELIEA. To confirm the influence of the line densities in each cell on the ion flux, it is necessary to measure the axial profile of the density. The density profile is measured with an interferometer and a reflectometer.

Figure 4.12 shows the line densities in the central cell (blue line), mirror throat of the central cell (purple line), east (green line) and west (red line) anchor cells, west plug/barrier cell (barrier as brown line and plug as black line) and the diamagnetism in the central cell in the typical discharge on GAMMA 10/PDX. The plasma is produced with RF1 connected to Type-III antennas in the central cell and the ion heating is carried out with RF2 connected to DHT antennas in the central cell. The density profiles are observed between 150–160 ms while the plasma parameters are kept constant. To estimate the axial profile of density, the radial profiles at the locations of the interferometers and reflectometers are analyzed.

First, the radial profile of the density near the center of the central cell (z = -52 cm) is observed with an interferometer. Radial scanning of the line density has been carried out by changing the position of lay of

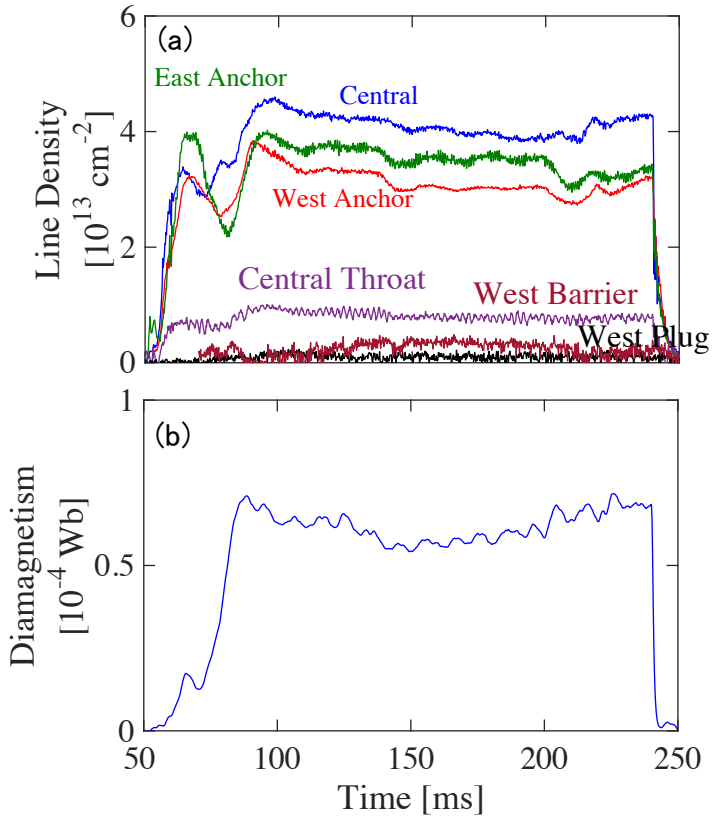

Figure 4.12 Time evolution of (a) line densities in the central cell (blue line), mirror throat of the central cell (purple line), east (green line) and west (red line) anchor cells, west plug/barrier cell (barrier as brown line and plug as black line) and (b) the diamagnetism in the central cell in the typical discharge on GAMMA 10/PDX.

microwave shot-to-shot in a series of identical discharges. Figure 4.13 shows the line densities of each position of the y-axis. Figure 4.14 shows the averages of the line densities between 150 and 160 ms as red dots and the blue line describes their fitting line. The radial density profile is obtained by Abel inversion, as shown in Fig. 4.15. The peak density is about 2×10^{18} m^{-3} and the plasma is shifted about -3 cm along the y-axis.

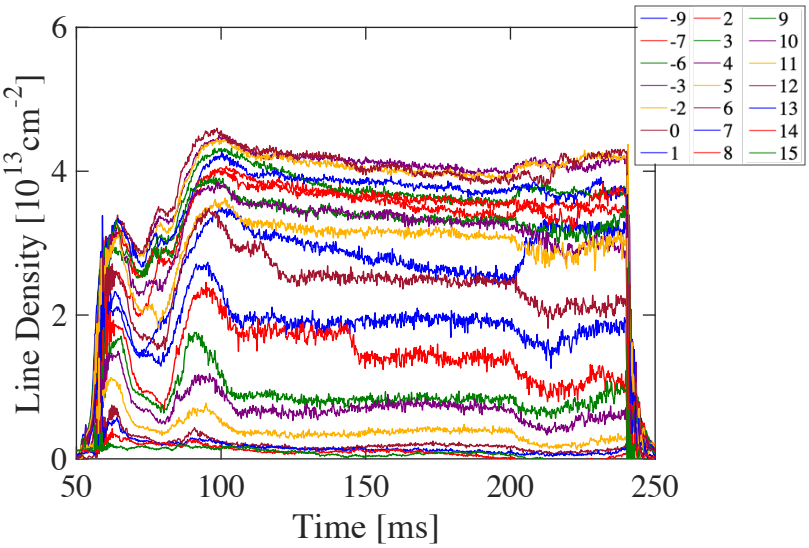

Figure 4.13 The line densities in the central cell on each position of y-axis in a series of identical discharges.

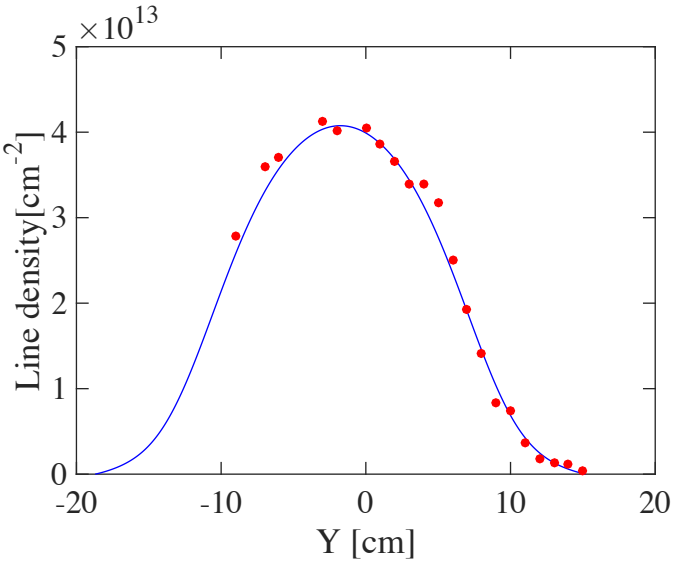

Figure 4.14 The averages of the line densities between 150 and 160 ms on the discharges as shown in Fig 4.13, the red dots and the blue line describes their fitting line.

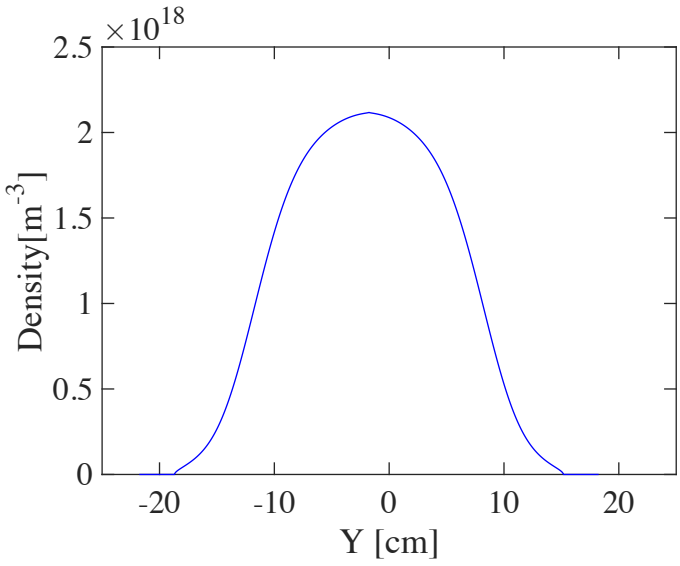

Figure 4.15 Radial density profile at z = -52 cm (near the center of the central cell) observed with an interferometer.

Second, we estimate the radial density profiles in mirror throat of the central cell (purple line, z = -307 cm), east (green line, z = -520 cm) and west (red line, z = 520 cm) anchor cells, west plug/barrier cell (barrier as brown line, z = 866 cm and plug as black line, z = 967.5 cm) with interferometers, as shown in Fig. 4.16. It is assumed that the shape of the radial profile is the same as the profile in the central cell along the magnetic field lines. In addition, the radial profiles are obtained by multiplying the profile to match the line densities.

Finally, the radial density profiles in the central cell at z = 52, 82, 112, 142 and 193 cm are observed with a reflectometer. Fig. 4.17 indicates the phase due to plasma (ϕ_{plasma}) observed with a homodyne FM reflectometer with a horn antenna located at z = 52, 82, 112, 142, 193 cm as blue, red, green, purple and brown solid lines, respectively. The probing frequency of the FM reflectometer is swept from 9 to 14 GHz. Figure 4.17 (b) is an enlarged view of the above. The gradient of the phase increases with an increase of the probing

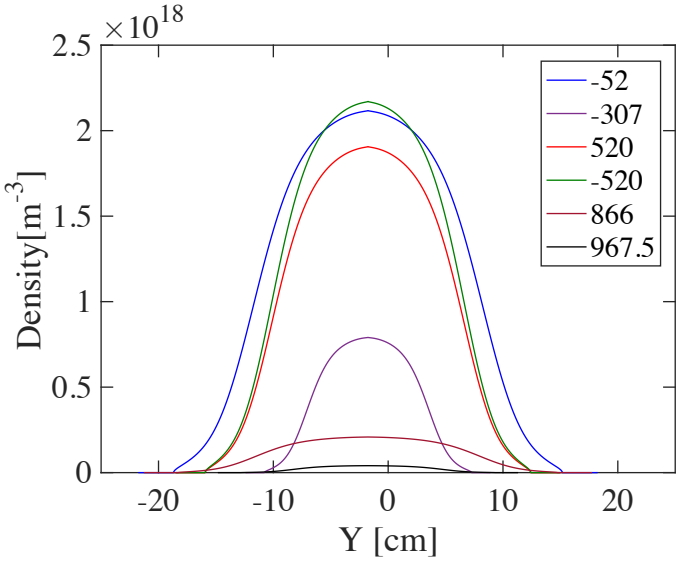

Figure 4.16 Radial density profile at each location of the interferometer.

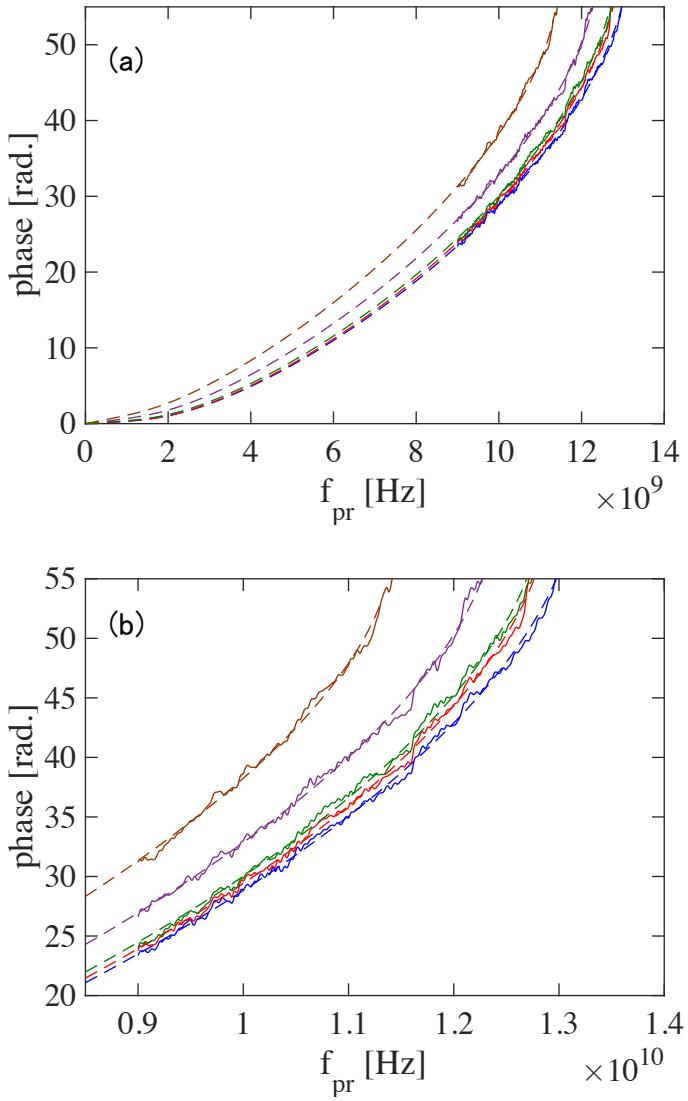

Figure 4.17 (a) The phase due to plasma and (b) enlarged view observed with the horn antennas at z = 52, 82, 112, 142, and 193 cm as blue line, red line, green line, purple line, and brown line, respectively. The dashed lines show the fitting lines.

frequency and the phase extraction cannot be performed above a certain frequency because the amplitude of the beat signal is under the noise level. In addition, this frequency decreases when the measurement is made near the mirror throat. This suggests that the phase extraction cannot be performed when the cutoff layer disappear, and the plasma density decreases near the mirror throat.

The dashed lines show the fitting lines of the measured values. The plasma density under 1×10^{18} m^{-3} shows that the cutoff density of O-mode microwave with the frequency of 9 GHz is assumed to have the same shape as the plasma density observed with interferometer (z = -52 cm) as shown in Fig 4.15. Figure 4.18 shows the plasma densities of the fitting lines at each location. The plasma density at z = 52 cm is almost that same as the plasma density observed with an interferometer at z = -52 cm. The plasma density decreases from 2.1×10^{18} m^{-3} at z = 52 cm and to 1.6×10^{18} m^{-3} at z = 193 cm.

Figure 4.19 shows the strength of the magnetic field on the z-axis, the peaks of the plasma density observed with an interferometer and a reflectometer are shown as a blue line and green dots, respectively. The red line indicates that the axial density profile smoothly connects the green dots in consideration of the magnetic field

strength. The plasmas are mainly confined in the central cell and the anchor cells, where the plasma production is performed with ICRF waves.

As the line density changes, the overall axial density profile in each cell changes. Also, the ions can loss to the end region at any location on the same magnetic tube. Hence, the coefficient of each line density is different

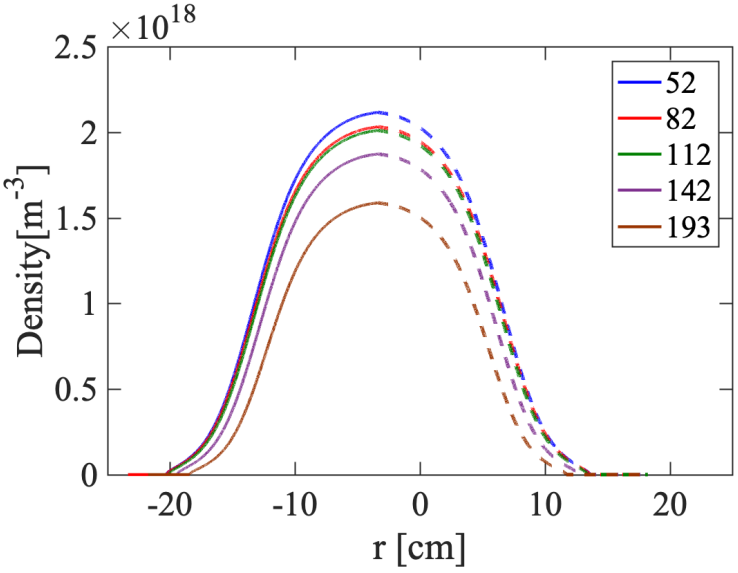

Figure 4.18 Radial density profile observed with FM reflectometer at each location of the horn antennas.

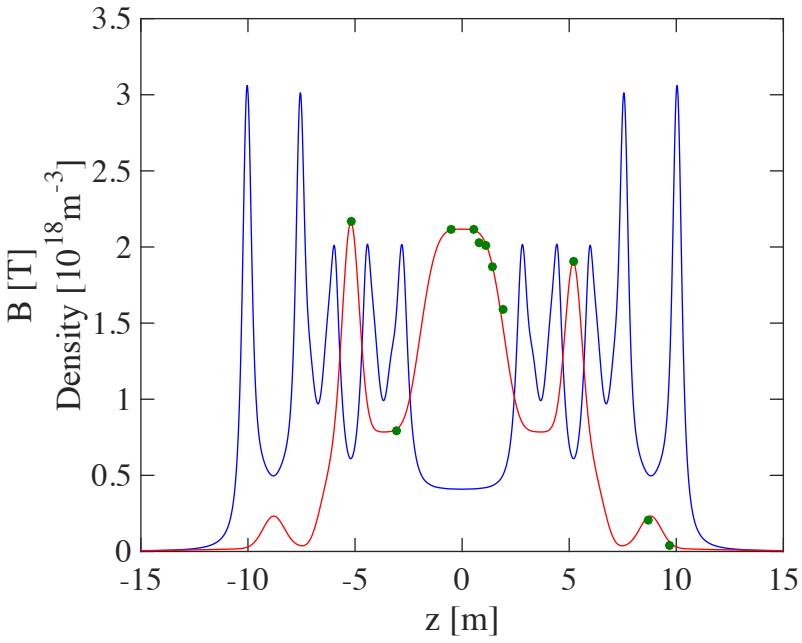

Figure 4.19 Axial density profile observed with FM reflectometer and interferometer. The blue line describes the magnetic field strength, the green dots are the measured values. The red line indicates that the axial density profile smoothly connects the green dots in consideration of the magnetic field strength.

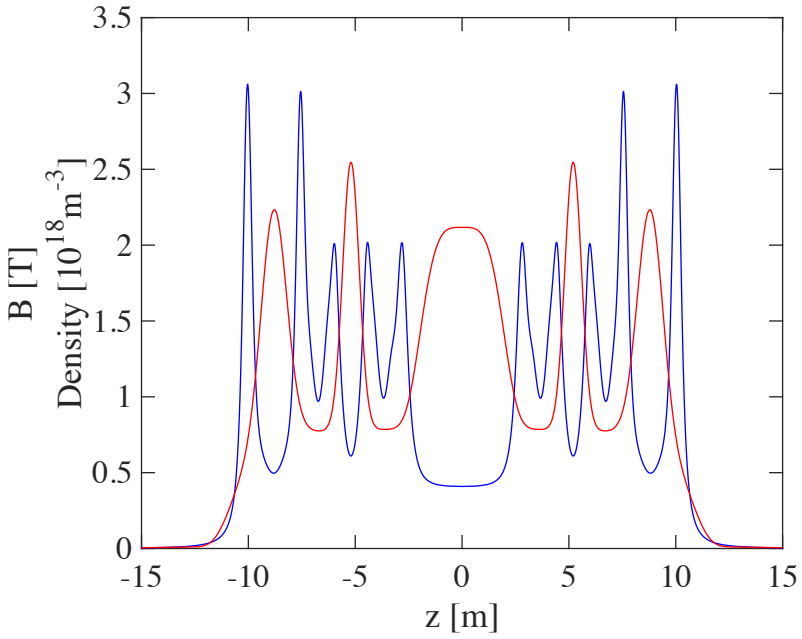

Figure 4.20 Axial density profile assuming that the line densities in the central cell, the anchor cells, and the barrier cells are same.

between each cell because the number of ions in the magnetic field tube is different. In order to compare the line density and the number of ions in the magnetic field tube, the axial density profile is integrated at each cell under the line density is same as shown in Fig. 4.20. If the line densities between the central cell, anchor cell and the plug/barrier cell are the same, the ratio of the number of the ions in those cells is 1: 0.45: 0.38. In addition, the loss cones at the anchor cells and the plug/barrier cells are larger than that in the central cell. The ratio of the dimension of the loss cone is 1: 1.50: 1.23 under uniform potential profile.

The ratio of the coefficient of the line density in the central cell, the west anchor cell, the east anchor cell, and the barrier cell is 1: 0.50: 0.60: 0.16 as shown in Fig. 4.9. The difference between the coefficient of the line density in the central cell and the anchor cells can be explained with the difference of the number of the ions in those cells and the dimension of the loss cone. In contrast, the coefficient of the line density in the plug/barrier cell is too small. In normal discharge on GAMMA 10/PDX, the plasmas are mainly produced in the central cell and the anchor cells. Also, the data of the ion flux with the additional heating in the plug/barrier cell is excluded on feature selection. It is suggested that the line density in the barrier cell increase because of the increase of the plasmas flowing from the central cell and the anchor cells not the increase of the plasma production in the plug/barrier cell. Hence, the line density in the plug/barrier cell changes as a result of the change of the ion flux. It is suggested that the increase of the plasma density with the increase of the plasma production is necessary for enhancement the ion flux of the end-loss ions.

ii) Influence of Potential

The potential is the variable that has the most influence on the ion flux in feature selection. An increase of the potential is observed in the experiments of additional heating with an ICRF wave with a frequency of 6.0 MHz as shown in Fig. 4.1. The potential increase due to ICRF waves has been discussed in previous works. In GAMMA 10/PDX, the potential is increased with additional heating using the anchor antennas, due to the radial transport near the anchor antenna with a non-axisymmetric magnetic configuration [65].

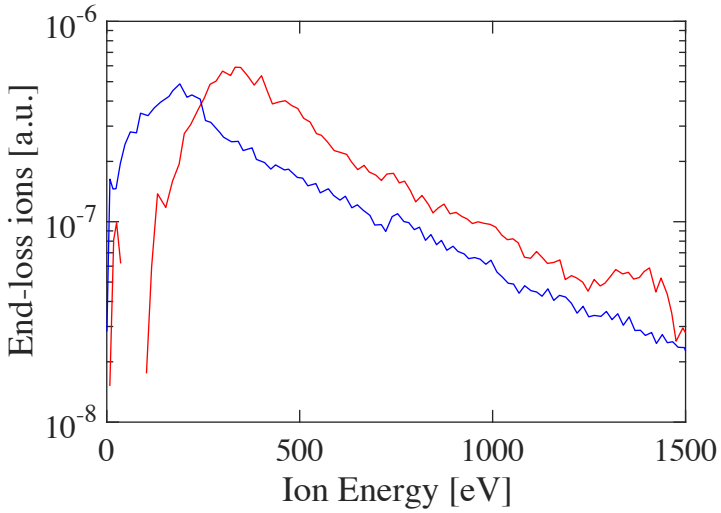

Figure 4.21 Energy distribution of the end-loss ions observed at the west end region with ELIEA on the discharge as shown in Fig 4.1. The blue and red lines show the energy distributions without additional heating (170 – 190 ms) and with additional heating (200 – 220 ms), respectively.

Figure 4.21 shows the energy distribution of the end-loss ions observed with ELIEA at the west end region on the same discharge as shown in Fig. 4.1. The blue and red lines show the energy distributions without (170 – 190 ms) and with (200 – 220 ms) additional heating, respectively. The energy distribution shifts from the low-energy region to the high-energy region and an enhancement of the end-loss ions is clearly observed. The end-loss ions should be enhanced with the potential increase in the confinement region because the loss cone of the ions expands with the potential increase.

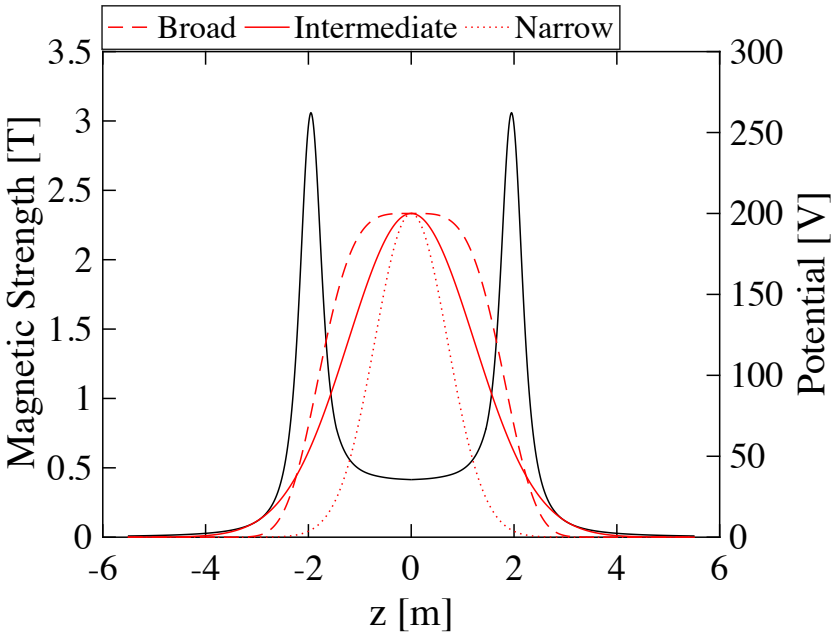

Figure 4.22 Magnetic field strength and potential profiles used in simulation as black line and the other color lines, respectively.

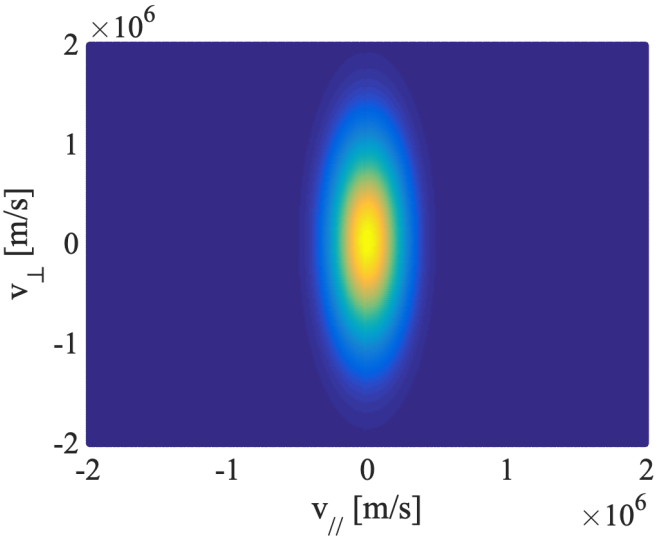

Figure 4.23 Energy distribution in the center of the mirror using the calculations. The perpendicular ion temperature of 4500 eV and the ion temperature anisotropy $T_{i\perp} / T_{i//}$ is 15.

To evaluate the influence of the increase of the potential, the orbit of the ions in a one-dimensional magnetic field is traced from the center of the mirror cell to the end region. For simplicity, it is assumed that the ions are produced at the center of the mirror cell and then move to the end region. The velocity of the ions is determined by the change of the magnetic field strength and the difference of the potential according to the law of conservation of energy and magnetic moment. Collisionless plasma is assumed because the ion-ion collision time is about 100 times longer than the average transport time of the ions from the central cell to the end region in typical discharges in GAMMA 10/PDX. The ion current is estimated by dividing the number of the ions by their transport time from the center of the mirror cell to the end region. Figure 4.22 shows the magnetic field strength and potential profiles used in the simulation as black lines and the red lines, respectively. Three types of potential profiles are simulated: broad type, intermediate type, and narrow type, which are shown as dashed line, solid line, and dotted line, respectively. The increase of the potential is simulated by multiplying the profile. Figure 4.23 shows the energy distribution of the ions; the energy distribution is Maxwell distribution with the perpendicular ion temperature of 4500 eV and a strong ion temperature anisotropy of $T_{i\perp} / T_{i//} = 15$, as observed in the typical discharges. The colors describe the number of the ions at the center of the mirror cell.

Figure 4.24 shows the energy distribution of the ions in the loss cone with a narrow potential profile with a center potential of (a) 50 V and (b) 250 V. The gray region describes the trapped region. The expansion of the loss region with an increase of the potential can be observed. In addition, the decrease of the transport time enhances the ion flux of the end-loss ions. Figure 4.25 shows the normalized ion flux of the end-loss ions as red lines. The ion flux increases almost linearly with the increase of the potential. The blue dots are the experimental results of the ion flux under $\mathbf{A}_{:,-j}\mathbf{x}_{-j}$ fixed at zero, where j is the column number of the potential. $\mathbf{A}_{:,-j}$ is the matrix, excluding the j column. This means that the influence of the other parameters is almost the same. The black-dashed line describes the results of the feature selection. The result of the orbit simulation can explain the coefficient of the potential on the feature selection.

Normally, the density decreases with the expansion of the loss cone, and the decrease of the transport time and the ion flux of the end-loss ions does not increase unless the increase of the plasma production. In GAMMA 10/PDX, the plasmas are produced with the ICRF waves and the density stays constant because of the eigenmodes formation [66]. Therefore, the plasma production increases until the density becomes constant and the ion flux increases with the increase of the potential.

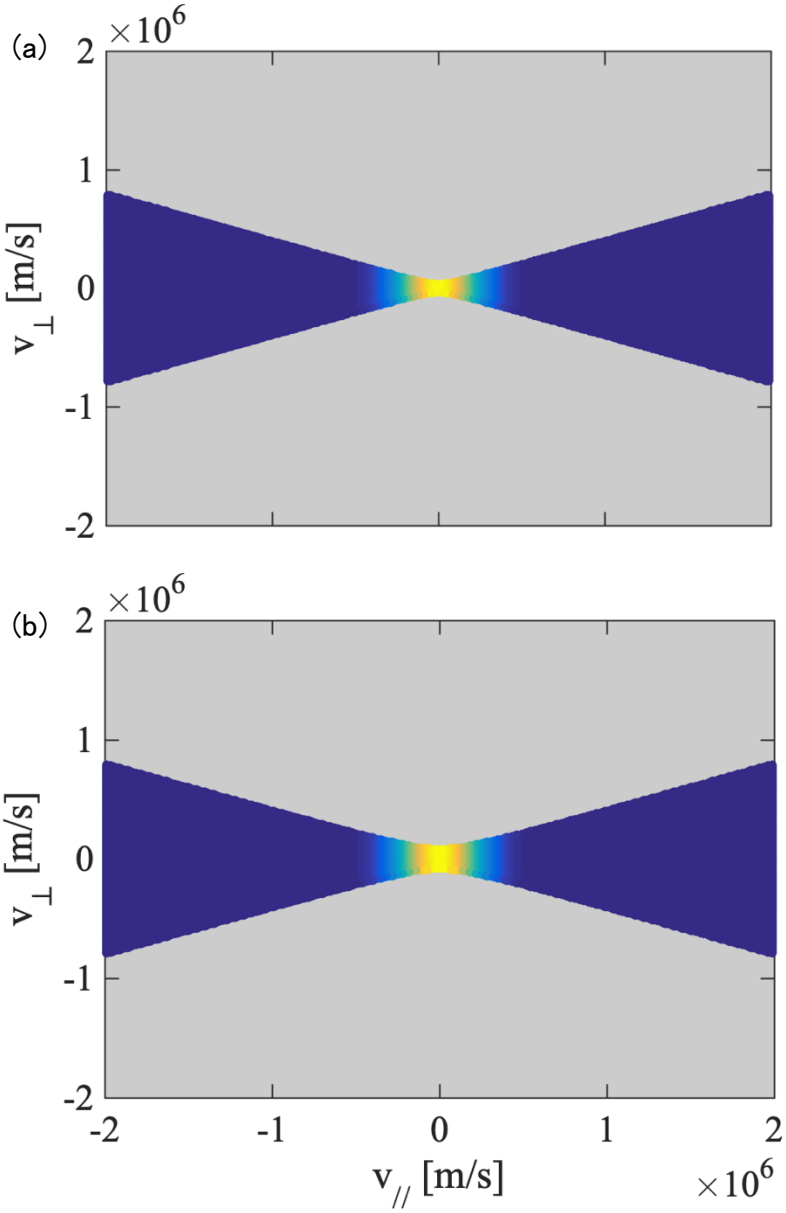

Figure 4.24 Energy distribution of the ions in the loss cone with the potential profile, as indicated with (a) blue line and (b) yellow line in Fig. 4.1.22. The gray region describes the trapped region.

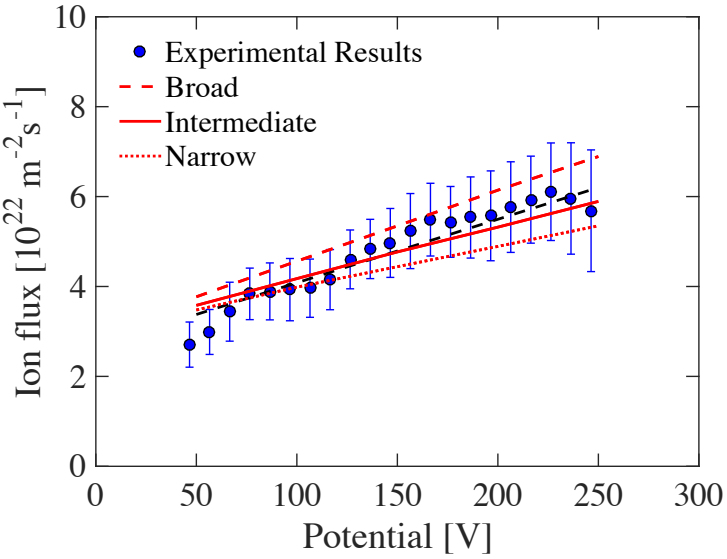

Figure 4.25 Experimental result of the ion flux under $\mathbf{A}_{:,-j}\mathbf{x}_{-j}$ fixed at zero as a function of the potential, shown as blue dots. The dashed line indicates the coefficient of the potential as shown in Fig. 4.9. The solid line shows the normalized result of the calculation.

iii) Influence of Diamagnetism

In normal discharge in GAMMA 10/PDX, the diamagnetism in the central cell mainly consists of the ion pressure, and the diamagnetism increases with ion cyclotron resonance heating using the ICRF waves with a frequency of 6.36 MHz. In the discharge shown in Fig.4.1, the additional heating is performed using an ICRF wave with a frequency of 6.0 MHz. As was explained earlier, this ICRF wave has no resonance layer except at the end region and has almost no direct impact on the diamagnetism. Figure 4.26 shows the radiated power of ICRF waves of 6.36 MHz which are used for ion heating. The radiated power of these ICRF waves has no significant change under additional heating between 190–220 ms. Hence, the condition of ion heating in GAMMA 10/PDX is almost the same with and without additional heating. This suggests that diamagnetism decreases as a result of the increase of the ion flux because of ion confinement deterioration.

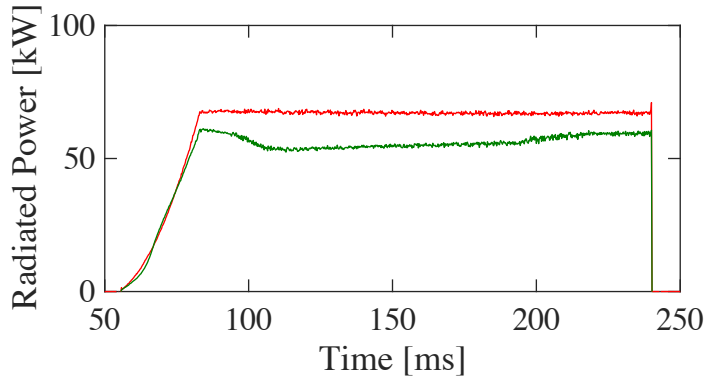

Figure 4.26 Radiated power of RF2 on the discharge as shown in Fig. 4.1. The green and red lines describe the radiated power of east and west DHT antennas, respectively.

iv) Influence of Neutral Gas

The intensity of Hα, which indicates the density of neutral gas, negatively affects the ion flux of the end-loss ions. The neutral gas induces radial energy loss due to charge exchange. Also, the radial density profile become flat due to gas injection. Consequently, the ion flux of the end-loss plasmas will decrease with the radial energy loss increase and the radial density profile become flat under the same density.

v) Conclusion of Feature Selection

As was discussed earlier, the line density in the barrier cell and the diamagnetism in the central cell have a linear relationship with the ion flux of the end-loss ions but these two variables are changed as a result of a change in the ion flux. Therefore, we perform a feature selection while excluding these parameters. Figure 4.27 and Fig. 4.28 show the coefficients and RSS as a function of the strength of penalty λ, respectively. Figure 4.28 (b) is an enlarged view of Fig. 4.28 (a) and the *K*-fold cross-validation method with k = 10 is carried out. The RSS slightly increases in comparison with Fig. 4.8. We chose λ of 3×10^{-6} under the one standard error rule. Figure 4.29 and Fig. 4.30 show the coefficients of the parameters with λ of 3×10^{-6} and the response vector **y** (the ion flux after average centering) as a function of the product of design matrix **A** and coefficient vector **x** (**Ax**), respectively.

To enhance the end-loss ion flux, it is necessary to increase the plasma production and decrease the radial energy loss. In GAMMA 10/PDX, we increase of the line densities in the central cell and the anchor cells, and the potential is able to enhance the end-loss ion flux. A linear model for ion flux is obtained by performing feature selection using LASSO.

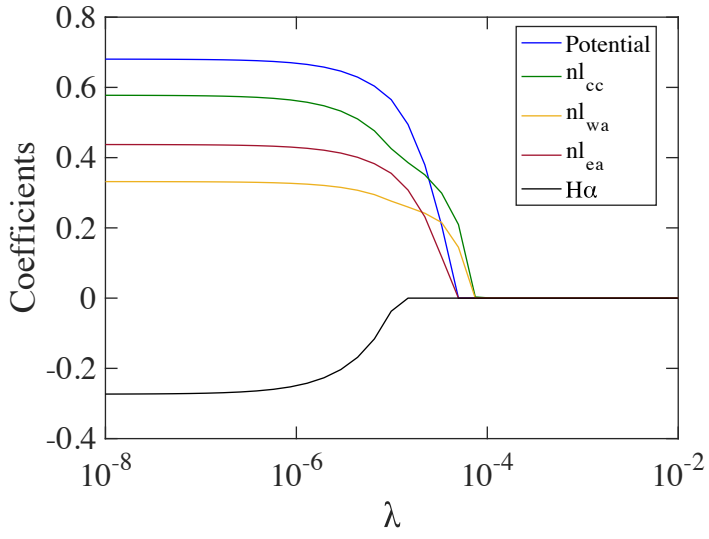

Figure 4.27 The coefficients of each measured value as a function of the strength of penalty λ.

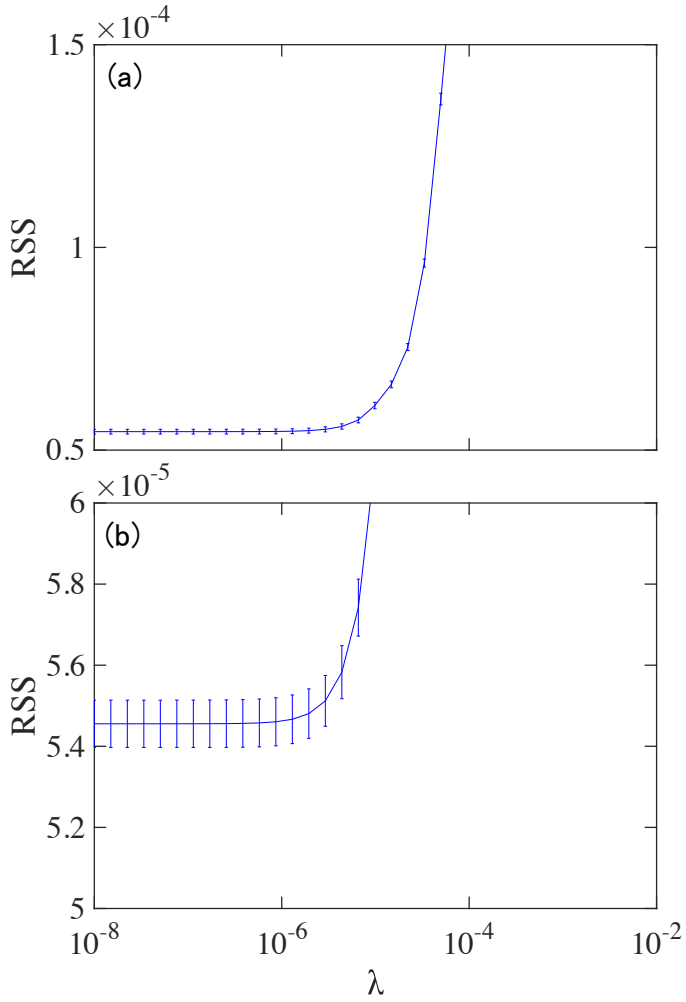

Figure 4.28 (a) The average of the RSS calculated by *K*-fold cross-validation as a function of λ and (b) enlarged view. The error bar shows the standard deviation of RSSs.

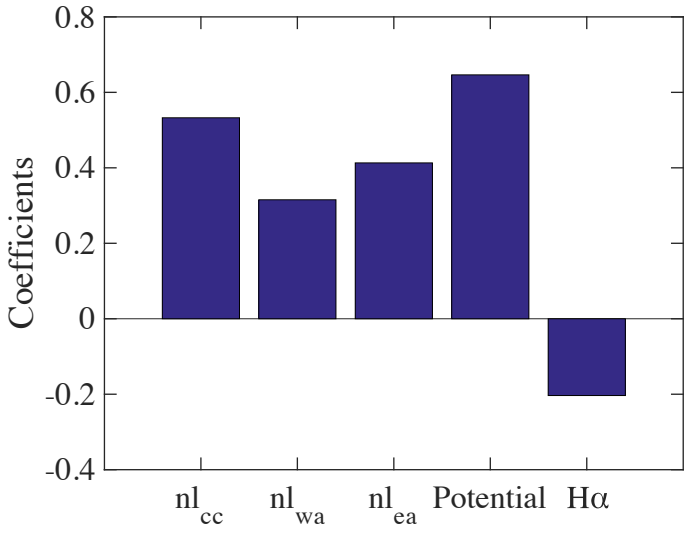

Figure 4.29 The coefficients of the parameters of the measurements; the line densities in the central cell (nl_{cc}), the west anchor cell (nl_{wa}), the east anchor cell (nl_{ea}), the potential observed with west ELIEA and the intensity of Hα in the central cell.

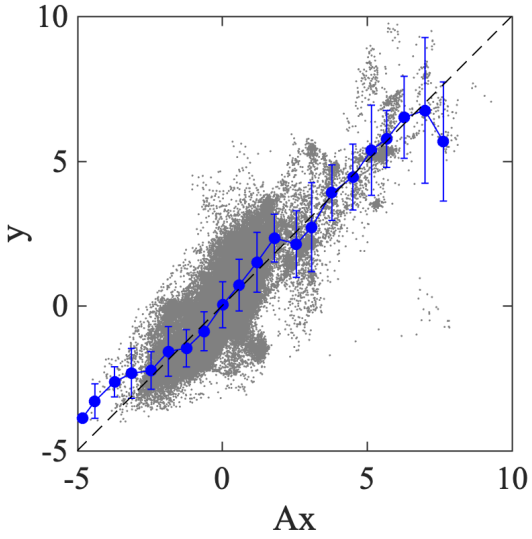

Figure 4.30 The response vector **y** (the ion flux after average centering) as a function of the product of design matrix **A** and coefficient vector **x** (**Ax**).

4.1.2 Enhancement of End-loss Ion Flux by Increasing Density and Potential Using ICRF Waves

As was discussed in Section 4.1.1, to enhance of the end-loss ion flux it is necessary to increase the plasma density and potential, and decrease the intensity of Hα. In this section, we perform additional heating in the anchor cell to enhance the ion flux of the end-loss ions.

The base plasma is produced with ICRF waves excited by RF1 and ion heating in the central cell by RF2 is performed. Additional heating using the ICRF wave with a frequency of the 9.9 MHz is performed with DAT antenna in the east anchor cell from 150 ms to 230 ms. The frequency of 9.9 MHz is same frequency as the ICRF wave excited by east Type-III antenna in the central cell and there is a resonance layer near the midplane of the anchor cell. Control of the phase difference of ICRF waves excited with east Type-III antenna and east DAT antenna is performed [67,68]. Additional gas puffing using GP#1a from 140 ms to 230 ms with a plenum pressure of 400 torr is carried out to increase the density in the central cell and the anchor cells. Figure 4.31 shows the discharge with the increase of the ion flux largely: (a) the line density in the central cell (blue line) and the east (green line) and west (red line) anchor cells, (b) the diamagnetism in the central cell, (c) the ion flux observed at the east (green line) and west (red line) end region, (d) radiated power of the excited ICRF wave for the additional heating, (e) potential observed with ELIEA, and (f) the intensity of Hα in the central cell. The line densities are increased about twice by the additional heating in the anchor cell and additional gas puffing. Meanwhile, diamagnetism is decreased because of the increase of the density and plasma cooling by gas puffing, and the potential is increased from 100 V to 150 V. The ion fluxes increase remarkably from 4.5 $\times 10^{22}$ $m^{-2}s^{-1}$ to 17 $\times 10^{22}$ $m^{-2}s^{-1}$ at east end and 4 $\times 10^{22}$ $m^{-2}s^{-1}$ to 12 $\times 10^{22}$ $m^{-2}s^{-1}$ at the west end. Although the intensity of Hα increases, the ion fluxes are increased by over three times by increasing the line density and the potential. Figure 4.32 shows the energy distribution without (130–150 ms) and with (200–230 ms) additional heating. The additional heating increases the total ion flux but decreases the high-energy end-loss ion flux.

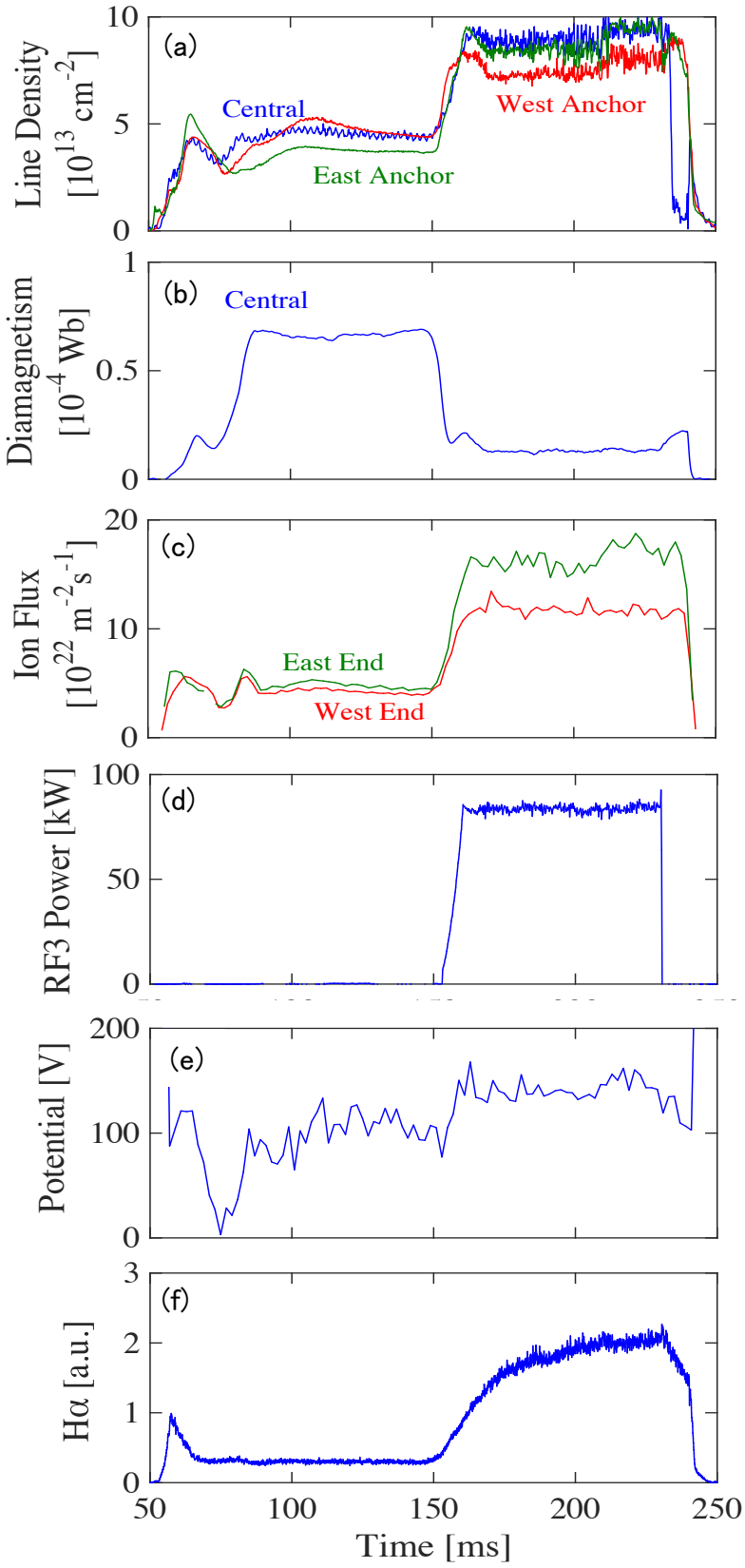

Figure 4.31 Time evolution of (a) line densities in the central cell (blue line), east anchor cell (green line) and west anchor cell (red line), (b) diamagnetism in the central cell and (c) ion currents at the east (green line) and west (red line) end regions, (d) radiated powers of RF3 connected with the east DAT antenna, (e) potential observed with west ELIEA, and (f) the intensity of the Hα in the central cell.

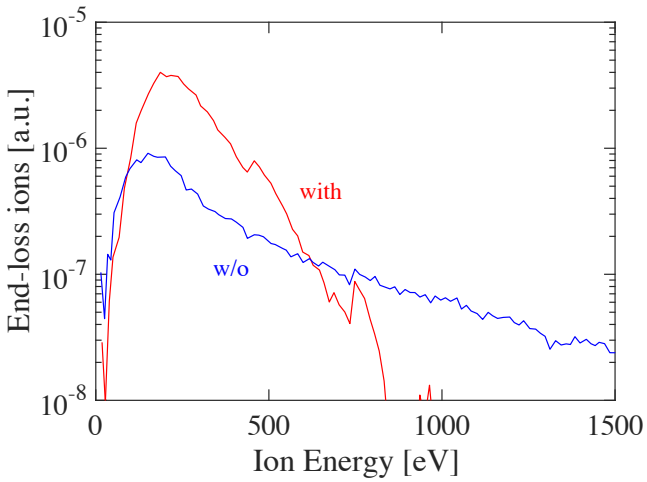

Figure 4.32 The energy distribution without (130–150 ms) and with (200–230 ms) additional heating.

4.2 Enhancement of High-energy End-loss Ions Using ICRF Waves

As shown in Fig. 4.32, the particle flux of the high-energy end-loss ions is decreased with the increase of the density and the diamagnetism in the central cell is decreased. Also, the increase of the potential is not effective on the increase of the ion temperature of the end-loss ions as shown in Fig. 4.21. In order to increase the ion temperature of the end-loss ions, ion cyclotron resonance heating using ICRF waves in the central cell is performed. In previous researches, up to 10 keV of perpendicular ion temperature is achieved by the ion heating in the central cell [49]. Since the ion heating with ICRF waves increase perpendicular ion temperature, high-energy ions are trapped in the mirror configuration and a strong ion anisotropy over 10 is observed. Therefore, the processes of dropping into the loss cone of trapped high-energy ions is necessary to increase the ion temperature of the end-loss ions. In this chapter, the change of energy distribution and pitch angle distribution of the end-loss ions during ion heating is described and the end-loss processes of the high-energy ions are discussed.

4.2.1 Ion Heating in the Central Cell and Enhancement of High-energy End-loss Ions

Ion heating in the central cell is carried out using Alfvén slow waves with a frequency of 6.36 MHz. The ICRF waves are excited with DHT antennas in the central cell driven by RF2 and are absorbed at the resonance layer located near the midplane of the central cell. Figure 4.33 shows the typical temporal evolution of plasma parameters during ion heating in the central cell. Figure 4.33 shows: (a) the line density in the central cell and both anchor cells as blue, red and green lines, (b) the diamagnetism in the central cell, (c) ion flux of the end-loss ions at the west and east end region as red and blue lines, and (d) radiated power from the west and east DHT antennas as red and blue lines, respectively. The line densities are about 5×10^{13} cm^{-2} and the plasma densities are low at 10^{18} m^{-3} in the central and anchor cells. The diamagnetism is increased by up to 0.7×10^{-4} Wb with the increase of the radiated power of RF2. In GAMMA 10/PDX, the diamagnetism increases linearly with the increase of the radiated power of RF2 [49]. Figure 4.34 describes the energy distribution of the end-

loss ions for each diamagnetism at the east end region. The ion flux is fixed 7.65 × 10^{22} $m^{-2}s^{-1}$. The ion temperature is increased from 220 eV to 520 eV.

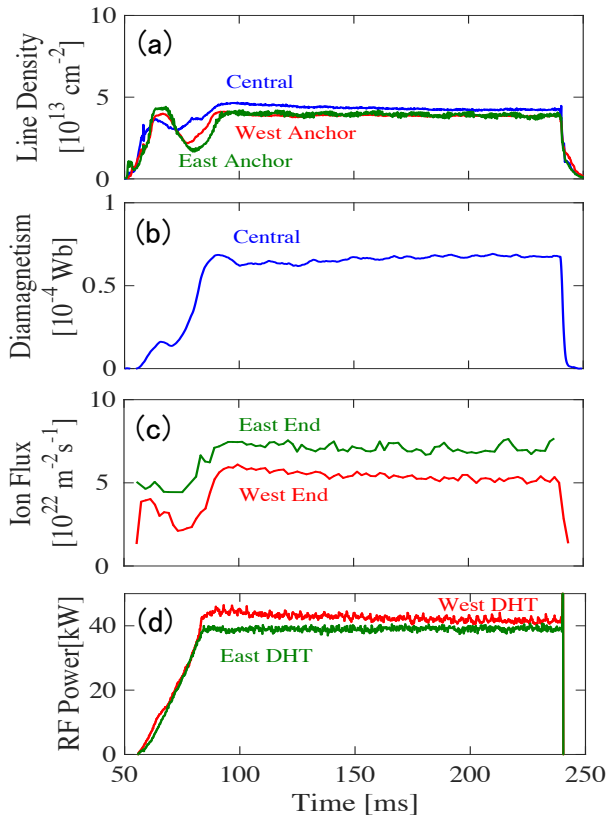

Figure 4.33 Time evolution of: (a) line densities in the central cell (blue line), east anchor cell (green line) and west anchor cell (red line), (b) diamagnetism in the central cell and (c) ion currents at the east (green line) and west (red line) end regions during ion heating with the DHT antennas in the central cell, and (d) radiated powers of RF2 connected with the east (green line) and west DHT (red line) antennas.

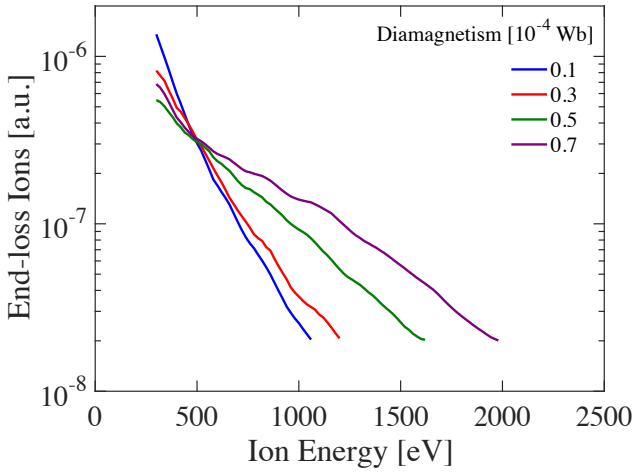

Figure 4.34 Energy distribution of the end-loss ions for each diamagnetism measured at the east end region. The ion flux at the east end region is fixed at 7.65 × 10^{22} $m^{-2}s^{-1}$.

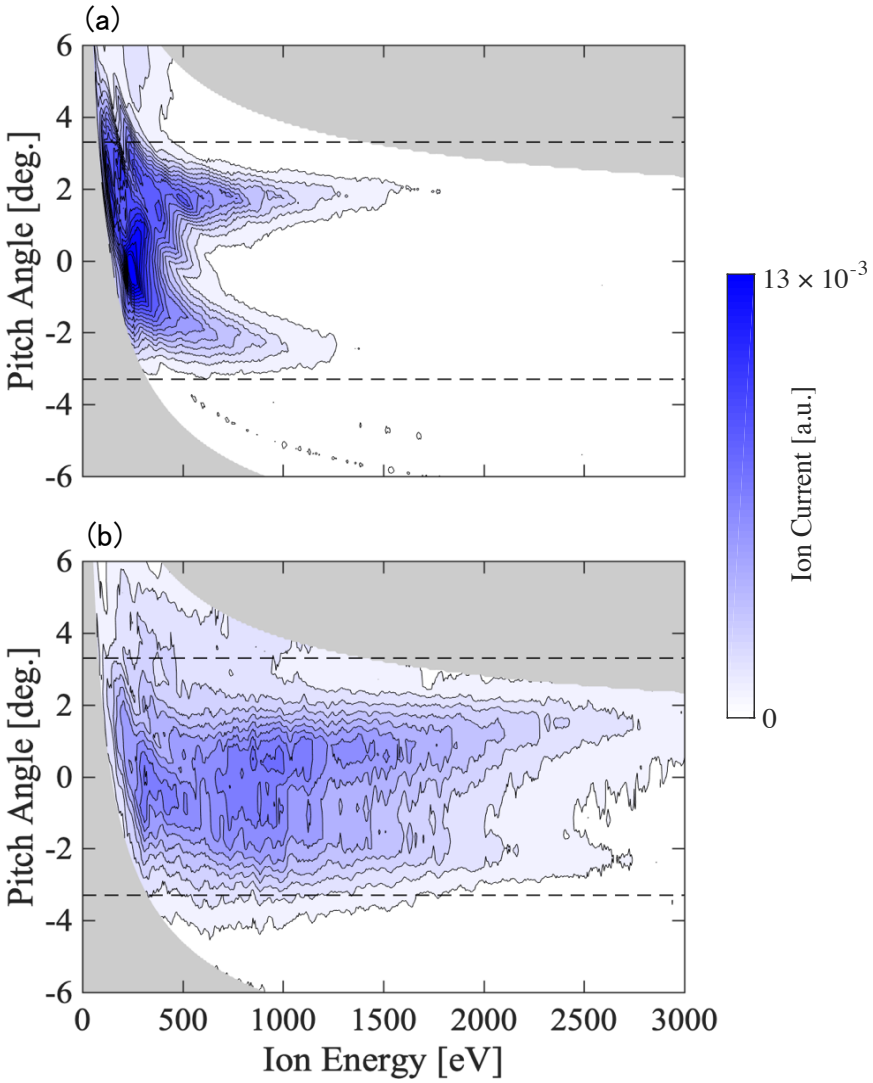

Figure 4.35 Contour maps of the end-loss ions measured at the east end region (a) without ion heating and (b) with ion heating. The dashed lines show the loss-cone boundary of the end-loss ions flowing from the central cell and the anchor cells (3.3 degrees).

To discuss the processes of the end-loss, pitch angle distribution is observed with ELECA. Figure 4.35 shows contour maps of the end-loss ions measured with ELECA at the east end region on: (a) the base plasma without ion heating in the central cell, and (b) the plasma with ion heating. The vertical lines show the pitch angle of the end-loss ions and the horizontal lines show the parallel energy of the end-loss ions. The dashed lines describe the loss-cone boundary (3.3 degree). Areas where the ELECA cannot be observed are masked with gray color. Figure 4.36 shows the pitch angle distribution of the end-loss ions with the energy of (a) 700 eV and (b) 1500 eV. Each colored line describes the pitch angle distribution when the diamagnetism is different. The pitch angle distribution at the same plasma with Fig. 4.35 (a) and (b) are shown as blue lines (diamagnetism is 0.1×10^{-4} Wb) and purple lines (diamagnetism is 0.7×10^{-4} Wb), respectively. The high-energy end-loss ions are increased remarkably by the ion heating. In addition, the pitch angle distribution of the end-loss ions with an energy of over 500 eV change drastically. The ion currents peak near the loss-cone boundary on the base plasma. Meanwhile, the ion currents with a pitch angle of near 0 degree increase with the ion heating and the pitch angle distribution becomes flat. The ion currents are increased overall with the increase of the diamagnetism.

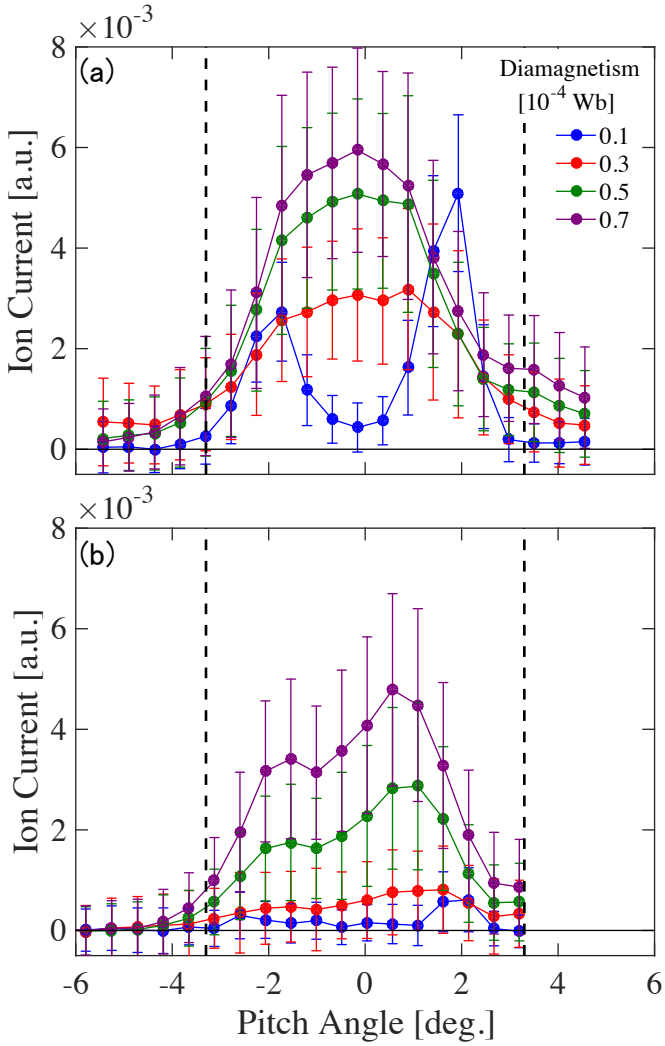

Figure 4.36 Pitch angle distribution of the end-loss ions with the energy of (a) 700 eV and (b) 1500 eV measured at the east end region. The dashed lines show the loss-cone boundary (3.3 degree).

In typical discharges on the GAMMA 10/PDX, ion-ion collision time (a few ten milliseconds) is about 100 times longer than the average transit time (a few hundred microseconds) of the ions from the central cell to the end region. Therefore, the ions drop into the loss region and have almost no change in pitch angle until they reach the end region. This suggests that the high-energy ions that are confined in the central cell drop into the loss region mainly with the pitch angle diffusion due to Coulomb collisions on the base plasma. Meanwhile, the high-energy end-loss ions drop into the loss region mainly with large pitch angle scattering due to wave-particle interaction during ion heating with ICRF waves. Figure 4.37 shows the diamagnetism dependence of the normalized end-loss ion currents within an absolute pitch angle of less than one degree. These end-loss ions are inferred to be dropped into the loss region due to wave-particle interaction. The measured values of the various conditions of the plasmas on about 350 shots are plotted. The influence of the parameters other than the diamagnetism on the high-energy end-loss ions is slight. The end-loss ion currents with energies of 700 eV and 1000 eV increase linearly with the increase of the diamagnetism. The end-loss ion current with the energy of over 1000 eV increases linearly under diamagnetism of about 0.45×10^{-4} Wb and increases drastically over that level. The wave-particle interaction with excited ICRF waves and spontaneously excited waves is discussed in Sections 4.2.2 and 4.2.3, respectively.

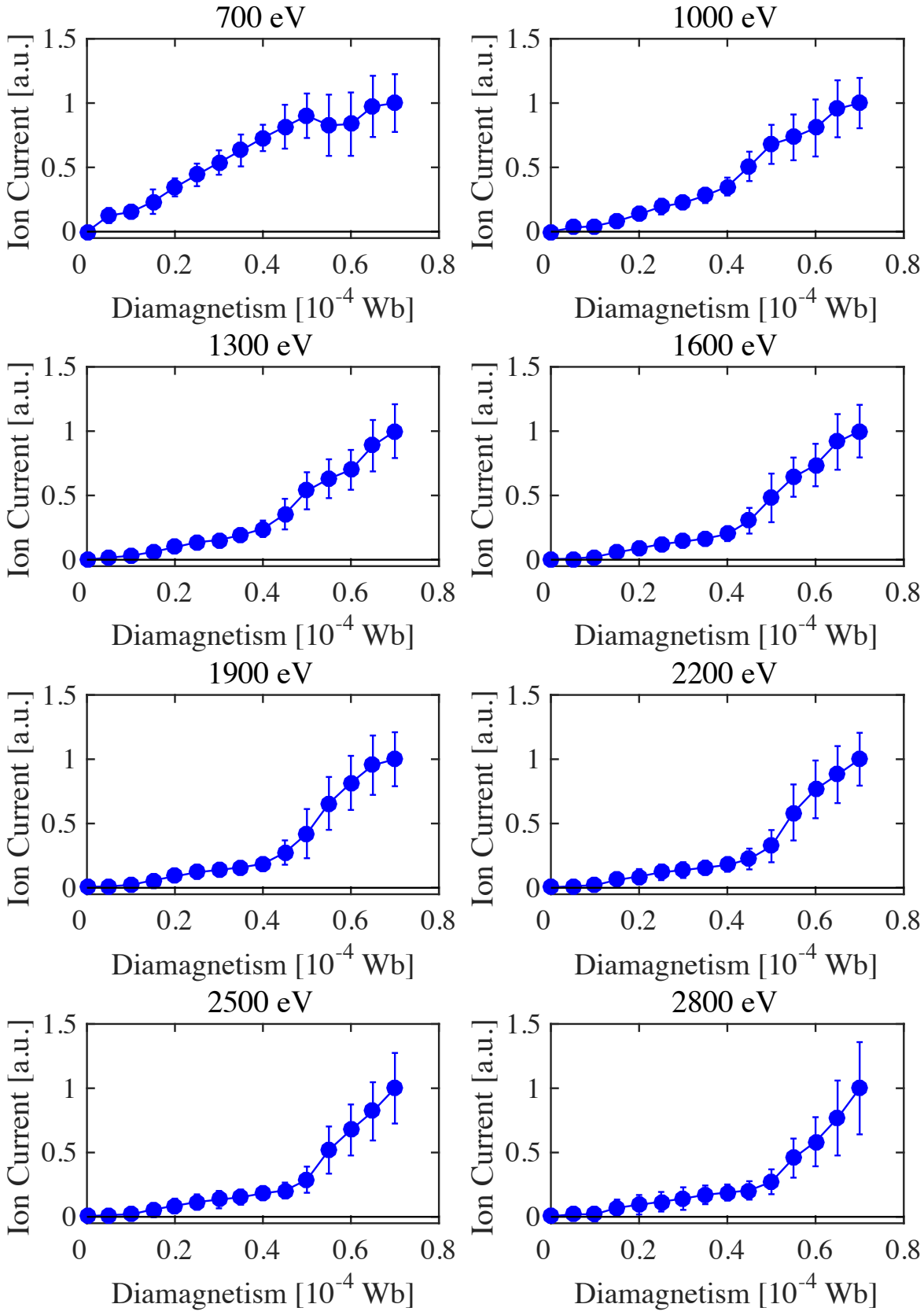

Figure 4.37 Normalized ion currents of the east end-loss ions within an absolute pitch angle of less than one degree as a function of the diamagnetism in the central cell.

4.2.2 Interaction with ICRF Waves Excited by DHT Antennas

To confirm the large pitch angle scattering of the ions due to excited ICRF waves, experiments of ion heating using one side of the DHT antenna in the central cell are performed. In GAMMA 10/PDX, the slow Alfvén waves excited with the DHT antenna propagate from high magnetic field side and are absorbed at the resonance layer that satisfies the ion cyclotron resonance condition of $\omega - k_{//}v_{//} = \omega_{ci}$, where ω is the angular frequency of wave, $k_{//}$ is the parallel wave number, $v_{//}$ is the parallel ion velocity, and ω_{ci} is the ion cyclotron frequency. By selecting the DHT antenna, the direction of $k_{//}$ can be selected and the sign of $k_{//}v_{//}$ of the end-loss ions flowing to the east end region where ELECA is installed can be selected—negative with the east DHT antenna and positive with the west DHT antenna. The position of the resonance layer changes between magnetic fields higher and lower than $\omega = \omega_{ci}$ when the sign of $k_{//}v_{//}$ is negative and positive, respectively. Since there are no wave fields of the slow wave at a magnetic field lower than $\omega = \omega_{ci}$, the end-loss ions flowing to the east end region can only resonate with the slow wave excited by the east DHT antenna.

Figure 4.38 shows (a) the line densities and (b) diamagnetism in the central cell and (c) radiated power of RF2 on the discharges without ion heating as blue lines, with ion heating using the west and east DHT antennas as red and green lines, respectively. The line densities and radiated powers are almost the same for each discharge. The diamagnetism during the ion heating is slightly increased. Figure 4.39 shows the density

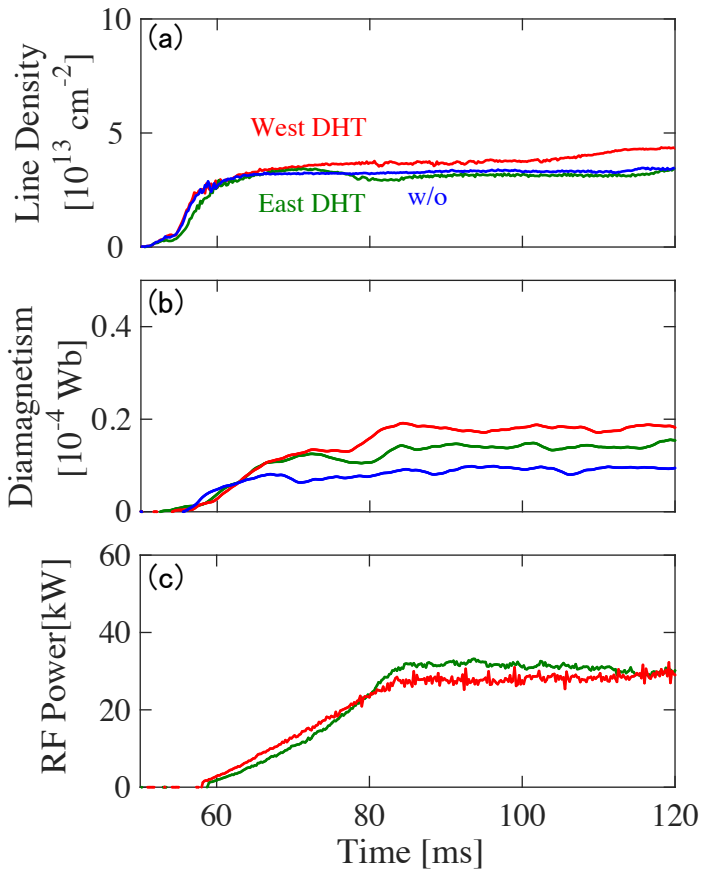

Figure 4.38 Time evolution of (a) the line densities in the central cell, (b) the diamagnetisms in the central cell and (c) the radiated powers of RF2 in the experiments of the ion heating with one side of the DHT antennas.

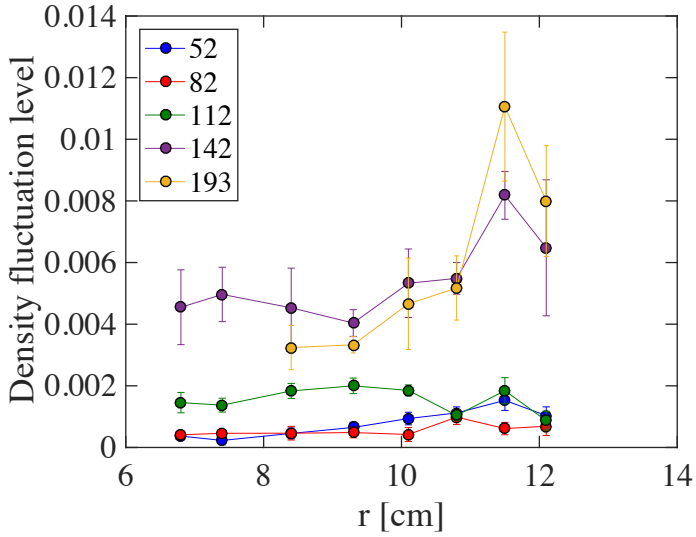

Figure 4.39 Radius profiles of density fluctuation of 6.36 MHz associated with wave field of ICRF wave. The profiles at each z positions are indicated by each color line.

fluctuation of 6.36 MHz associated with wave field of ICRF wave on experiment using the west DHT antenna located at z = 171.5 cm. Each color line describes the density fluctuation observed at each z location and the density profiles at each z position are assumed to be same as the density profile observed with an interferometer located at z = -52 cm. The density fluctuation with a radius less than 8 cm at z = 193 cm and less than 6 cm at other z positions cannot be measured because the phase extraction cannot be performed. The profiles at z = 142 cm and 193 cm are almost the same and become smaller towards the midplane of the central cell. This indicates that the ICRF wave with the frequency of 6.36 MHz is damped at the resonance layer located near z = 100 cm.

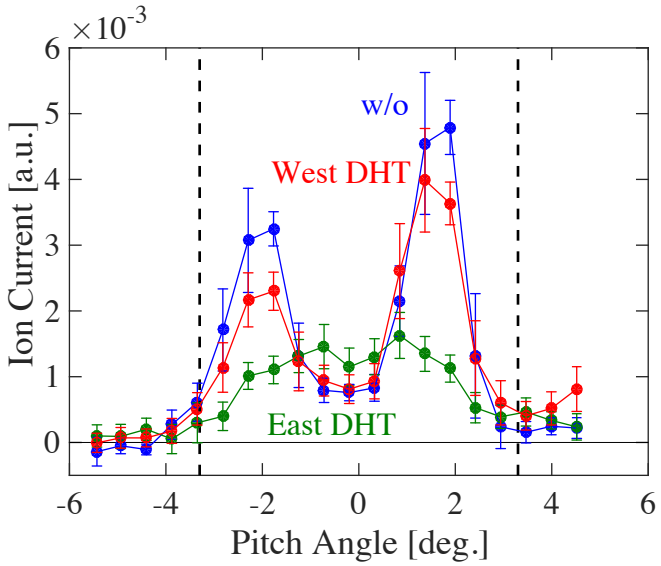

Figure 4.40 Pitch angle distribution of east end-loss ions on same discharges with Fig. 4.38. Signals between 85–105 ms are analyzed.

Figure 4.40 shows the pitch angle distribution of the end-loss ions measured at east end region. The pitch angle distribution with ion heating using the west DHT antenna is almost that same as that without ion heating. Meanwhile, the pitch angle distribution becomes flat and the end-loss ions near 0 degree increase during the ion heating with the east DHT antenna. As was explained previously, only the ICRF wave excited by the east DHT antenna can resonate as the ions move to the east. This suggests that the interaction with ICRF wave enhances the parallel transport of ions with large pitch angle scattering.

The ions in the central cell are scattered from the loss region to the trapped region, and vice versa, because the ICRF wave increases and decreases the perpendicular velocity of resonating ions at the resonance layer. In mirror plasmas, the number of ions in the trapped region is sufficiently larger than that in the loss region [69,70]. Furthermore, the number of ions to the loss region is suggested to be larger than that to the trapped region near the loss boundary. Therefore, the parallel transport of the trapped ions is enhanced due to ICRF waves.

4.2.3 Interaction with Spontaneously Excited Waves

As shown in Fig. 4.37, the end-loss ions with the energy of over 1000 eV is increased drastically over the diamagnetism in the central cell of 0.45×10^{-4} Wb. To confirm the change of the end-loss ions near the diamagnetism of 0.45×10^{-4} Wb, an experiment where the diamagnetism increases slowly is carried out. Figure 4.41 shows (a) the line densities in the central cell (blue line), the west (red line) and east (green line) anchor

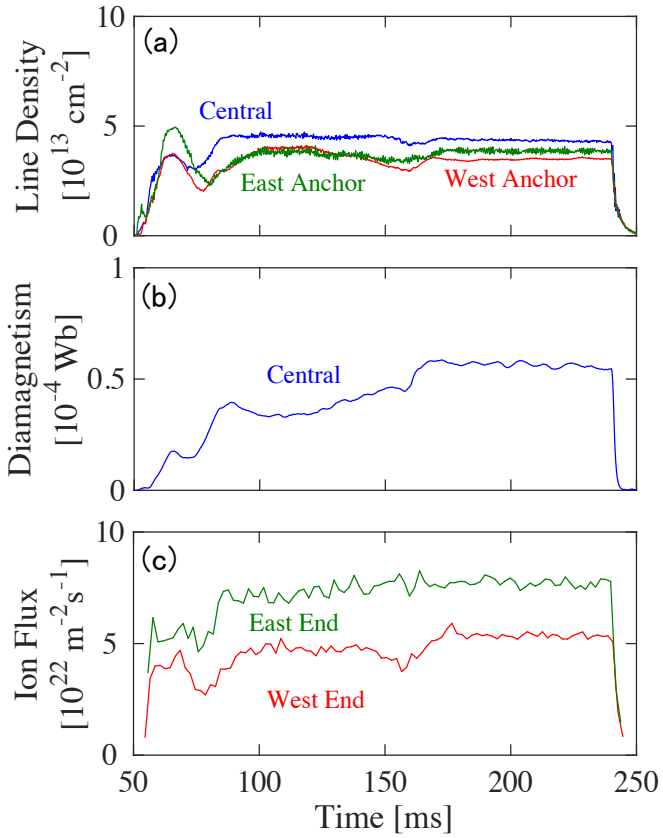

Figure 4.41 Time evolution of (a) line densities in the central cell (blue line), east anchor cell (green line) and west anchor cell (red line), (b) diamagnetism in the central cell, and (c) ion flux at the east (green line) and west (red line) end regions.

cells, (b) the diamagnetism in the central cell and the ion flux observed at the west (red line) and east (green line) end regions. The diamagnetism is increased slowly from 0.33×10^{-4} Wb to 0.58×10^{-4} Wb between 100 ms and 170 ms. Meanwhile, the line densities and the ion flux have no significant change.

Figure 4.42 (a) shows the temporal evolution of intensity plot of the frequency spectrum of the magnetic fluctuation on the same discharge as shown in Fig. 4.41. The frequency between 5.4 MHz to 6.8 MHz is plotted. ICRF wave for ion heating with the frequency of 6.36 MHz is observed. AIC waves with the frequency of about 5.7 MHz are excited spontaneously from 155 ms, where the diamagnetism is about 0.45×10^{-4} Wb, due to strong anisotropy of ion temperature. Figure 4.42 (b) shows the average intensity of 5.6 MHz to 5.8 MHz, which is the intensity of AIC waves. Figure 4.42 (c) shows the ion current of the end-loss ions with specific energy measured by ELECA. The high-energy end-loss ions are increased slowly before 155 ms with the increase of the diamagnetism. In contrast, the high-energy end-loss ions increase drastically due to the excitation of AIC waves. Therefore, it is clarified that the drastic increase from the diamagnetism of 0.45×10^{-4} Wb of the end-loss ions with the energy of over 1000 eV as shown in Fig. 4.37 is caused by the pitch angle scattering due to excitation of AIC waves.

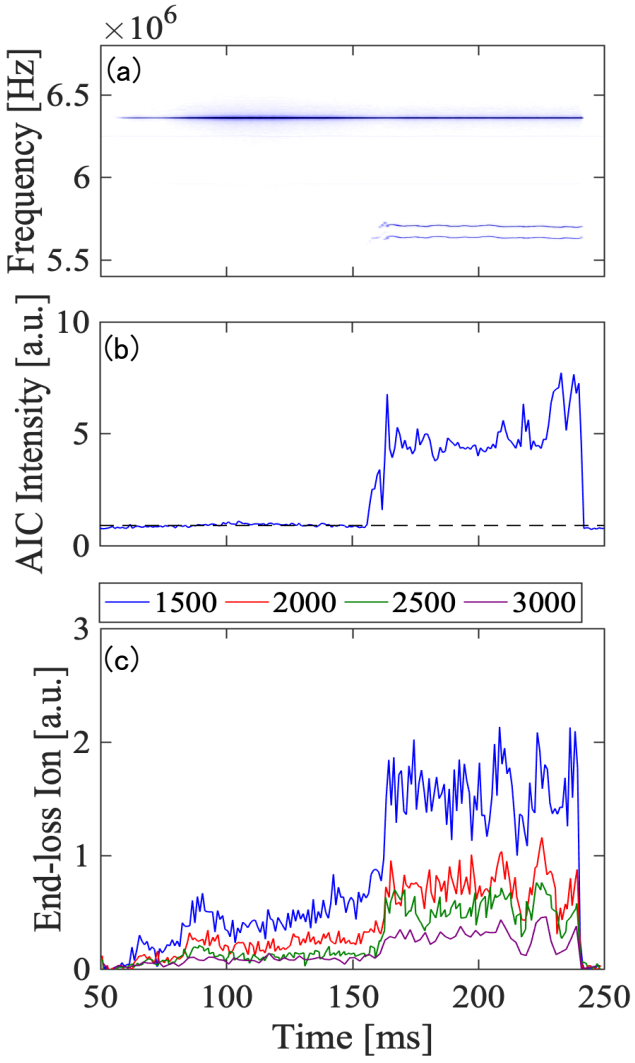

Figure 4.42 Time evolution of (a) the frequency spectrum of magnetic fluctuation in the central cell, (b) the average of intensity of the AIC waves (5.6 - 5.8 MHz) and (c) the end-loss ion currents measured with ELECA in the same discharge with Fig. 4.41

4.3 Using ICRF Waves to Increase Both Ion Flux and Ion Temperature

To further increase both of the ion flux and the ion temperature, the ICRF wave with a frequency of 7.7 MHz is excited with the west DAT antenna driven by RF3. Because the ICRF wave of 7.7 MHz has no resonance layer in the anchor cell, the wave can propagate to the central cell and can be absorbed at the resonance layer located near the west mirror throat in the central cell. Figure 4.43 shows (a) the line densities on the central cell and both anchor cells, (b) the diamagnetism in the central cell, and (c) the ion flux of the

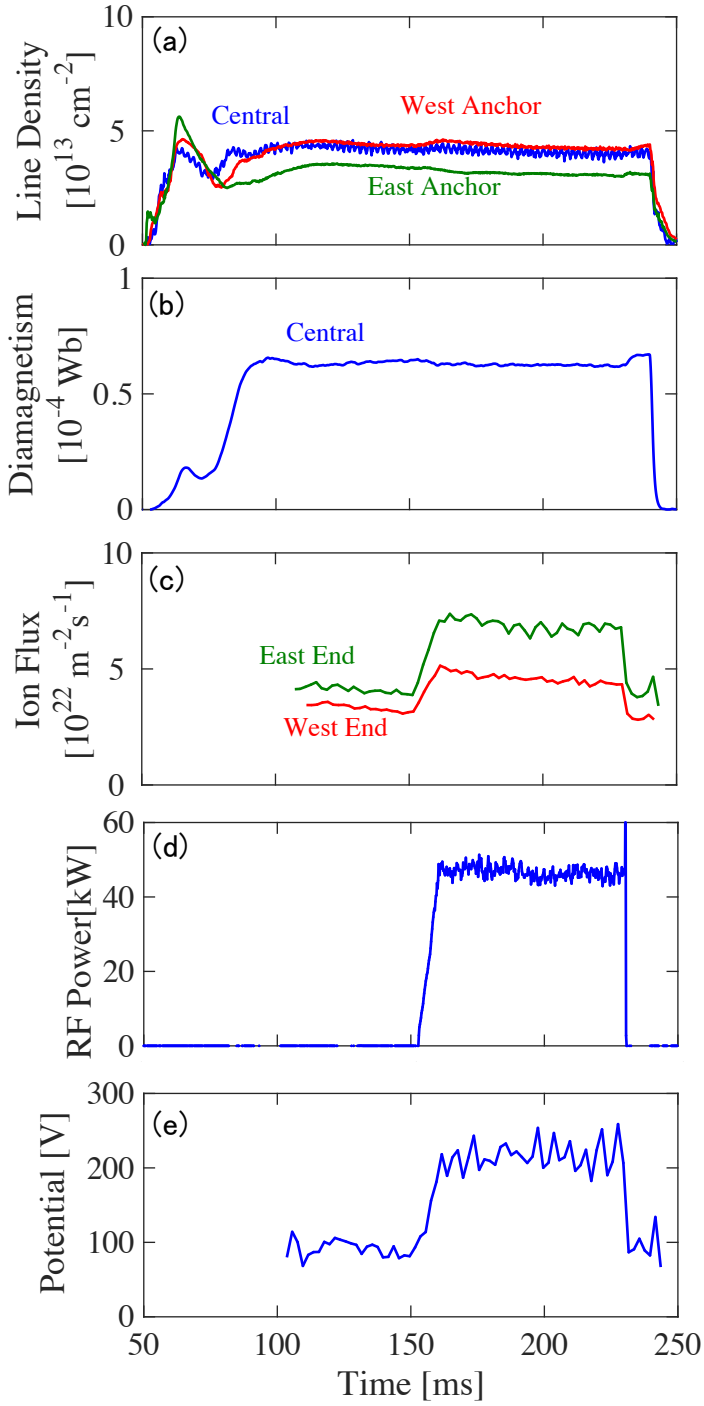

Figure 4.43 Time evolution of (a) the line densities, (b) the diamagnetism, (c) the ion flux, (d) the radiated power of RF3, and (e) the potential on the experiment of additional heating with the west DAT antenna.

end-loss ions observed at the west and east end regions, radiated power of RF3 and plasma potential measured with ELIEA. Ion heating with the DHT antennas in the central cell is carried out with RF2 from 53 ms and the additional heating with RF3 is performed from 150 ms. The line densities and the diamagnetism have little influence with the additional heating. In contrast, the ion fluxes at the both end region increase remarkably with the additional heating, due to the increase of the potential as discussed in Section 4.1. In addition, the increase of the ion temperature at the west end region is observed. Figure 4.44 shows the energy distribution measured with ELIEA at the (a) west and (b) east end region. The blue and red lines show the energy distribution of end-loss ions without (120–150 ms) and with (170–200 ms) the additional heating. The black lines indicate fitting lines assuming two components (low-temperature and high-temperature) of Maxwell distribution. With additional heating, the energy distribution shifts from low energy to high-energy regions and the end-loss ion flux increases in the low-energy region at both ends due to the increase of the potential. The ion temperature of the low-energy component of the end-loss ions has no significant change from 90 eV on both sides. Meanwhile, the temperature of the high-energy component increases from 370 eV to 500 eV on the anchor antenna side and does not increase from 360 eV on the opposite side. An increase of both the ion flux and the ion temperature is observed at the same time on the anchor antenna side, which is consistent with the discussions in Section 4.2.2.

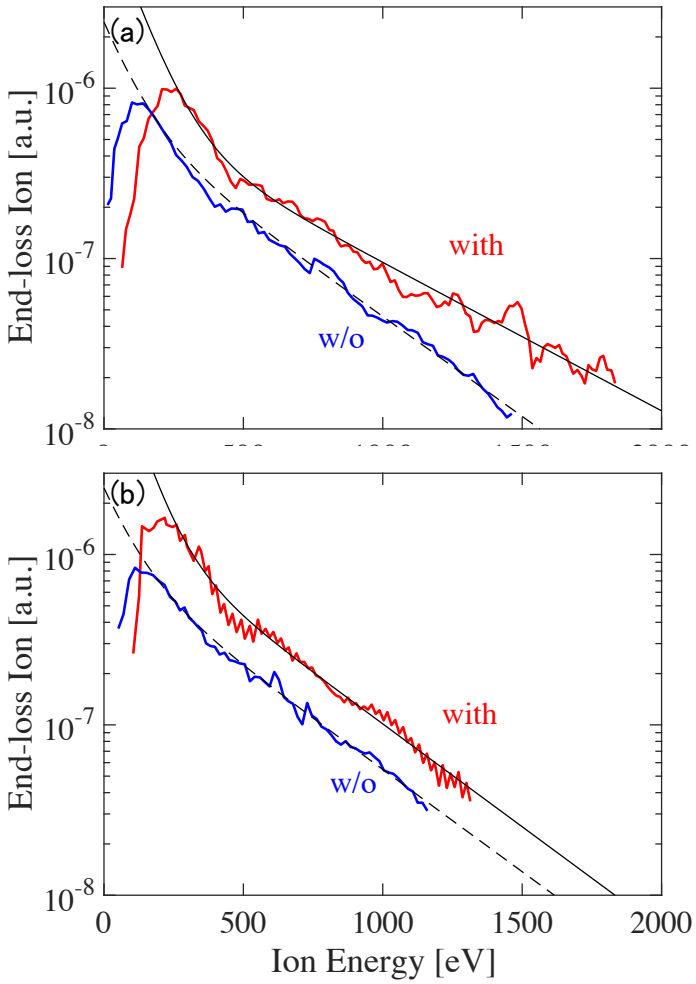

Figure 4.44 Energy distributions of the end-loss ions with and without additional heating observed at (a) the west end region and (b) the east end region.

5. CONCLUSION

The processes of the parallel transport of the ions to the end region in GAMMA 10/PDX are investigated with feature selection and measurements of particle flux, pitch angle distribution and the energy distribution of the end-loss ions. Based on the results, the experiments of the additional heating with ICRF waves have been carried out and the parameter region of the flux and the temperature of the end-loss ions has been expanded. Figure 5.1 shows the parameter region of GAMMA 10/PDX. The black lines show that the heat flux of the end-loss ions. The arrows describe the increase of the flux and/or the temperature of the end-loss ions using ICRF waves.

Using ICRF Waves to Enhance the End-loss Ion Flux

To enhance the end-loss ion flux, the influence of the plasma density, the potential, the diamagnetism and the intensity of Hα on the end-loss ion flux is investigated with feature selection using LASSO. Consequently, we obtain a linear model of the end-loss ion flux. The plasma densities at the central cell and both anchor cells, and the potential positively and the intensity of Hα negatively affect the ion flux.

First, the effect of the plasma density is discussed with measurement of the density profiles in the central cell (z = -52, 52, 82, 112, 142 and 193 cm) and the line density at the mirror throat of the central cell (z = -307 cm) in the both anchor cells (z = ± 520 cm), west plug/barrier cell (z = 866 and 967.5 cm). The influence of the plasma density is explained by the number of the ions in the magnetic tube. Second, the effect of the potential is discussed with orbit calculation of the end-loss ions. The increase of the end-loss ion flux with the increase of the potential is explained by the expansion of the loss region of the ions and the decrease of the transport time of the ions. It is suggested that the increase of the plasma production until the density becomes constant is due to the eigenmodes formation of the ICRF waves.

The end-loss ion flux is increased with additional heating using anchor antenna. The blue dots describe the parameter of the end-loss ions until the additional heating. Additional gas injection is performed to increase the plasma's density. An ICRF wave with a frequency of 9.9 MHz is excited. The plasma density in the central cell and both anchor cells, and the potential have increased remarkably and the end-loss ion flux increases by over three times. In contrast, the ion temperature decreases, due to the increase of the plasma density and plasma cooling with neutral gas.

Using ICRF Waves to Enhance High-energy End-loss Ions

High-energy end-loss ion flux is low and the main source is the pitch angle diffusion by ion-ion collisions without ion heating in the central cell. To enhance high-energy end-loss ions, additional heating using an ICRF antenna installed near the mirror throat of the central cell is performed. ICRF waves with a frequency of 6.36 MHz are excited and absorbed at the resonance layer located near the midplane of the central cell. The ions in the central cell are heated by ICRF waves and the temperature of the end-loss ions is increased as shown in Fig. 5.1 as indicated with yellow dots. It is suggested that the main source of the high-energy end-loss ions is pitch angle scattering due to wave-particle interaction.

The influence of the interaction between ions and excited ICRF waves is discussed with experiments of ion heating using one side of the DHT antenna in the central cell. The experimental results indicate that the high-energy end-loss ion flux increases when the ICRF waves decrease the perpendicular velocity of the ions and the ions dropped into the loss region. In addition, the increase of the high-energy end-loss ion flux is observed with the excitation of the AIC waves. In GAMMA 10/PDX, the main source of the high-energy end-loss ions is interaction with the excited ICRF waves and excitation of the AIC waves.

Ion heating in the central cell and additional heating with anchor antenna is performed to increase the heat flux of the end-loss ions by increasing both the ion flux and the ion temperature. The high-energy ion flux is increased due to the interaction with the excited ICRF waves and the excitation of the AIC waves during the ion heating in the central cell. In addition, an ICRF wave with a frequency of 7.7 MHz that has no resonance layer in the anchor cell is excited by the anchor antenna. The ICRF wave propagates to the central cell and is absorbed at the resonance layer near the mirror throat of the central cell. The potential is increased applying RF field in the anchor cell. The ion flux and the ion temperature increase at the same time due to the increase of the potential and high-energy end-loss ions enhancement by interaction with the additional ICRF wave, respectively, as shown in Fig. 5.1 as red dots. The heat flux of the end-loss ions increases from 0.5 MW/m^2 to 1.5 MW/m^2.

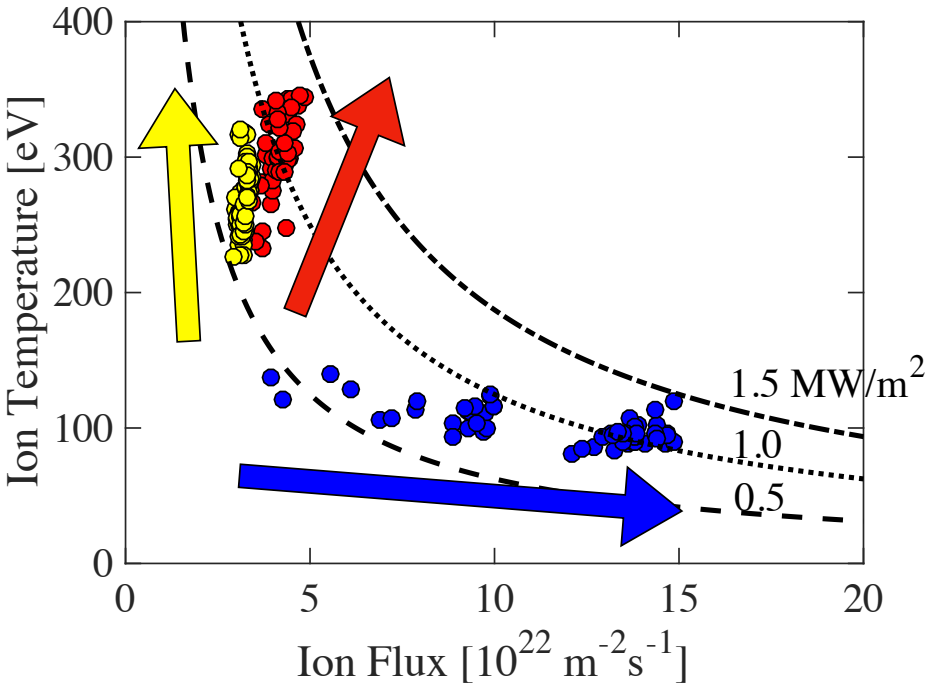

Figure 5.1 Parameter region of GAMMA 10/PDX. The black lines show the heat flux of the end-loss ions.

ACKNOWLEDGMENTS

The author would like to express his deepest appreciation to Dr. M. Ichimura at the Plasma Research Center, University of Tsukuba. Dr. M. Ichimura gives insightful comments and suggestions. Without his support, the present study would not have been possible.

The author would like to express his gratitude to Associate Professor R. Ikezoe at the Research Institute for Applied Mechanics, Kyushu University and Dr. M. Hirata at the Plasma Research Center, University of Tsukuba for their significant discussions and helpful suggestions.

The author would like to appreciate deeply Professor M. Sakamoto at the Plasma Research Center, University of Tsukuba for giving him the opportunity to study.

The author would like to thank Associate Professor M. Yoshikawa, N. Ezumi, R. Minami, Dr. Y. Nakashima and Dr. T. Imai at the Plasma Research Center, University of Tsukuba for their helpful advice.

The author would like to thank especially member of ICRF group for their helpful discussion. The author would like to thank all of the members of the GAMMA 10/PDX group.

This work was partly supported by the bidirectional collaborative research program of the National Institute for Fusion Science, Japan (NIFS19KUGM141, NIFS17KUGM132 and NIFS19KUGM141) and JSPS KAKENHI Grant Number 18K03574.

REFERENCES

1. Y. Koide, H. Adachi, H. Akasaka, K. Akiba, T. Fukuda *et al.*, Phys. Plasmas **4**, 1623 (1997)
2. L. L. Lao *et al.*, Fusion Science and Technology **48**, 968 (2005)
3. Kishimoto, H.; Ishida, S.; Kikuchi, M.; & Ninomiya, H.; Nuclear Fusion **45**, 986 (2005)
4. Y. Kamada *et al.*, Nucl. Fusion **53**, 104010 (2013)
5. T. Sunn Pedersen *et al.*, Nucl. Fusion **55**, 126001 (2015)
6. Komori *et al*., Fusion Science and Technology **58**, 1 (2010)
7. H.A.B. Bodin and A.A. Newton, Nucl. Fusion **20**, 1255 (1980)
8. D. R. Welch, S. A. Cohen, T. C. Genoni, and A. H. Glasser, Phys. Rev. Lett. **105**, 015002 (2010)
9. SA Cohen, AS Landsman, and AH Glasser, Phys. Plasmas **14**, 072508 (2007)
10. McGuire, K.M.; Barnes, C.W.; & Batha, S.H., International Atomic Energy Agency (IAEA) (1997)
11. Watkins, M.L., Nucl. Fusion **39**, 1227 (1999)
12. M. Greenwald *et al.*, PSFC Report, RR-18-2 (2018)
13. M. Gryaznevich, O. Asunta, Fusion Engineering and Design **123**, 177 (2017)
14. Betti, R.; Hurricane, O., Nature Phys **12**, 435 (2016)
15. Loarte A *et al*., Nucl. Fusion **47** S203 (2007)
16. M. Sakamoto *et al.*, Nuclear Materials and Energy **12**, 1004 (2017).
17. N. Ezumi *et al.*, Nucl. Fusion **59**, 066030 (2019)
18. N. Ohno, Plasma Phys. Control. Fusion **59**, 034007 (2017).
19. C. J. Beers *et al.*, Phys. Plasmas **25**, 013526 (2018)
20. R. H. Goulding *et al.*, Fusion Sci. Technol. DOI: 10.1080/15361055.2019.1623569 (2019)
21. Ohno N. *et al.*, Nucl. Fusion **41**, 1055 (2001)
22. Hollmann E, *et al.*, Phys. Plasmas **9,** 1226 (2002)
23. H.J.N. van Eck *et al.*, Fusion Engineering and Design **89**, 2150 (2014)
24. K. Ichimura *et al.*, Plasma Fusion Res. **7**, 2405147 (2012)
25. E.A. Bering III *et al.*, Phys. Plasmas **17**, 043509 (2010)
26. C.S. Olsen *et al.*, IEEE Trans. Plasma Sci. **43**, 252 (2015)
27. Kazunori Takahashi and Akira Ando, Phys. Rev. Lett. **118**, 225002 (2017)
28. Kazunori Takahashi, Aiki Chiba, Atsushi Komuro, and Akira Ando, Phys. Rev. Lett. **114**, 195001 (2015)
29. Kazuki Takase, Kazunori Takahashi, and Yoshinori Takao, Phys. Plasmas **25**, 023507 (2018)
30. Kazunori Takahashi *et al.,* Plasma Sources Sci. Technol. 28, 085014 (2019)
31. K Saito *et al.,* Plasma Phys. Control. Fusion **44**, 103 (2002)
32. J.-M. NOTERDAEME *et al.*, Fusion Science and Technology **53**, 1103 (2008)
33. M. J. Mantsinen *et al.*, AIP Conference Proceedings **1689**, 030005 (2015)
34. Lawrence R. Lyons and Richard Mansergh Thorne, J. Geophys. Res **77,** 5608 (1972)
35. A. Hasegawa, J. Geophys. Res **81,** 5083 (1976)
36. T. Tajima, K. Mima and J.M. Dawson, Phys. Rev. Lett. **39**, 201 (1977).
37. M. Tanaka, J. Geophys. Res. **90**, 6459 (1985).
38. Kitamura *et al.,* Science **361**, 1000 (2018)
39. M. Ichimura *et al.*, Phys. Rev. Lett. **70**, 2734 (1993)
40. K. Ishii *et al.*, Phys. Rev. Lett. **83**, 3438 (1999)
41. T. Saito *et al.*, Phys. Rev. Lett. **82**, 1169 (1999).
42. R. Ikezoe *et al.*, Nucl. Fusion **53**, 073040 (2013)

43. K. Izumi *et al*., Plasma Fusion Res. **14**, 2402033 (2019)
44. M. Inutake *et al.*, Phys. Rev. Lett. **65**, 3397 (1990).
45. M. Ichimura *et al.*, Nucl. Fusion **28**, 799 (1988).
46. M. Inutake *et al.*, Phys. Rev. Lett. **55**, 939 (1985)
47. S. Jang *et al.,* AIP Conf. Proc. **1771**, 030011 (2016)
48. Y. Kubota *et al*., Plasma Fusion Res. **14**, 2401012 (2019)
49. M. Ichimura *et al.*, Plasma Phys. Rep. **28**, 727 (2002)
50. M. Inutake *et al.*, Proc. 17th International Electric Pro- pulsion Conference, 213-221 (1984).
51. T. Goto：Ph. D, Univ. of Tsukuba (2000)
52. P. Varela *et al.*, Review of Scientific Instruments **66**, 4937 (1995)
53. K. W. Kim *et al.*, Review of Scientific Instruments **66**, 1229 (1995)
54. Akira EJIRI *et al.,* Plasma Fusion Res. **2**, 040 (2007)
55. Saeideh Koohestani *et al.*, Fusion Engineering and Design **113**, 139 (2016)
56. Hitoshi Hojo *et al.*, Jpn. J. Appl. Phys. **32**, 3287 (1993)
57. A. Mase *et al.*, Review of Scientific Instruments **66**, 821 (1995)
58. R. Ikezoe *et al.,* Rev. Sci. Instrum. **88**, 033504 (2017)
59. R. Ikezoe *et al.*, Fusion Sci. Technol. **68**, 63 (2015)
60. S. Sumida *et al.*, Fusion Sci. Technol. **68**, 136 (2015)
61. S. Jang *et al.*, Plasma Fusion Res. **14**, 2402032 (2019)
62. Tibshirani R. Journal of the Royal Statistical Society. Series B (Methodological) **58**, 267 (1996)
63. Jerome Friedman *et al.*, J Stat Softw. **33**, 1 (2010)
64. Makoto Uemura *et al.*, Publications of the Astronomical Society of Japan **67**, 55 (2015)
65. A. Tanaka *et al.*, Plasma Fusion Res. **14**, 2401028 (2019)
66. Y. Yamaguchi *et al*., Fusion Sci. Technol. **55**, 106 (2009)
67. T. Yokoyama *et al.*, Fusion Sci. Technol. **68**, 185 (2015)
68. T. Okada *et al.*, Fusion Sci. Technol. **68**, 161 (2015)
69. R. H. Cohen *et al.*, Nucl. Fusion **18**, 1229 (1978)
70. R. H. Cohen *et al.*, Nucl. Fusion **20**, 1421 (1980)